Fall 2010

Chemical bath deposition and electrodeposition of epitaxial semiconductor materials for application in photovoltaic devices

Guojun Mu

Department: Chemistry

CHEMICAL BATH DEPOSITION AND ELECTRODEPOSITION OF EPITAXIAL SEMICONDUCTOR MATERIALS FOR APPLICATION IN PHOTOVOLTAIC DEVICES

by

GUOJUN MU

A DISSERTATION

Presented to the Faculty of the Graduate School of the

MISSOURI UNIVERSITY OF SCIENCE AND TECHNOLOGY

In Partial Fulfillment of the Requirements for the Degree

DOCTOR OF PHILOSOPHY

in

CHEMISTRY

2010

Approved by

Jay A. Switzer, Advisor
Frank Blum
Nicholas Leventis
Jeffrey G. Winiarz
F. Scott Miller

PUBLICATION DISSERTATION OPTION

This dissertation has been prepared in the format used by *Chemistry of Materials*. This dissertation consists of one article that has been published and two articles intended for submission. Paper I (pages 41-61) is published in *Chemistry of Materials* 2009, vol 21(17), pp 3960-3964. Papers II (pages 61-90) and III (pages 91-112) are written for submission to *Chemistry of Materials.*

ABSTRACT

This dissertation investigates the chemical bath deposition of zinc oxide and electrodeposition of cuprous iodide on polycrystalline and single crystal substrates. Paper I describes the chemical bath deposition and characterization of titled epitaxial zinc oxide nanospears on Si(001) single crystal substrate. In Paper II, the chemical bath deposition of zinc oxide nanospears from highly alkaline solutions is discussed in detail, including a thermodynamic calculation of saturation and speciation of Zn(II) in aqueous solution, and a kinetic study of the deposition process. In this paper the epitaxial zinc oxide is reported grown on Au(100), (110), and (111) single crystals. Paper III involves the electrodeposition of epitaxial cuprous iodide thin films on single crystalline Au(100) substrate from a slightly acidic Cu(II)-EDTA-KI solution. The electronic property of the so deposited CuI film is estimated by photoluminescence spectroscopy.

This dissertation also includes three appendices. The first two appendices cover the supplementary materials for Papers I and II. The third appendix has unpublished results on thermal transformation of electrodeposited magnetite and ferrihydrite into hematite.

ACKNOWLEDGMENTS

I would like to thank my advisor, Dr. Jay A. Switzer for his knowledge, encouragement, guidance, and patience throughout my graduate studies. His time and effort will always be appreciated. Likewise, I would like to thank Professors Frank Blum, Nicholas Leventis, Jeffrey G. Winiarz, and F. Scott Miller for agreeing to be part of my committee and educating me in the fundamentals of science throughout my years at Missouri University of Science and Technology. Similarly, I would like to thank all my professors and teachers for their words of wisdom and their time spent educating me.

Along with this gratitude is the appreciation of the scientific discussions, basic knowledge, and many friendships gained from being part of the Switzer group, the Chemistry Department, and the Materials Research Center. Special thanks go to Dr. Eric W. Bohannan, Dr. Steven J. Limmer, Dr. Vishnu V. Rajashekaran, Dr. Shaibal K. Sarkar, Dr. Elizabeth A. Kulp, Dr. Sansanee Boonsalee, Rakesh V. Gudavarthy, Niharika Burla, Zhen He, and Samantha Mathews. I would especially thank my parents, without whose love and encouragement, I would not have fulfilled my dream of being a PhD. I would also like to thank all my friends for their constant supports during the course of my study.

Last but not least, I would like to acknowledge the financial support of the National Science Foundation (DMR-0504715) and Department of Energy Grant (DE-FG02-08ER46518).

TABLE OF CONTENTS

PAPER

LIST OF ILLUSTRATIONS

Page

LIST OF TABLES

Page

PAPER II

1. INTRODUCTION

This dissertation presents the studies on the electrodeposition and chemical bath deposition of epitaxial semiconductor materials of zinc oxide and cuprous iodide onto single crystalline substrates of silicon and gold. It also includes studies on the thermal transformation of hematite from electrodeposited magnetite thin films and ferrihydrite nanoribbons.

Paper I reports the chemical bath deposition of epitaxial ZnO nanospears on degenerate p-type Si(001) substrate from an alkaline supersaturated solution of Zn(II) at 70 ^{o}C. The lattice mismatch between the hexagonal ZnO and diamond cubic Si is reduced dramatically from -40.16% for an un-tilted structure to -0.25% in the ZnO $[1\bar{2}10]$ direction and -0.99% in ZnO $[25\overline{\overline{76}}]$ direction by tilting the nanospears 51^{o} relative to the surface normal. The tilted nanostructure brings the $(20\bar{2}3)$ planes of ZnO into coincidence with the (001) planes of Si. The photoluminescence (PL) spectrum of ZnO on Si shows a UV emission at 364 nm (3.41 eV) which is assigned to be ZnO exciton emission, and a stronger visible emission at 500-700 nm attributed to multiple sources, mainly the singly ionized O vacancies, or the Zn interstitials in the ZnO crystal, or both.

Paper II describes in detail the chemical bath deposition of ZnO from highly alkaline solutions. According to thermodynamic calculation, the driving force for deposition is the slight excess of saturation state of Zn(II) ions in the solution. XRD patterns and SEM micrographs show that below 60 ^{o}C the deposits are ε-$Zn(OH)_2$, whereas temperatures of 60 ^{o}C and above yield pure ZnO. The activation energy (E_a) is 70 kJ/mol for depositing $Zn(OH)_2$ and 32 kJ/mol for depositing ZnO. The green emission (500-700 nm) of ZnO in the PL spectrum is dramatically reduced by a post-deposition

calcination. The remaining green emission at 333 nm is due to Na impurity in the ZnO. Epitaxial ZnO nanocolumns were deposited onto Au(100), (110) and (111) single crystal substrates at 70 ^{o}C using this method. The epitaxial relationships between ZnO and Au determined by X-ray θ-2θ scan and X-ray pole figures. They are ZnO $(0001)[10\bar{1}1]$ //Au $(100)[011]$ and ZnO $(0001)[10\bar{1}1]$ //Au $(100)[0\bar{1}1]$ for ZnO on Au(100). Those on Au(110) and Au(111) are ZnO $(0001)[10\bar{1}1]$ // Au $(110)[001]$ and ZnO $(0001)[10\bar{1}1]$ //Au $(111)[\bar{1}10]$, respectively.

Paper III addresses the electrodeposition of epitaxial γ-CuI thin films on Au(100) single crystals from a slightly acidic Cu(II)-EDTA-KI solution (pH=3) at 50 ^{o}C. CuI could be generated at more negative potentials than predicted by the linear sweep voltammogram, a phenomenon believed to be due to a chemical oxidation of electrochemically deposited Cu metal by I_2 in the solution. XRD shows that the films deposited at potentials of -0.1, -0.2, -0.3, and -0.4 V versus Ag/AgCl are all pure CuI, whereas that deposited at -0.4 V is a mixture of Cu and CuI. The PL spectra of these films show that the deposited CuI exhibit a sharp free-exciton emission peak at 409 nm, and a weak bound-exciton emission peak at 413 nm and broad red emission at 680 nm due to crystal defects. The epitaxial CuI film was deposited on Au(100). The epitaxial relationships for the four CuI domains on Au(100) are CuI $(111)[2\bar{1}\bar{1}]$ //Au(100)[001], Cu $(111)[2\bar{1}\bar{1}]$ //Au(100)[010], Cu $(111)[2\bar{1}\bar{1}]$ //Au $(100)[00\bar{1}]$, and Cu $(111)[2\bar{1}\bar{1}]$ //Au $(100)[0\bar{1}0]$. That is, the CuI(111) planes and Au(100) planes are parallel, and the CuI $[2\bar{1}\bar{1}]$ and Au<010> in-plane directions are coincident.

Additionally, Appendix A provides supplementary information on the work described in Papers I and II, specifically calculations of solubility and species distribution of Zn(II) in aqueous solutions. Appendix B reports the morphology and X-ray diffraction analysis of the ZnO samples. In particular, it addresses those deposited on gold-sputtered microscope slides from alkaline solutions by electrochemical oxidation of various amino acids and chemically deposited on Si(100) using various bases (LiOH, NaOH, KOH, and CsOH). It also presents the result for those deposited on epitaxial Cu_2O thin films on Au(100), Au(110), and Au(111) substrates. Finally, Appendix C reports the thermal transformation of electrodeposited epitaxial thin films of magnetite into epitaxial thin films containing maghemite and hematite on Au single crystals, as well as the thermal transformation of ferrihydrite nanoribbons into hematite nanoribbons on gold substrates.

1.1. SEMICONDUCTOR MATERIALS

The research reported in this dissertation involves the synthesis and characterization of various semiconductor materials that are promising candidates for applications in photovoltaic devices. This section briefly discusses the crystal structures as well as the electrical and physical properties of these materials.

1.1.1. Zinc Oxide. ZnO is an n-type semiconductor material with a direct and wide band gap of 3.37 eV,[1] which makes it transparent to the visible light and functional in the UV and blue ranges.

The exciton binding energy of this material is about 60 meV at room temperature, 2.4 times of the room temperature thermal energy (25 meV), which gives rise to an intense near-band-edge excitonic emission in ZnO at room temperature and beyond.[2-3]

Over the last several decades, significant efforts have focused on both syntheses and applications of this material due to its outstanding performance in the functional devices such as light emitting diodes,[4-5] laser diodes,[6] UV detectors,[7-8] piezoelectric diodes,[9-11] field effect transistors,[12] gas sensors,[13-15] and solar cells.[16-19]

1.1.1.1 ZnO crystal structures. ZnO is a group II–VI binary oxide, the ionicity of which is between that of covalent and ionic compounds. ZnO has three crystal structures: primitive hexagonal wurtzite, face-centered cubic zinc blende, and face-centered cubic rocksalt structures. In the first two cases, each cation is coordinated with four anions at the corners of a tetrahedron, whereas in the rocksalt structure each cation is surrounded by six anions. Under ambient conditions, ZnO is thermodynamically stable only in the wurtzite structure, therefore it has an tendency to be formed in this phase. The zinc blende structure has been observed on the ZnS substrate with the same structure.[20-21] Further, it has been observed surprisingly to exist in the arms of ZnO wurtzite tetrapods.[22-23] The rocksalt structure has been observed only under higher pressures.[24-26] The present work only addresses the wurtzite structure.

The polarity in wurtzite ZnO is responsible for piezoelectricity spontaneous polarization and affect the crystal growth habits as well as defect generation. The space group of wurtzite ZnO is $P6_3mc$, with lattice parameters of a = b = 3.25 Å, c = 5.21 Å, α = β = 120°, and γ = 90°. As shown in Figure 1.1, the Zn^{2+} cations (ionic radii = 0.6 Å) in a unit cell are presented as smaller white balls, occupying the (0, 0, 0,) and (2/3, 1/3, 1/2) positions; whereas O^{2-} anions (ionic radii = 1.38 Å), represented as larger grey balls, take the positions of (0, 0, 3/8) and (2/3, 1/3, 7/8). The polarity is due to the lack of inversion center in the crystal. The basal plane $(000\bar{1})$ is different from the top plane (0001), one

having oxygen and the other having zinc. Thus, the polarity forms along the *c*-axis, pointing positively to the (0001) plane. The side planes $\{10\bar{1}0\}$ that have equal numbers of Zn and O, on the other hand, are nonpolar.[27]

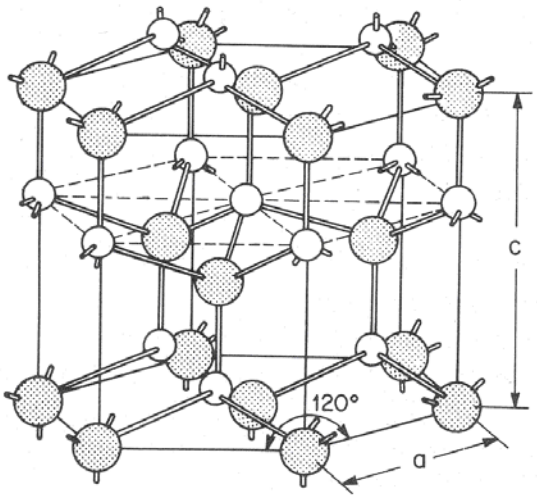

Figure 1.1. ZnO hexagonal wurtzite structure. The larger gray balls represent O atom, and the smaller white balls represent Zn atom.

1.1.1.2 ZnO electronic structures. Many groups have calculated the electronic band structure of ZnO.[28-31] Among them, the local density approximation (LDA) with dominant atomic self-interaction-corrected pseudopotentials (SIC-PP) accurately accounts for the contributions of Zn 3*d* electrons.31 Figure 1.2 shows the resulting band structure along the hexagonal Brillouin zone. The conduction band minima and valence band maxima occur at the point Γ, indicating that ZnO is a direct bandgap semiconductor material. From bottom to top, the groups of bands are Zn 3*d* levels (10 bands, -9 eV), O 2*p* levels (6 bands, -5 to 0 eV), and Zn 3*s* levels (2 bands, top). According to this

calculation, the band gap is 3.77 eV, which agrees closely with the experimental value of 3.4 eV. In addition, the results of the electronic structure calculation of ZnO crystal surfaces shows that the Zn face has more covalent character, whereas the O face is more ionic. Two more useful properties are the effective mass of ZnO, $m_e^* = 0.28m_o$ and hole effective mass $m_{hh}^* = 0.78m_o$ These properties are calculated using the first-principles orthogonalized linear combination of atomic orbital method in the local density approximation.[32] The carrier concentration in ZnO varies a lot according to the quality of crystallization, but it is usually in the range of 10^{16}~10^{17} cm^{-3}, which can be significantly improved by doping.[33-39]

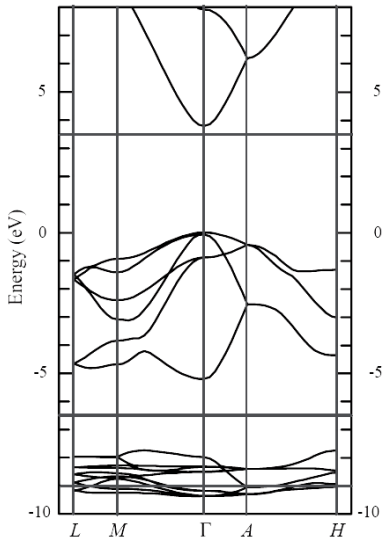

Figure 1.2. Local density approximation (LDA) band structure of bulk wurtzite ZnO in the hexagonal Brillouin zone calculated with dominant atomic self-interaction-corrected pseudopotentials (SIC-PP). [31]

The possibility for band gap engineering is important for industrial applications of ZnO. By doping or alloying with another material of a different band gap, the band gap of ZnO can be finely tuned For example, $Zn_xMg_{1-x}O$ may have a band gap range of 3.37 to 4.0 eV,[40-44] and for $Zn_xCd_{1-x}O$ the range is from 2.9 to 3.37 eV.[40, 45-47]

1.1.1.3 ZnO photoluminescence spectra. The PL emissions can be classified by their origins, that is, either intrinsic or extrinsic transitions. Intrinsic transitions depend on the essential nature of the semiconductor materials, whereas the extrinsic properties are related to dopants, native defects, impurities, or complexes, which usually create additional electronic states in the band gap and therefore affect both absorption and emission processes.

An exciton in semiconductor materials is a bound state of a conduction band (CB) electron and a free valence band (VB) which are attracted to each other by Columbic force. Excitons are classified as free or bound. Those bond ones can be bound to neutral or charged donors and acceptors. For a shallow neutral donor-bound exciton, for example, two electrons in the bound exciton state are assumed to pair off into a two-electron state with zero spin. The additional hole is then weakly bound in the net hole-attractive Coulomb potential set up by this bound two-electron aggregate. Similarly, shallow neutral acceptor bound excitons have a two-hole state derived from the topmost valence band and one electron interaction.

Other extrinsic transitions can be seen in optical spectra. These include free-to-bound (electron-acceptor), bound-to-bound (donor-acceptor), and the so-called yellow/green luminescence. The well known green band in ZnO luminescence spectra (a

broad peak around 500–700 nm) is observed in nearly all samples regardless of growth conditions. A requisite consensus on this issue is still lacking.

Figure 1.3 shows a PL spectrum obtained by Meyer et al. on undoped n-type bulk ZnO produced by Eagle-Picher.[48] The spectrum was excited by the 325-nm line of an He-Cd laser (30 mW) at liquid helium temperature of 4.2 K. Emissions are visible from the band edge to the green/orange spectral range. The free exciton emission with a valence band of 3.375 eV is visible. The prominent lines positioned at 3.3628, 3.3608, 3.3598, and 3.3570 eV are observed due to bound exciton recombinations (excitons bound to neutral donors (D^0X) or acceptors (A^0X)). At lower energies from 3.34 to 3.31 eV further recombination lines appear. Their longitudinal optical (LO) phonon replicas are found at energies of 72 meV (E_{LO}) lower than each BE lines. Also found is a donor-acceptor pair transition (DA_xP, with an unknown chemical identity of acceptor A_x) with energy of 3.22 eV, again with its phonon replicas (DA_xP-E_{LO} and DA_xP-$2E_{LO}$). The green-band emission between 1.9 to 2.8 eV, defect related, still possesses unclear origins.

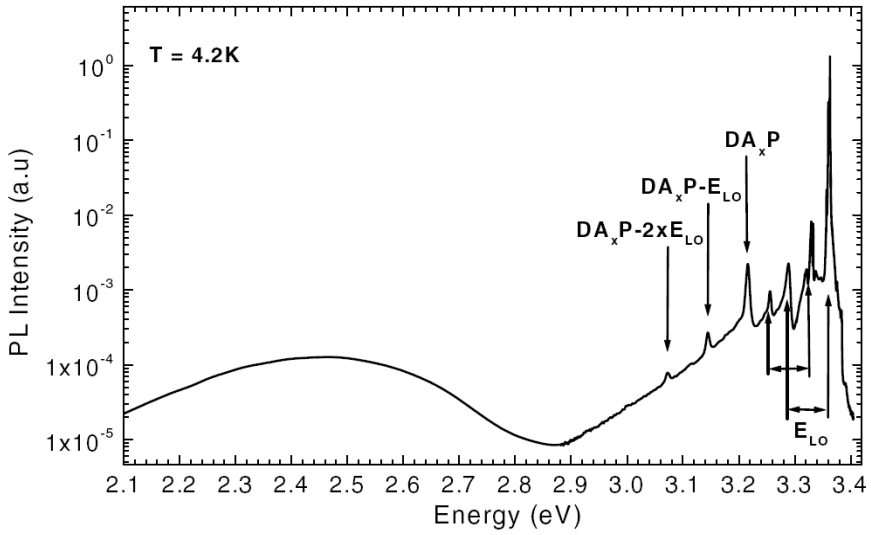

Figure 1.3. Photoluminescence spectrum of n-type bulk ZnO with He-Cd excitation of 325 nm at 4.2 K, showing bound exciton recombination, donor-acceptor pair transition, and green-band emission.

1.1.2. Cuprous Iodide. Below the melting temperature of 873 K, CuI crystal has three phases. The high-temperature α phase (stable at above 680 K) is distorted face-centered cubic. The β phase that only exists in a narrow temperature range of 642-680 K is hexagonal wurtzite.[49] Both α and β phase CuI are superionic conductors with Cu^+ ions being the mobile species.[50-52] Their conductivity level is comparable to those of liquid electrolytes.[53] The low temperature γ phase has an ordered face-centered cubic zinc blende structure, as illustrated in Figure 1.4.

The γ-CuI has drawn much attention in recent years because of its unique properties. It is one of the few *p*-type semiconductor materials with wide band gap (such as CuSCN,[54] and $CuAlO_2$[55]). It has a wide band gap of 3.053 eV and large exciton binding energy of 62 meV.[53] The conductivity in CuI is believed to arise from the

stoichiometric excess of iodide.[56-58] Therefore, CuI has been reported to be used as the electrolyte layer in solid-state dye-sensitized solar cells and provides much higher hole mobility than molecular solids or polymers.[54,58] It is also one of the inorganic scintillation crystal materials with ultrafast scintillation property at a decay time of about 90 ps at room temperature.[59]

Kim et al. have reported energy splitting in the absorption spectra of CuI thin films.[60-61] For the excitons consisting of holes of j_h=3/2, known as heavy-hole and light-hole excitons, they found a notable splitting into two lines (as shown in Figure 1.5) at lower temperatures. This splitting is due to the thermal strains caused by the different thermal expansion between CuI thin film and the sapphire substrate. More recently, they have reported a similar splitting in the PL spectrum of the CuI thin films on various substrates (NaCl, KCl) at 10 K.[61]

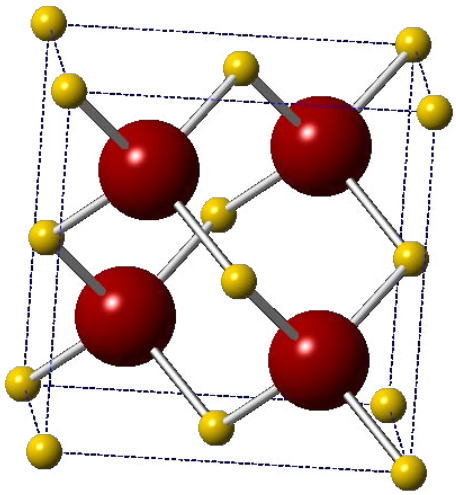

Figure 1.4. A unit cell of the zinc blende γ-CuI crystal structure. The larger red balls represent I atoms, and the smaller yellow balls represent Cu atoms.

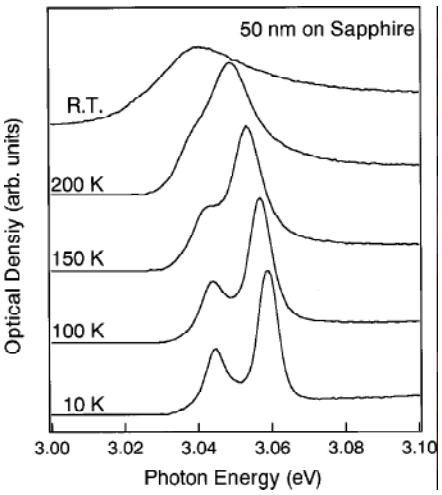

Figure 1.5. Temperature dependence of the absorption spectra for 50-nm thick CuI thin films grown on a sapphire substrate.[60]

1.1.3. Iron Oxides. Iron oxides are widespread in nature and readily synthesized in the laboratory. There are 16 iron compounds (including oxides, hydroxides, or oxide-hydroxides) composed of Fe with O and/or OH.

Magnetite (Fe_3O_4) is a black ferromagnetic mineral with the inverse spinel structure that contains both Fe(II) and Fe(III). Ferrihydrite is a reddish brown compound that occurs in surface environments. It is unstable and slowly transforms into more stable iron compounds. Its structure consists of hexagonal close packing anions and a mixture of defect-free and defective structure units. Maghemite (γ- Fe_2O_3) is a reddish brown ferromagnetic mineral that contains only Fe(III). It is isostructural with magnetite, but it has cation-deficient sites. Finally, hematite (α-Fe_2O_3) is one of the oldest known iron oxide minerals that is widespread in soil and rocks. It has a blood-red color when finely divided, and looks black or a sparkling grey if coarsely crystalline.

The Switzer group has shown that epitaxial magnetite thin films and superlattices can be electrodeposited on Au single crystal substrates from Fe(III)-TEA solutions at temperatures of 60 to 90 ^{o}C.[62-64] That work electrochemically reduced a complex of Fe(III) and triethanolamine (TEA) to Fe(II), which further reacts chemically with the Fe(III)-TEA complex in solution to produce Fe_3O_4. Stoichiometric magnetite thin films were deposited at an applied potential of -1.065 V versus Ag/AgCl. At potentials ranging from -1.01 to -1.07 V versus Ag/AgCl, nonstoichiometric magnetite was deposited. Therefore, defect chemistry superlattices based on Fe_3O_4 were deposited by pulsing two different potentials. At potentials from -1.10 to -1.20 V versus Ag/AgCl, nanoribbons of ferrihydrite were deposited. The production of ferrihydrite was unexpected because at more negative potentials the surface concerntration of Fe(II) is high, whereas ferrihydrite is an Fe(III)-rich compound with a formula of $Fe_{10}O_{14}(OH)_2$. The films deposited at -1.10 to -1.20 V versus Ag/AgCl were initially green rust, which is a mixture of Fe(II) and Fe(III) hydroxide, and they air-oxidized first to black and finally to reddish brown films.

Appendix C reports the progress that has been made in the thermal transformation of electrodeposited magnetite thin films into maghemite and hematite thin films, as well as to the thermal transformation of ferrihydrite nanoribbons into hematite thin films and nanoribbons.

1.1.3.1. Magnetite. Magnetite is a ferromagnetic material with an inverse spinel structure, space group $Fd\bar{3}m$. In each unit cell 32 O^{2-} are regularly close packed along the [111] direction. The formula of magnetite is written as $[Fe(III)]_{td}[Fe(II)Fe(III)]_{oc}O_4$, that is, Fe(II) and Fe(III) mixed ions occupy the octahedral sites, and Fe(III) is in the tetrahedral sites. Figure 1.6 shows a unit cell of magnetite crystal.

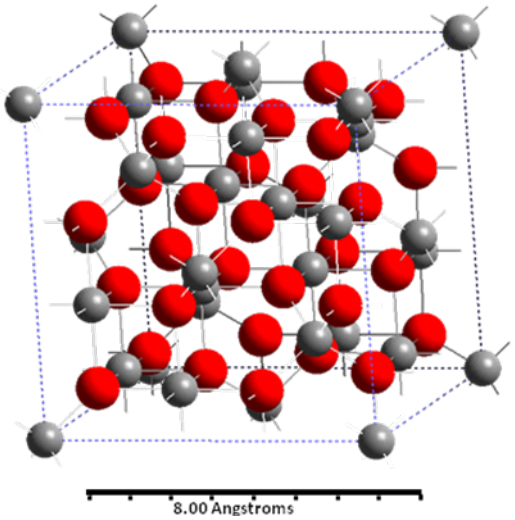

Figure 1.6. A unit cell of magnetite (Fe_3O_4) with an inverse spinel structure, space group $Fd\bar{3}m$.

Ferrimagnetism is observed below the Curie temperature of 860 K in magnetite, only due to the Fe^{2+} ions. Calculations have also indicated that the Fermi level electrons are 100% spin-polarized in this ferromagnetic phase.[65-66] In the ideal case of stoichiometric magnetite, the moments of the Fe(III) ions are antiferromagnetically coupled and the resulting magnetic moment is due to the Fe(II) in the cell. The electrical conductivity of this material at room temperature is reported to be the result of hopping of the charge carriers between the Fe(II) and Fe(III) ions in the octahedral sites.[66-67] As the temperature drops below 120 K, a metal to insulator transition known as the Verwey transition occurs.[68] This charge-ordered insulator has a magnetoelectronic effect, becoming ferroelectric below this Verwey temperature.[69-71]

1.1.3.2. Ferrihydrite. Ferrihydrite is an Fe(III)-rich oxyhydroxide compound with various reported formulas, such as $Fe_5HO_8 \cdot 4H_2O$, $5Fe_2O_3 \cdot 9H_2O$, and $Fe_2O_3 \cdot 2Fe$-

OOH_3•2.6H_2O.[72] Because of its poor crystalline quality, the X-ray powder diffraction patterns of ferrihydrite contain either 2 or 6 peaks. The ferrihydrite is thus labeled as 2-line or 6-line.[73] Ferrihydrite is superparamagnetic at room temperature.[72] Its blocking temperature, defined as the temperature at which 50% of the Mossbauer spectrum is magnetically split, is reported in the range of 25 to 115 K. At 4.2 K the spectra of ferrihydrite is speromagnetic ordering in which the spins freeze into a random non-collinear structure.[74-75] Ferrihydrite is observed in the corrosion of iron and steel and as a byproduct of mining. This nanomaterial that is also found in soil and sediments, naturally adsorbs cations, anions, and organic species such as insecticides and herbidices. Due to the small size of individual nanocrystals, ferrihydrite is a nanoporous material yielding large surface areas of several hundred m^2/g.[76-77] Because of this adsorption, ferrihydrite has been studied for the removal of heavy metals in water treatment and SO_2 emission.[72] It has also been suggested as the iron core of ferritin, an iron storage protein. Generally, this metastable material is made synthetically by rapid oxidation of Fe(II) or by hydrolysis of Fe(III) salts. It is then used as a precursor for the production of goethite and hematite.

1.1.3.3. Maghemite. Maghemite (γ-Fe_2O_3) has structure similar to that of magnetite, however all its cations are in a trivalent state. Each unit cell contains 32 closely packed O^{2-} ions, along with 21 1/3 Fe^{3+} ions and 2 1/3 vacancies. The vacancies are only in the octahedral sites. Eight cations occupy the tetrahedral sites, the remainder are randomly distributed over the octahedral sites. Maghemite forms by weathering or low-temperature oxidation of magnetite. It occurs as a widespread yellow pigment in terrestrial sediments and soils. It is often associated with magnetite and goethite.

Maghemite is ferromagnetic at room temperature. Measurement of Curie temperature (T_C) is difficult since maghemite transforms into hematite at temperatures of about 700-800 K. Murad has estimated the Curie temperature to be around 820-986 K.[78]

1.1.3.4. Hematite. Hematite (α-Fe_2O_3) is of the same structure as corundum. Its structure belongs to the rhombohedral system, with a space group of $R\bar{3}c$. Hematite is paramagnetic at above 956 K (T_C). At room temperature, it is weakly ferromagnetic and at 260 K (the Morin temperature, T_M), it undergoes a phase transition to an antiferromagnetic state. Particles smaller than 8 nm show superparamagnetic relaxation at room temperature.

Hematite has a band gap of 2.2 eV, which lies in the visible region allowing absorption of 38% of the photons in the solar spectrum.[79] It has long-term chemical stability in aqueous solutions over a wide pH range. However, some drawbacks of this material limit its applications. For instance, its photoresponse is quite low because of its high resistivity and fast recombination of photogenerated charge carriers.[80]

1.2. THIN FILM DEPOSITION BY SOLUTION METHODS

This dissertation comprises two papers (Pare I and II) concerning the chemical bath deposition of ZnO nanostructures and epitaxial films. Paper III addresses the electrodeposition of epitaxial CuI thin films on Au(100). Appendix II concerns the electrodeposition of ZnO nanocolumns from alkaline solutions using various amino acids. Finally, Appendix III discusses the thermal production of Fe_2O_3 from electrodeposited magnetite thin films and ferrihydrite nanoribbons. In this section, the electrodeposition and chemical bath deposition method will be discussed.

1.2.1. Electrodeposition. Electrodeposition is a means synthesizing materials onto conductive substrates by applying an electrical potential or current. It is a versatile method of depositing metals,[81-83] metal oxides,[84-85] semiconductors,[86] and biomaterials.[87]

Compared with other techniques, electrodeposition is simple and offers various advantages, especially it is low cost and environmental friendly, and it can be worked at low temperatures and under ambient pressures. With this method, materials with complex compositions (such as superlattices and multilayers) can be deposited by controlling the overpotential.[62, 88-89] In addition, the rate of deposition can be precisely tuned by varying the applied current.[90] Further, the method offers capability to change the characteristics of the deposits by varying factors such as electrolyte composition, pH value, and deposition temperature. Electrodeposition has disadvantages though. First, the electrochemical process requires a conductive substrate to serve as the working electrode (WE) in the deposition cell, thus preventing its application on some semiconductor or insulting substrates. Similarly, if the deposited material is highly resistive, the thickness of the film will be limited.[91]

In this dissertation, two types of mechanisms were used for electrodeposition of materials. One is to electrochemically oxidize or reduce the ions at the vicinity of WE; the ions, thus produced ions react chemically with species in the solution to form the final product on the WE. The electrodeposition of Fe_3O_4[63] and CuI belong to this category. The deposition of Fe_3O_4 is described in Equations 1 and 2, where TEA is triethanolamine, an Fe(III) complexing agent. Equation 1 is a one-electron reduction of Fe(III)-TEA complex to Fe(II)-TEA complex. The Fe(II)-TEA complex then chemically reacts with the Fe(III)-TEA complex in the solution to form Fe_3O_4.

$$Fe(OH)_4(TEA)_2^- + e^- \rightarrow Fe(TEA)_2^{2+} + 4OH^- \quad (1)$$

$$2Fe(OH)_4(TEA)_2^- + Fe(TEA)_2^{2+} \rightarrow Fe_3O_4 + 4H_2O \quad (2)$$

In the case of CuI deposition, Cu(II)-EDTA complexes are first electrochemically reduced to Cu(I) ions (Equation 3), then the Cu(I) chemically reacts with I^- in the solution to produce CuI (Equation 3).

$$Cu(EDTA)^{2+} + e^- \rightarrow Cu^+ + EDTA \quad (3)$$

$$Cu^+ + I^- \rightarrow CuI \quad (4)$$

A second method to produce films is to electrochemically change the solution pH at the WE surface. Since the solubility of a material is dependent on pH, thus the local pH change may lower the solubility in the vicinity of the electrode and induce the precipitation of a material only on the electrode surface. A good example is ZnO, nanocolumns of which can be deposited from O_2 saturated $ZnCl_2$ solution.[85] Before deposition, the Zn(II) cation is stable in the solution. The dissolved O_2 is electrochemicaly reduced to generate OH^- ions and increase the local pH at the electrode surface (Equation 5). Then ZnO is deposited on the surface of the electrode due to the excess of saturation state of Zn(II) in the solution (Equation 6).

$$O_2 + 2H_2O + e^- \rightarrow 4OH^- \quad (5)$$

$$Zn^{2+} + 2OH^- \rightarrow ZnO + H_2O \quad (6)$$

On the other hand, as an amphoteric compound, ZnO is also dissolvable in alkaline solutions. From a solution containing $Zn(NO_3)_2$ and NaOH, electrochemical oxidation of ascorbic acid[84] can result in the decrease of local pH and induce the precipitation of ZnO, as shown by Equations 7 and 8.

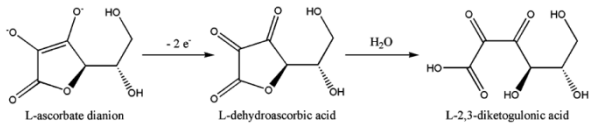

(7)

$$Zn(OH)_4^{2-} + 2H^+ \rightarrow ZnO + 3H_2O \quad (8)$$

1.2.2. Chemical Bath Deposition. Like electrodeposition, chemical bath deposition (CBD), also known as chemical solution deposition, or simply chemical deposition, is also a simple and lost-cost thin film deposition method that works at low temperatures and ambient pressures.

It requires only a solution that contains precursor ions or complexes and a substrate on which films are deposited. It is scalable, and thus applicable to large-area batch processing or continuous deposition. None of the deposition solution, substrate, or film is required to be electronic conductive. One drawback of this method is that the solution is wasted after every deposition. Additionally, the deposited materials often need post thermal treatment to form the final product that exhibits the desired properties.

Over the last several decades, the CBD method has been intensively studied for preparation of semiconductor materials including sulfides (CdS,[92] In_2S_3,[93] Sb_2S_3,[94] HgS,[95] Bi_2S_3,[96] CuS,[97] SnS[86,98]), selenides (PbSe,[99] ZnSe,[100] Cu_xSe,[101-103] CdSe,[104] $CdInSe_2$[105]), and oxides (Cu_2O,[106] CuO,[106] TiO_2,[107] ZnO,[108-111] NiO,[112] $BaWO_4$[113]).

The mechanism for chemical deposition of sulfides and selenides usually involves a controlled release of one reactant ion from its precursor complex. When the ion is released, it reacts chemically with the other reactant to form the desired product. For example, in the case of Cu_2Se deposition from aqueous solutions containing $CuSO_4$, $Na_3C_6H_5O_7$, Na_2SO_3, NaOH, and selenium granules.[114] The citrate ($Na_3C_6H_5O_7$) is used

to complex Cu(II) in the solution, and the Cu(I) ion is slowly released by a slow chemical redox reaction as shown in Equation 9. Then produced Cu(I) ions reacts with $SeSO_3^{2-}$ and form Cu_2Se thin film (Equation 10).

$$SO_3^{2-} + 2Cu^{2+} + 2OH^- \rightarrow SO_4^{2-} + 2Cu^+ + H_2O \quad (9)$$

$$Cu^+ + SeSO_3^{2-} + 2OH^- \rightarrow Cu_2Se + SO_4^{2-} + H_2O \quad (10)$$

As for the deposition of ZnO, in 2004 Peterson et al. proposed the chemical bath deposition of ZnO on ZnO seeded substrates from alkaline solutions.[108] This method requires no complexing agents and produces ZnO thin films in less than 1 hour. The ZnO deposits simply due to the slight excess of saturation state of Zn(II) in the solution. The solution system is thermodynamically unstable. The deposition process is kinetically sluggish, as a result, the ZnO grows on the substrate. Papers I and II in this dissertation report the use of this method to deposit epitaxial nanostrucutres of ZnO on the single crystalline Si and Au substrates. Appendix A presents the detailed thermodynamic calculations of the saturation state of Zn(II) aqueous solution.

1.3. THIN FILM CHARACTERIZATION

1.3.1. X-ray Diffraction Technique. XRD technique is a powerful method to characterize films and thus to determine the epitaxial relationships between the films and substrates. Diffraction, the constructive interfere of the X-ray beam, occurs only when the X-ray wavelength and the distance between the atomic planes in a crystal satisfy Bragg's Law:

$$n\lambda = 2d_{hkl}\sin\theta \quad (11)$$

where, n is an integer (1, 2, 3, etc), and λ is the wavelength in unit of Å, dependent on the X-ray source (e.g. 1.54 Å for $Cu_{k\alpha}$), d_{hkl} is the distance between atomic layers in Å, and θ is the diffraction angle in degrees or radiens.

Typically, an XRD pattern is a plot of intensity versus 2θ value. Each angle of diffraction (θ) corresponds to a set of atomic planes {*hkl*} (see Bragg's Law). Every crystalline material has its unique fingerprint XRD pattern. A pattern of a randomly oriented film deposited on polycrystalline substrate is usually used to identify the material and determine its crystallinity, because the crystals grown in various orientations show multiple reflection peaks in the XRD pattern. In addition, broad peaks found in some patterns can be used to determine the particle size and residual strain by Williamson-Hall analysis.

Besides polycrystalline substrates and randomly oriented films, single crystalline substrates and epitaxial layers are often studied. As mentioned above, epitaxial deposits grow with both out-of-plane and in-plane orientations that are dependent on those of the substrate. To characterize an epitaxial film, multiple XRD techniques are often combined, such as X-ray diffraction patterns, pole figures, azimuthal scans, and rocking curves. The X-ray diffraction pattern for an epitaxial layer on a single crystalline substrate is different from that of a polycrystalline film on a polycrystalline substrate, as illustrated in Figure 1.7. Poly crystalline films have all the possible orientations, resulting in multiple peaks in the pattern. On the other hand, epitaxial films normally grow with only one orientation and show only a family of planes in the pattern. In Figure 1.7, the ZnO sample deposited on an Au-glass substrate (upper) shows all the possible peaks, with both peak positions and relative intensities coincident with its fingerprint pattern. The ZnO sample deposited

on Au(110) single crystalline substrate shows only ZnO (0002) and (0004) peaks, which belong to the {0001} family planes.

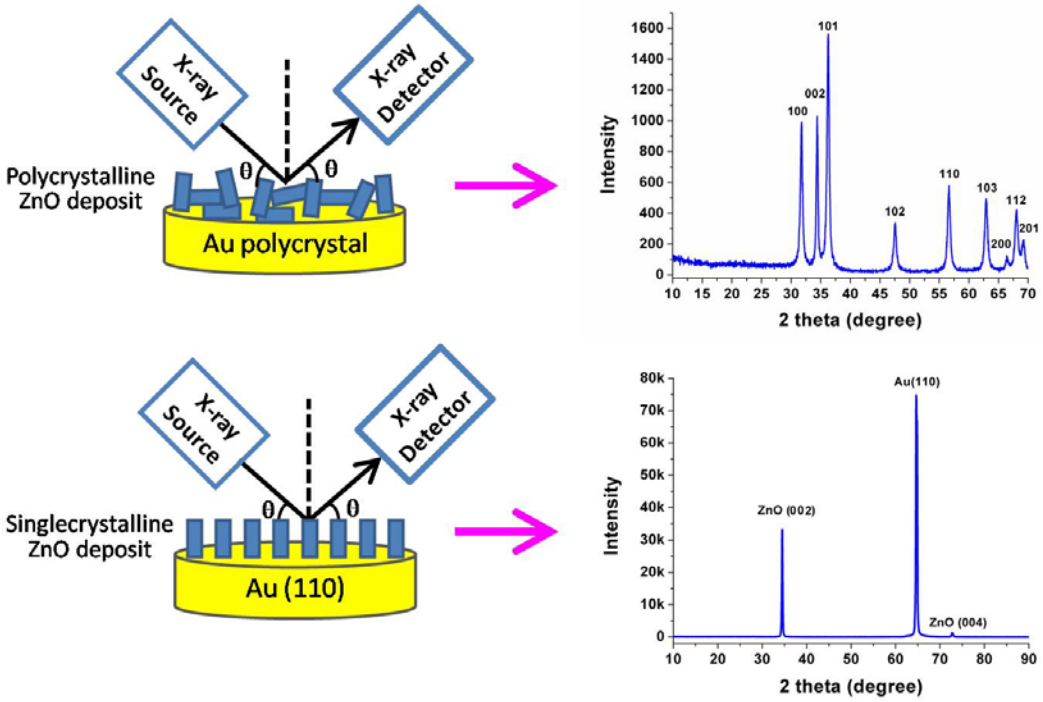

Figure 1.7. Setup (left) used to acquire X-ray diffraction patterns, and the resulting XRD patterns of a polycrystalline zinc oxide film (right, upper) deposited on an Au-sputtered microslide substrate and a epitaxial zinc oxide film (right, lower) deposited on an Au(110) single crystalline substrate. Both films were deposited by chemical bath deposition method from a solution containing 0.25 M of NaOH and 10 mM of $Zn(NO_3)_2$ at 70 ^oC for 30 minutes.

One strong out-of-plane texture, however, does not constitute sufficient proof of epitaxy. An epitaxial film should be aligned both out-of-plane and in-plane. The X-ray pole figure technique is a method to reveal both out-of-plane and in-plane epitaxial relationships between film and its substrate. A pole figure is actually a graphical representation of the orientation of objects in space. Figure 1.8 illustrates the set-up used to acquire pole figures and shows the pole figures that were collected on a ZnO(0001) on

Au(110) substrate. In this example, both the ZnO $(10\bar{1}1)$ pole figure and Au(111) substrate pole figures were run. To produce the ZnO$(10\bar{1}1)$ pole figure, 2θ of 35.379^{o} was chosen for the ZnO$(10\bar{1}1)$ plane to set up the X-ray source and detector. The sample surface was then tilted over an angle (χ) from 0-90^{o} and rotated azimuthally (φ) from 0-360^{o} at each tilt angle. In a pole figure, the radial grid lines correspond to 30^{o} increments in tilt angle (χ). The color of the spots differentiates the diffracted intensity. The resulting ZnO $(10\bar{1}1)$ pole figure shows six equally spaced spots at χ=62^{o}, which is one set of ZnO$(10\bar{1}1)$ reflections onto the ZnO(0001) plane (six-fold symmetry). The Au(111) substrate pole figure was acquired by setting the X-ray source and detector at 2θ of 38.184^{o} for the Au(111) plane, and then tilting (χ) and rotating (φ) the sample as mentioned above. The resulting pole figure has two spots at χ=56.9^{o}, corresponding to one set of Au(111) reflections to the Au(110) plane (two-fold symmetry). By comparing the pole figure to its calculated stereographic projection (a process discussed in a section below), the epitaxial relationship between the ZnO deposit and Au substrate can be determined. For ZnO(0001) on Au(110) substrate, the epitaxial relationship is ZnO(0001)$[10\bar{1}1]$ //Au(110)[001], which means that the ZnO(0001) and Au(110) planes are parallel, and the ZnO$[10\bar{1}1]$ and Au[001] in-plane directions are coincident.

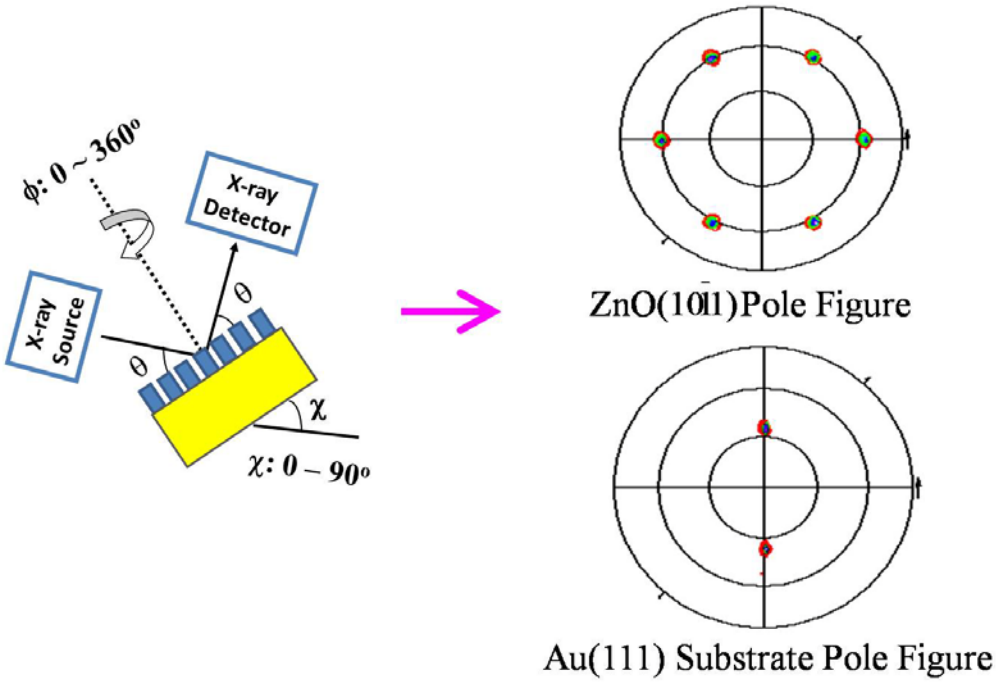

Figure 1.8. Setup used to acquire X-ray pole figure (left) and the resulting pole figures for a (0001) oriented zinc oxide film (right, upper) deposited on Au(110) single crystalline substrate and its correspondent substrate pole figure (right, lower). The ZnO was deposited by chemical bath deposition method from a solution containing 0.25 M of NaOH and 10 mM of $Zn(NO_3)_2$ at 70 ^oC for 30 minutes.

A ploycrystalline sample with no preferred out-of-plane or in-plane orientation has no peaks in the pole figure, because it has equal intensity at all tiling and azimuthal angles, and thus produces no outstanding peak for one particular angle. The pole figure shows a ring pattern of a sample with the preferred out-of-plane but random in-plane orientations (known as fiber texture). That can be understood by rotating and overlaying multiple pole figures of an epitaxial sample (like that shown in Figure 1.8), therefore the separated spots in the pole figure are finally connected with one another into a ring pattern.

1.3.2. X-ray Stereographic Projection. The stereographic projection is a planar drawing that accurately displays the angular relationship between lattice planes and directions. It is employed to understand X-ray pole figures. To produce a stereographic projection, a single crystal is placed at the center of an imaginary sphere. Each plane normal of this crystal intersects the surface of the sphere at a point called a *pole*. As a result, the plane orientations of this crystal can be represented by a point in the sphere, and the interplane angle (α) between any two planes is evidently equal to the angle between their poles. A planar circle, however, is more convenient for measuring angles than a sphere surface. Hence, a planar equiangular stereographic projection is generated to represent the spherical surface. The most important feature of the equiangular stereographic projection is that it preserves angular relationships faithfully although distorting areas. As shown in Figure 1.9, a circle with latitude and longitude lines is called a Wulff net. The Wulff net in Figure 1.9 gives an accuracy of 10^{o} in both latitude and longitude directions. The measurement of an angle between two crystal planes is thus transformed into the measurement of the angle between the poles of these two planes, for instance, between planes A and B, C and D, or E and F.

Figure 1.10 shows an actual (0001) stereographic projection of a ZnO crystal. It is generated with CaRIne Crystallography 3.1 software by placing the (0001) pole at the center and selecting as projection planes some family planes with low indices as the plane for projection, such as $\{10\bar{1}0\}$, $\{10\bar{1}1\}$, $\{10\bar{1}2\}$, $\{11\bar{2}0\}$, and $\{21\bar{3}0\}$. From this stereographic projection, the inter-planar angles between any two planes can be simply determined. For each family of planes, six equally spaced reflections are found, due to the six-fold symmetry along [0001] directions of the hexagonal crystal structure.

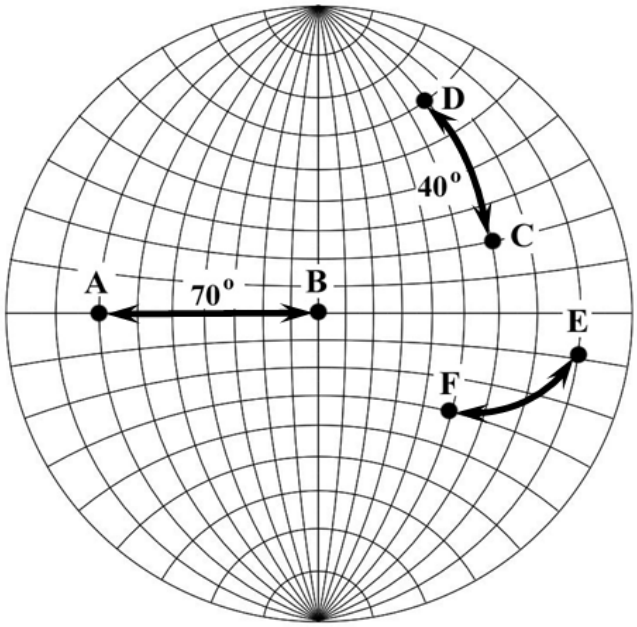

Figure 1.9. Stereographic projection superimposed a Wulff net with 10^{o} intervals for measurement of the angle between poles.

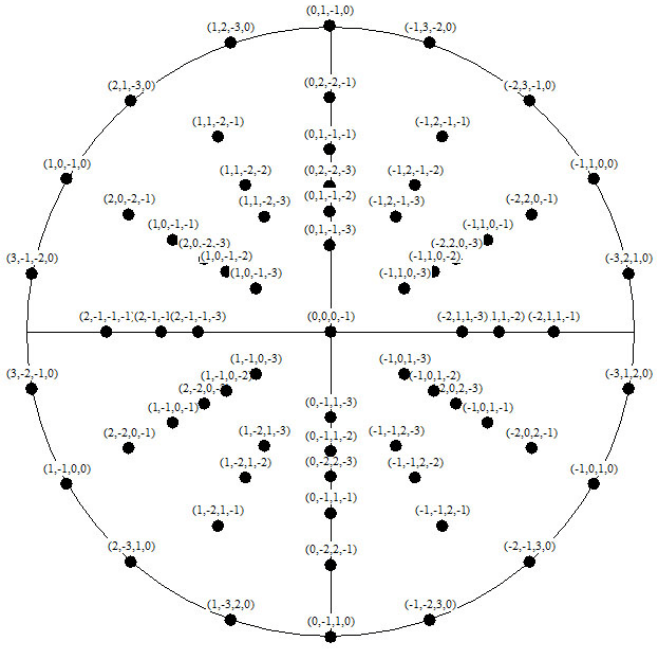

Figure 1.10. The (0001) stereographic projection of ZnO (hexagonal, a = 3.2498 Å, c = 5.2066 Å).

1.3.3. Rhombohedral-Hexagonal Transformation. To generate a stereographic projection and properly understand the XRD analysis results for a crystal with a hexagonal structure, a rhombohedral-hexagonal transformation is necessary. Commonly, the indices of planes and directions used in the hexagonal system are Miller-Bravais indices, which differ from the three-fold Miller indices used for other crystal systems.

As illustrated in Figure 1.11, the hexagonal unit cell has three coplanar axes, $\mathbf{a_1}$, $\mathbf{a_2}$, and $\mathbf{a_3}$ that are separated by 120^o from one another, as well as a **c** axis perpendicular to the basal plane. The inner primitive rhombohedral unit cell, on the other hand, has three axes, $\mathbf{b_1}$, $\mathbf{b_2}$, and $\mathbf{b_3}$. The lattice points in the rhombohedral cell can be referred to as a hexagonal cell. The hexagonal cell is no longer primitive, because it contains three lattice points per unit cell at (0, 0, 0), (2/3, 1/3, 1/3), and (1/3, 2/3, 2/3). It also has three times the volume of the inner rhombohedral cell. To determine the lattice parameters (a_R and α) for the rhombohedral unit cell according to its correspondent hexagonal ones (a_H and c), the following equations may be used:

$$a_R = \frac{\sqrt{(3a_H^2 + c^2)}}{3} \tag{12}$$

$$\sin(\frac{\alpha}{2}) = \frac{3}{2\sqrt{3 + \left(\frac{c}{a_H}\right)^2}} \tag{13}$$

when the c/a_H ratio in these equations equals 2.45, the α for the resulting rhombohedral cell will be equal to 60^o, which means the lattice is face-centered cubic.

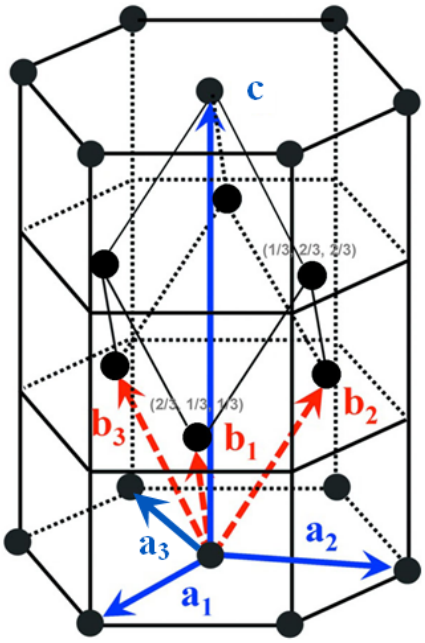

Figure 1.11. Illustration of relationships between rhombohedral and hexagonal unit cells.

If one knows the three-fold indices (h'k'l') of a plane referred to the rhombohedral system, then its four-fold hexagonal indices (hkil) can be obtained with the following equations:

$$h = h' - k' \tag{14}$$

$$k = k' - l' \tag{15}$$

$$l = h' + k' + l' \tag{16}$$

$$i = -(h + k) \tag{17}$$

The inverse transforming relations are:

$$h' = \frac{(2h + k + l)}{3} \tag{18}$$

$$k' = \frac{(-h + k + l)}{3} \tag{19}$$

$$l' = \frac{(-h - 2k + l)}{3} \tag{20}$$

For instance, the $\{11\bar{2}0\}$ family of planes in a hexagonal system includes six equivalent planes of $(11\bar{2}0),(1\bar{2}10),(\bar{2}110),(\bar{1}\bar{1}20),(\bar{1}2\bar{1}0)$, and $(2\bar{1}\bar{1}0)$. Once transformed in a rhombohedral index notation, it would be {110}, including (110), $(\bar{1}20),(\bar{2}10),(\bar{1}\bar{1}0),(1\bar{2}0)$, and $(2\bar{1}0)$.

For directions, the Miller-Bravais indices [uvtw] can be obtained from its Miller indices [u'v'w'] with the following equations:

$$u = \frac{(2u' - v')}{3} \tag{21}$$

$$v = \frac{(2v' - u')}{3} \tag{22}$$

$$t = \frac{-(u' + v')}{3} = -(u + v) \tag{23}$$

$$w = w' \tag{24}$$

The inverse transformations are:

$$u' = 2u + v \tag{25}$$

$$v' = 2v + u \tag{26}$$

$$w' = w \tag{27}$$

For example, the [100] direction in Miller-Bravais indices is $[2\bar{1}\bar{1}0]$; the [111] direction is $[11\bar{2}3]$; and the [211] direction is $[10\bar{1}1]$.

1.3.4. Other Film Characterization Techniques. Many other techniques are used to characterize the thin films. In this dissertation, the film morphology, particle size, and cross-sectional film thickness is observed using SEM. Along with SEM, energy-dispersive spectroscopy (EDS) is used to determine the elemental compositions in the films. The EDS shows the peaks at a particular energy level for an element, and its intensity indicates the amount of the element existing in the sample. Besides SEM, atomic force microscopy (AFM) can also be used to measure thin film thickness, morphology, as well as grain size. In addition, PL spectroscopy is used to determine the optical properties of the thin film, and Raman spectroscopy is used to reveal the crystal dynamics of the deposits. For this dissertation, XRD and SEM techniques were used to characterize all films. The other techniques mentioned above were used in some cases depending on the chemical compositions and physical properties of the material.

REFERENCES

1. Reynolds, D. C.; Look, D. C.; Jogai, B.; Litton, C. W.; Collins, T. C.; Harsch, W.; Cantwell, G., Neutral-donor-bound-exciton complexes in ZnO crystals. *Physical Review B: Condensed Matter and Materials Physics* **1998,** 57, (19), 12151-12155.
2. Look, D. C., Recent advances in ZnO materials and devices. *Materials Science and Engineering B: Solid-State Materials for Advanced Technology* **2001,** 80, (1-3), 383-387.
3. Reynolds, D. C.; Look, D. C.; Jogai, B.; Litton, C. W.; Cantwell, G.; Harsch, W. C., Valence-band ordering in ZnO. *Physical Review B: Condensed Matter and Materials Physics* **1999,** 60, (4), 2340-2344.
4. Bayram, C.; Teherani, F. H.; Rogers, D. J.; Razeghi, M., A hybrid green light-emitting diode comprised of n-ZnO/(InGaN/GaN) multi-quantum-wells/p-GaN. *Applied Physics Letters* **2008,** 93, (8), 081111/1-081111/3.
5. Guo, H.; Lin, Z.; Feng, Z.; Lin, L.; Zhou, J., White-Light-Emitting Diode Based on ZnO Nanotubes. *Journal of Physical Chemistry C* **2009,** 113, (28), 12546-12550.
6. Liang, H. K.; Yu, S. F.; Yang, H. Y., Directional and controllable edge-emitting ZnO ultraviolet random laser diodes. *Applied Physics Letters* **2010,** 96, (10), 101116/1-101116/3.
7. Yadav, H. K.; Sreenivas, K.; Gupta, V., ZnO-Sn bilayer ultraviolet (UV) photon detector with improved responsitivity. *Materials Research Society Symposium Proceedings* **2007,** 957, (Zinc Oxide and Related Materials), 195-200.
8. Li, Y.; Della Valle, F.; Simonnet, M.; Yamada, I.; Delaunay, J.-J., High-performance UV detector made of ultra-long ZnO bridging nanowires. *Nanotechnology* **2009,** 20, (4), 045501/1-045501/5.
9. Zhou, J.; Fei, P.; Gu, Y.; Mai, W.; Gao, Y.; Yang, R.; Bao, G.; Wang, Z. L., Piezoelectric-Potential-Controlled Polarity-Reversible Schottky Diodes and Switches of ZnO Wires. *Nano Letters* **2008,** 8, (11), 3973-3977.
10. Xi, Y.; Song, J.; Xu, S.; Yang, R.; Gao, Z.; Hu, C.; Wang, Z. L., Growth of ZnO nanotube arrays and nanotube based piezoelectric nanogenerators. *Journal of Materials Chemistry* **2009,** 19, (48), 9260-9264.
11. Mantini, G.; Gao, Y.; D'Amico, A.; Falconi, C.; Wang, Z. L., Equilibrium piezoelectric potential distribution in a deformed ZnO nanowire. *Nano Research* **2009,** 2, (8), 624-629.
12. Fleischhaker, F.; Wloka, V.; Hennig, I., ZnO based field-effect transistors (FETs): solution-processable at low temperatures on flexible substrates. *Journal of Materials Chemistry* **2010,** 20, (32), 6622-6625.

13. Yebo, N. A.; Lommens, P.; Hens, Z.; Baets, R., An integrated optic ethanol vapor sensor based on a silicon-on-insulator microring resonator coated with a porous ZnO film. *Optics Express* **2010,** 18, (11), 11859-11866.

14. Zhang, C.; Wang, G.; Liu, M.; Feng, Y.; Zhang, Z.; Fang, B., A hydroxylamine electrochemical sensor based on electrodeposition of porous ZnO nanofilms onto carbon nanotubes films modified electrode. *Electrochimica Acta* **2010,** 55, (8), 2835-2840.

15. Dimova-Malinovska, D.; Angelov, O.; Nichev, H.; Lasarova, V.; Pivin, J. C., ZnO:H thin films for room temperature selective NH3 gas sensor. *Nanoscience & Nanotechnology* **2007,** 7, 101-104.

16. Ichimura, M.; Takagi, H., Electrodeposited ZnO/SnS heterostructures for solar cell application. *Japanese Journal of Applied Physics* **2008,** 47, (10, Pt. 1), 7845-7847.

17. Labat, F.; Ciofini, I.; Hratchian, H. P.; Frisch, M.; Raghavachari, K.; Adamo, C., First Principles Modeling of Eosin-Loaded ZnO Films: A Step toward the Understanding of Dye-Sensitized Solar Cell Performances. *Journal of the American Chemical Society* **2009,** 131, (40), 14290-14298.

18. Zhang, W.; Zhu, R.; Liu, X.; Liu, B.; Ramakrishna, S., Facile construction of nanofibrous ZnO photoelectrode for dye-sensitized solar cell applications. *Applied Physics Letters* **2009,** 95, (4), 043304/1-043304/3.

19. Chen, C.-P.; Lin, P.-H.; Chen, L.-Y.; Ke, M.-Y.; Cheng, Y.-W.; Huang, J., Nanoparticle-coated n-ZnO/p-Si photodiodes with improved photoresponsivities and acceptance angles for potential solar cell applications. *Nanotechnology* **2009,** 20, (24), 245204/1-245204/6.

20. Limaye, M. V.; Singh, S. B.; Date, S. K.; Gholap, R. S.; Kulkarni, S. K., Epitaxially grown zinc-blende structured Mn doped ZnO nanoshell on ZnS nanoparticles. *Materials Research Bulletin* **2009,** 44, (2), 339-344.

21. Ashrafi, A. B. M. A.; Ueta, A.; Avramescu, A.; Kumano, H.; Suemune, I.; Ok, Y.-W.; Seong, T.-Y., Growth and characterization of hypothetical zinc-blende ZnO films on GaAs(001) substrates with ZnS buffer layers. *Applied Physics Letters* **2000,** 76, (5), 550-552.

22. Lazzarini, L.; Salviati, G.; Fabbri, F.; Zha, M.; Calestani, D.; Zappettini, A.; Sekiguchi, T.; Dierre, B., Unpredicted nucleation of extended zinc blende phases in wurtzite ZnO nanotetrapod arms. *ACS nano* **2009,** 3, (10), 3158-64.

23. Ding, Y.; Wang, Z. L.; Sun, T.; Qiu, J., Zinc-blende ZnO and its role in nucleating wurtzite tetrapods and twinned nanowires. *Applied Physics Letters* **2007,** 90, (15), 153510/1-153510/3.

24. Recio, J. M.; Blanco, M. A.; Luana, V.; Pandey, R.; Gerward, L.; Olsen, J. S., Compressibility of the high-pressure rocksalt phase of ZnO. *Physical Review B: Condensed Matter and Materials Physics* **1998,** 58, (14), 8949-8954.

25. Aoumeur, F. Z.; Benkabou, K.; Belgoumene, B., Structural and dynamical properties of ZnO in zinc-blende and rocksalt phases. *Physica B: Condensed Matter (Amsterdam, Netherlands)* **2003,** 337, (1-4), 292-297.

26. Boulfelfel, S. E.; Leoni, S., Competing intermediates in the pressure-induced wurtzite to rocksalt phase transition in ZnO. *Physical Review B: Condensed Matter and Materials Physics* **2008,** 78, (12), 125204/1-125204/7.

27. Laudise, R. A.; Ballman, A. A., Hydrothermal synthesis of zinc oxide and zinc sulfide. *Journal of Physical Chemistry* **1960,** 64, 688-91.

28. Chelikowsky, J. R., An oxygen pseudopotential: application to the electronic structure of zinc oxide. *Solid State Communications* **1977,** 22, (6), 351-4.

29. Ivanov, I.; Pollmann, J., Electronic structure of ideal and relaxed surfaces of zinc oxide: A prototype ionic wurtzite semiconductor and its surface properties. *Physical Review B: Condensed Matter* **1981,** 24, (12), 7275-96.

30. Jaffe, J. E.; Snyder, J. A.; Lin, Z.; Hess, A. C., LDA and GGA calculations for high-pressure phase transitions in ZnO and MgO. *Physical Review B: Condensed Matter and Materials Physics* **2000,** 62, (3), 1660-1665.

31. Vogel, D.; Krueger, P.; Pollmann, J., Ab initio electronic-structure calculations for II-VI semiconductors using self-interaction-corrected pseudopotentials. *Physical Review B: Condensed Matter* **1995,** 52, (20), R14316-R14319.

32. Xu, Y. N.; Ching, W. Y., Electronic, optical, and structural properties of some wurtzite crystals. *Physical Review B: Condensed Matter* **1993,** 48, (7), 4335-51.

33. Lu, J. G.; Fujita, S.; Kawaharamura, T.; Nishinaka, H.; Kamada, Y.; Ohshima, T.; Ye, Z. Z.; Zeng, Y. J.; Zhang, Y. Z.; Zhu, L. P.; He, H. P.; Zhao, B. H., Carrier concentration dependence of band gap shift in n-type ZnO:Al films. *Journal of Applied Physics* **2007,** 101, (8), 083705/1-083705/7.

34. Lopatiuk-Tirpak, O.; Schoenfeld, W. V.; Chernyak, L.; Xiu, F. X.; Liu, J. L.; Jang, S.; Ren, F.; Pearton, S. J.; Osinsky, A.; Chow, P., Carrier concentration dependence of acceptor activation energy in p-type ZnO. *Applied Physics Letters* **2006,** 88, (20), 202110/1-202110/3.

35. Kim, C. E.; Moon, P.; Kim, S.; Myoung, J.-M.; Jang, H. W.; Bang, J.; Yun, I., Effect of carrier concentration on optical bandgap shift in ZnO:Ga thin films. *Thin Solid Films* **2010,** 518, (22), 6304-6307.

36. Jung, M. N.; Lee, E. S.; Jeon, T. I.; Gil, K. S.; Kim, J. J.; Murakami, Y.; Lee, S. H.; Park, S. H.; Lee, H. J.; Yao, T.; Makino, H.; Chang, J. H., Synthesis and investigation on the extrinsic carrier concentration of indium doped ZnO tetrapods. *Journal of Alloys and Compounds* **2009,** 481, (1-2), 649-653.

37. Ip, K.; Heo, Y. W.; Baik, K. H.; Norton, D. P.; Pearton, S. J.; Ren, F., Carrier concentration dependence of Ti/Al/Pt/Au contact resistance on n-type ZnO. *Applied Physics Letters* **2004,** 84, (4), 544-546.

38. Grossner, U.; Christensen, J. S.; Svensson, B. G.; Kuznetsov, A. Y., Carrier concentration and shallow electron states in In-doped hydrothermally grown ZnO. *Superlattices and Microstructures* **2005,** 38, (4-6), 364-368.

39. Chatman, S.; Emberley, L.; Poduska, K. M., Significant Carrier Concentration Changes in Native Electrodeposited ZnO. *ACS Applied Materials & Interfaces* **2009,** 1, (10), 2348-2352.

40. Cheng, C.; Liu, B.; Sie, E. J.; Zhou, W.; Zhang, J.; Gong, H.; Huan, C. H. A.; Sum, T. C.; Sun, H.; Fan, H. J., ZnCdO/ZnO Coaxial Multiple Quantum Well Nanowire Heterostructures and Optical Properties. *Journal of Physical Chemistry C* **2010,** 114, (9), 3863-3868.

41. Kuznetsov, P.; Lusanov, V.; Yakushcheva, G.; Jitov, V.; Zakharov, L.; Kotelyanskii, I.; Kozlovsky, V., MOVPE growth and study of ZnO, ZnMgO epilayers and ZnO/ZnMgO MQW structures. *Physica Status Solidi C: Current Topics in Solid State Physics* **2010,** 7, (6), 1568-1570.

42. Yousefi, R.; Jamali Sheini, F.; Muhamad, M. R.; More, M. A., Characterization and field emission properties of ZnMgO nanowires fabricated by thermal evaporation process. *Solid State Sciences* **2010,** 12, (7), 1088-1093.

43. Kim, I.-S.; Lee, B.-T., Structural and optical properties of single-crystal ZnMgO thin films grown on sapphire and ZnO substrates by RF magnetron sputtering. *Journal of Crystal Growth* **2009,** 311, (14), 3618-3621.

44. Sadofev, S.; Schaefer, P.; Fan, Y. H.; Blumstengel, S.; Henneberger, F.; Schulz, D.; Klimm, D., Radical-source molecular beam epitaxy of ZnMgO and ZnCdO alloys on ZnO substrates. *Applied Physics Letters* **2007,** 91, (20), 201923/1-201923/3.

45. Mari, B.; Tortosa, M.; Mollar, M.; Bosca, J. V.; Cui, H. N., Electrodeposited ZnCdO thin films as conducting optical layer for optoelectronic devices. *Optical Materials (Amsterdam, Netherlands)* **2010,** 32, (11), 1423-1426.

46. Tortosa, M.; Mollar, M.; Mari, B., Synthesis of ZnCdO thin films by electrodeposition. *Journal of Crystal Growth* **2007,** 304, (1), 97-102.

47. Sadofev, S.; Blumstengel, S.; Cui, J.; Puls, J.; Rogaschewski, S.; Schaefer, P.; Henneberger, F., Visible band-gap ZnCdO heterostructures grown by molecular beam epitaxy. *Applied Physics Letters* **2006,** 89, (20), 201907/1-201907/3.

48. Meyer, B. K.; Alves, H.; Hofmann, D. M.; Kriegseis, W.; Forster, D.; Bertram, F.; Christen, J.; Hoffmann, A.; Strassburg, M.; Dworzak, M.; Haboeck, U.; Rodina, A. V., Bound exciton and donor-acceptor pair recombinations in ZnO. *Physica Status Solidi B: Basic Research* **2004,** 241, (2), 231-260.

49. Shan, Y.; Li, G.; Tian, G.; Han, J.; Wang, C.; Liu, S.; Du, H.; Yang, Y., Description of the phase transitions of cuprous iodide. *Journal of Alloys and Compounds* **2009,** 477, (1-2), 403-406.

50. Darlington, C. N. W., Atomic vibrations in cuprous iodide. *Journal of Physics C: Solid State Physics* **1986,** 19, (26), 5095-102.

51. Zheng-Johansson, J. X. M.; Ebbsjoe, I.; McGreevy, R. L., A molecular dynamics study of ionic conduction in CuI. I. Derivation of the interionic potential from dynamic properties. *Solid State Ionics* **1995,** 82, (3,4), 115-22.

52. Zheng-Johansson, J. X. M.; McGreevy, R. L., A molecular dynamics study of ionic conduction in CuI. II. Local ionic motion and conduction mechanisms. *Solid State Ionics* **1996,** 83, (1,2), 35-48.

53. Dhere, S. L.; Latthe, S. S.; Kappenstein, C.; Mukherjee, S. K.; Rao, A. V., Comparative studies on p-type CuI grown on glass and copper substrate by SILAR method. *Applied Surface Science* **2010,** 256, (12), 3967-3971.

54. O'Regan, B. C.; Lenzmann, F., Charge Transport and Recombination in a Nanoscale Interpenetrating Network of n-Type and p-Type Semiconductors: Transient Photocurrent and Photovoltage Studies of TiO2/Dye/CuSCN Photovoltaic Cells. *Journal of Physical Chemistry B* **2004,** 108, (14), 4342-4350.

55. Tate, J.; Ju, H. L.; Moon, J. C.; Zakutayev, A.; Richard, A. P.; Russell, J.; McIntyre, D. H., Origin of p-type conduction in single-crystal CuAlO2. *Physical Review B: Condensed Matter and Materials Physics* **2009,** 80, (16), 165206/1-165206/8.

56. Rusop, M.; Shirata, T.; Sirimanne, P. M.; Soga, T.; Jimbo, T., Properties of pulsed-laser-deposited CuI and characteristics of constructed dye-sensitized TiO2|Dye|CuI solid-state photovoltaic solar cells. *Japanese Journal of Applied Physics, Part 1: Regular Paper, Short Notes & Review Paper* **2003,** 42, (8), 4966-4972.

57. Kumara, G. R. A.; Kaneko, S.; Okuya, M.; Tennakone, K., Fabrication of Dye-Sensitized Solar Cells Using Triethylamine Hydrothiocyanate as a CuI Crystal Growth Inhibitor. *Langmuir* **2002,** 18, (26), 10493-10495.

58. Rusop, M.; Soga, T.; Jimbo, T.; Umeno, M., Copper iodide thin films as a p-type electrical conductivity in dye-sensitized p-CuI|Dye|n-TiO2 heterojunction solid state solar cells. *Surface Review and Letters* **2004,** 11, (6), 577-583.

59. Gao, P.; Gu, M.; Liu, X.-L.; Liu, B.; Huang, S.-M., X-ray excited luminescence of cuprous iodide single crystals: On the nature of red luminescence. *Applied Physics Letters* **2009,** 95, (22), 221904/1-221904/3.

60. Kim, D.; Nakayama, M.; Kojima, O.; Tanaka, I.; Ichida, H.; Nakanishi, T.; Nishimura, H., Thermal-strain-induced splitting of heavy- and light-hole exciton energies in CuI thin films grown by vacuum evaporation. *Physical Review B: Condensed Matter and Materials Physics* **1999,** 60, (19), 13879-13884.

61. Tanaka, I.; Kim, D.; Nakayama, M.; Nishimura, H., Photoluminescence from heavy-hole and light-hole excitons split by thermal strain in CuI thin films. *Journal of Luminescence* **2000,** 87-89, 257-259.

62. Switzer, J. A.; Gudavarthy, R. V.; Kulp, E. A.; Mu, G.; He, Z.; Wessel, A. J., Resistance Switching in Electrodeposited Magnetite Superlattices. *Journal of the American Chemical Society* **2010,** 132, (4), 1258-1260.

63. Kulp, E. A.; Kothari, H. M.; Limmer, S. J.; Yang, J.; Gudavarthy, R. V.; Bohannan, E. W.; Switzer, J. A., Electrodeposition of Epitaxial Magnetite Films and Ferrihydrite Nanoribbons on Single-Crystal Gold. *Chemistry of Materials* **2009,** 21, (21), 5022-5031.

64. Kothari, H. M.; Kulp, E. A.; Limmer, S. J.; Poizot, P.; Bohannan, E. W.; Switzer, J. A., Electrochemical deposition and characterization of Fe3O4 films produced by the reduction of Fe(III)-triethanolamine. *Journal of Materials Research* **2006,** 21, (1), 293-301.

65. Zhang, Z.; Satpathy, S., Electron states, magnetism, and the Verwey transition in magnetite. *Physical Review B: Condensed Matter* **1991,** 44, (24), 13319-31.

66. Anisimov, V. I.; Elfimov, I. S.; Hamada, N.; Terakura, K., Charge-ordered insulating state of Fe3O4 from first-principles electronic structure calculations. *Physical Review B: Condensed Matter* **1996,** 54, (7), 4387-4390.

67. Yanase, A.; Siratori, K., Band structure in the high temperature phase of iron oxide (Fe3O4). *Journal of the Physical Society of Japan* **1984,** 53, (1), 312-17.

68. Verwey, E. J. W., Electronic conduction of magnetite (Fe3O4) and its transition point at low temperatures. *Nature (London, U. K.)* **1939,** 144, 327-8.

69. Walz, F., The Verwey transition-a topical review. *Journal of Physics: Condensed Matter* **2002,** 14, (12), R285-R340.

70. Garcia, J.; Subias, G., The Verwey transition-a new perspective. *Journal of Physics: Condensed Matter* **2004,** 16, (7), R145-R178.

71. Rado, G. T.; Ferrari, J. M., Linear and bilinear magnetoelectric effects in magnetically biased magnetite (Fe3O4). *Physical Review B: Solid State* **1977,** 15, (1), 290-7.

72. Jambor, J. L.; Dutrizac, J. E., Occurrence and Constitution of Natural and Synthetic Ferrihydrite, a Widespread Iron Oxyhydroxide. *Chemical Reviews (Washington, D. C.)* **1998,** 98, (7), 2549-2585.

73. Michel, F. M.; Ehm, L.; Antao, S. M.; Lee, P. L.; Chupas, P. J.; Liu, G.; Strongin, D. R.; Schoonen, M. A. A.; Phillips, B. L.; Parise, J. B., The structure of ferrihydrite, a nanocrystalline material. *Science (Washington, DC, United States)* **2007,** 316, (5832), 1726-1729.

74. Coey, J. M. D.; Readman, P. W., New spin structure in an amorphous ferric gel. *Nature (London)* **1973,** 246, (5434), 476-8.

75. Coey, J. M. D.; Readman, P. W., Characterization and magnetic properties of natural ferric gel. *Earth and Planetary Science Letters* **1973,** 21, (1), 45-51.

76. Hiemstra, T.; Van Riemsdijk, W. H.; Rossberg, A.; Ulrich, K.-U., A surface structural model for ferrihydrite II: Adsorption of uranyl and carbonate. *Geochimica et Cosmochimica Acta* **2009,** 73, (15), 4437-4451.

77. Hiemstra, T.; Van Riemsdijk, W. H., A surface structural model for ferrihydrite I: Sites related to primary charge, molar mass, and mass density. *Geochimica et Cosmochimica Acta* **2009,** 73, (15), 4423-4436.

78. Schwertmann, U.; Friedl, J.; Stanjek, H.; Murad, E.; Bender Koch, C., Iron oxides and smectites in sediments from the Atlantis II Deep, Red Sea. *European Journal of Mineralogy* **1998,** 10, (5), 953-967.

79. Ingler, W. B., Jr.; Baltrus, J. P.; Khan, S. U. M., Photoresponse of p-Type Zinc-Doped Iron(III) Oxide Thin Films. *Journal of the American Chemical Society* **2004,** 126, (33), 10238-10239.

80. Vibha, P.; Saddichha, S.; Kumar, R., Attitudes of ward attendants towards mental illness: comparisons and predictors. *The International journal of social psychiatry* **2008,** 54, (5), 469-78.

81. Sukava, A. J.; Newby, W. J.; DiIorio, R. A.; Sharma, R. N.; Chu, K. P., Cathode growth at the air-solution interface in the electrodeposition of copper. *Nature (London, United Kingdom)* **1968,** 220, (5167), 574-6.

82. Huang, C.; Wang, P.; Guan, W.; Yang, S.; Gao, L.; Wang, L.; Song, X.; Murakami, R.-i., Improved microstructure and magnetic properties of iron-cobalt nanowire via an ac electrodeposition with a multistep voltage. *Materials Letters* **2010,** 64, (22), 2465-2467.

83. Haehnel, V.; Faehler, S.; Schaaf, P.; Miglierini, M.; Mickel, C.; Schultz, L.; Schloerb, H., Towards smooth and pure iron nanowires grown by electrodeposition in self-organized alumina membranes. *Acta Materialia* **2010,** 58, (7), 2330-2337.

84. Limmer, S. J.; Kulp, E. A.; Switzer, J. A., Epitaxial Electrodeposition of ZnO on Au(111) from Alkaline Solution: Exploiting Amphoterism in Zn(II). *Langmuir* **2006,** 22, (25), 10535-10539.

85. Liu, R.; Vertegel, A. A.; Bohannan, E. W.; Sorenson, T. A.; Switzer, J. A., Epitaxial electrodeposition of zinc oxide nanopillars on single-crystal gold. *Chemistry of Materials* **2001,** 13, (2), 508-512.

86. Boonsalee, S.; Gudavarthy, R. V.; Bohannan, E. W.; Switzer, J. A., Epitaxial Electrodeposition of Tin(II) Sulfide Nanodisks on Single-Crystal Au(100). *Chemistry of Materials* **2008,** 20, (18), 5737-5742.

87. Kulp, E. A.; Switzer, J. A., Electrochemical Biomineralization: The Deposition of Calcite with Chiral Morphologies. *Journal of the American Chemical Society* **2007,** 129, (49), 15120-15121.

88. Kothari, H. M.; Vertegel, A. A.; Bohannan, E. W.; Switzer, J. A., Epitaxial Electrodeposition of Pb-Tl-O Superlattices on Single-Crystal Au(100). *Chemistry of Materials* **2002,** 14, (6), 2750-2756.

89. Switzer, J. A.; Hung, C.-J.; Huang, L.-Y.; Switzer, E. R.; Kammler, D. R.; Golden, T. D.; Bohannan, E. W., Electrochemical Self-Assembly of Copper/Cuprous Oxide Layered Nanostructures. *Journal of the American Chemical Society* **1998,** 120, (14), 3530-3531.

90. Switzer, J. A.; Kothari, H. M.; Bohannan, E. W., Thermodynamic to Kinetic Transition in Epitaxial Electrodeposition. *Journal of Physical Chemistry B* **2002,** 106, (16), 4027-4031.

91. Bohannan, E. W.; Jaynes, C. C.; Shumsky, M. G.; Barton, J. K.; Switzer, J. A., Low-temperature electrodeposition of the high-temperature cubic polymorph of bismuth(III) oxide. *Solid State Ionics* **2000,** 131, (1,2), 97-107.

92. Nakada, T., Preparation of cadmium sulfide thin films by chemical bath deposition and its application to copper indium selenide (CuInSe2) solar cells. *Oyo Butsuri* **1993,** 62, (2), 139-42.

93. Lin, L.-H.; Wu, C.-C.; Lai, C.-H.; Lee, T.-C., Controlled Deposition of Silver Indium Sulfide Ternary Semiconductor Thin Films by Chemical Bath Deposition. *Chemistry of Materials* **2008,** 20, (13), 4475-4483.

94. Desai, J. D.; Lokhande, C. D., Alkaline bath chemical deposition of antimony (III) sulfide thin films. *Thin Solid Films* **1994,** 237, (1-2), 29-31.

95. Najdoski, M. Z.; Grozdanov, I. S.; Dey, S. w. K.; Siracevska, B. B., Chemical bath deposition of mercury(II) sulfide thin layers. *Journal of Materials Chemistry* **1998,** 8, (10), 2213-2215.

96. Desai, J. D.; Lokhande, C. D., Chemical deposition of semiconducting bismuth(III) sulfide thin films from an acidic bath. *Indian Journal of Pure and Applied Physics* **1993,** 31, (3), 152-5.

97. Gadave, K. M.; Lokhande, C. D., Formation of copper sulfide (CuxS) films through a chemical bath deposition process. *Thin Solid Films* **1993,** 229, (1), 1-4.

98. Bhad, V. V.; Lokhande, C. D., Formation of tin sulfide (SnS2) thin films by chemical bath deposition. *Bulletin of Electrochemistry* **1991,** 7, (12), 571-2.

99. Smu, I.; Nnabuchi, M. N., The optical and solid state properties of lead selenide (PbSe) thin films grown by chemical bath deposition (CBD) technique. *Journal of Ovonic Research* **2010,** 6, (2), 81-86.

100. Hankare, P. P.; Chate, P. A.; Sathe, D. J.; Chavan, P. A.; Bhuse, V. M., Effect of thermal annealing on properties of zinc selenide thin films deposited by chemical bath deposition. *Journal of Materials Science: Materials in Electronics* **2009,** 20, (4), 374-379.

101. Levy-Clement, C.; Neumann-Spallart, M.; Haram, S. K.; Santhanam, K. S. V., Chemical bath deposition of cubic copper(I) selenide and its room temperature transformation to the orthorhombic phase. *Thin Solid Films* **1997,** 302, (1,2), 12-16.

102. Garcia, V. M.; Nair, P. K.; Nair, M. T. S., Copper selenide thin films by chemical bath deposition. *Journal of Crystal Growth* **1999,** 203, (1/2), 113-124.

103. Al, M.; Islam, A. B. M. O.; Bhuiyan, A. H., Structural, electrical and optical properties of copper selenide thin films deposited by chemical bath deposition technique. *Journal of Materials Science: Materials in Electronics* **2005,** 16, (5), 263-268.

104. Shyju, T. S.; Anandhi, S.; Indirajith, R.; Gopalakrishnan, R., Effects of annealing on cadmium selenide nanocrystalline thin films prepared by chemical bath deposition. *Journal of Alloys and Compounds* **2010,** 506, (2), 892-897.

105. Girija, K.; Thirumalairajan, S.; Mohan, S. M., Deposition and characterization of cadmium indium selenide thin films by chemical bath technique. *Optoelectronics and Advanced Materials, Rapid Communications* **2009,** 3, (1), 53-55.

106. Pan, Q.; Wang, M.; Wang, Z., Facile fabrication of Cu2O/CuO nanocomposite films for lithium-ion batteries via chemical bath deposition. *Electrochemical and Solid-State Letters* **2009,** 12, (3), A50-A53.

107. Shokuhfar, A.; Hassanjani-Roshan, A.; Vaezi, M. R.; Kazemzadeh, S. M.; Kandjani, A. E.; Nasiri-Tabrizi, B., Synthesis and characterization of TiO2 nanoparticles via Chemical Bath Deposition (CBD) method. *Journal of Nano Research* **2010,** 11, 35-38.

108. Peterson, R. B.; Fields, C. L.; Gregg, B. A., Epitaxial Chemical Deposition of ZnO Nanocolumns from NaOH Solutions. *Langmuir* **2004,** 20, (12), 5114-5118.

109. Maji, S.; Bhattacharyya, P.; Sengupta, A.; Saha, H., Growth and characterization of nano-cups, flowers and nanorods of ZnO by chemical bath deposition. *Advanced Science Letters* **2010,** 3, (2), 154-160.

110. Lin, M.-S.; Chen, C.-C.; Wang, W.-C.; Lin, C.-F.; Chang, S.-Y., Fabrication of the selective-growth ZnO nanorods with a hole-array pattern on a p-type GaN:Mg layer through a chemical bath deposition process. *Thin Solid Films* **2010,** 518, (24), 7398-7402.

111. Jacobs, K.; Balitsky, D.; Armand, P.; Papet, P., Low-temperature chemical bath deposition of crystalline ZnO. *Solid State Sciences* **2010,** 12, (3), 333-338.

112. Berkat, L.; Cattin, L.; Reguig, A.; Regragui, M.; Bernede, J. C., Comparison of the physico-chemical properties of NiO thin films deposited by chemical bath deposition and by spray pyrolysis. *Materials Chemistry and Physics* **2005,** 89, (1), 11-20.

113. Wang, R.; Liu, C.; Zeng, J.; Li, K.; Wang, H., Fabrication and morphology control of BaWO4 thin films by microwave assisted chemical bath deposition. *Journal of Solid State Chemistry* **2009,** 182, (4), 677-684.

114. Lakshmi, M.; Bindu, K.; Bini, S.; Vijayakumar, K. P.; Kartha, C. S.; Abe, T.; Kashiwaba, Y., Chemical bath deposition of different phases of copper selenide thin films by controlling bath parameters. *Thin Solid Films* **2000,** 370, (1,2), 89-95.

PAPER

I. Tilted Epitaxial ZnO Nanospears on Si(001) by Chemical Bath Deposition

*Guojun Mu, Rakesh V. Gudavarthy, Elizabeth A. Kulp, and Jay A. Switzer**

Department of Chemistry and Graduate Center for Materials Research, Missouri University of Science and Technology, Rolla, MO 65409-1170

*To whom correspondence should be addressed: E-mail: *jswitzer@mst.edu*.

ABSTRACT

We show that epitaxial ZnO nanospears can be deposited onto degenerate p-type Si(001) from an alkaline supersaturated solution of Zn(II) at 70 ^{o}C using chemical bath deposition. The lattice mismatch between the hexagonal ZnO and diamond cubic Si is reduced from -40.16% for an un-tilted structure to -0.25% in the $ZnO[1\bar{2}10]$ direction and -0.99% in $ZnO[25\bar{7}\bar{6}]$ direction by tilting the nanospears 51^{o} relative to the surface normal. The tilted nanostructure brings the $(20\bar{2}3)$ planes of ZnO into coincidence with the (001) planes of Si.

KEYWORDS ZnO, Si(001), epitaxy, chemical bath deposition

INTRODUCTION

Zinc oxide (space group = $P6_3mc$; a = 0.32495 nm, c = 0.52069 nm) is an n-type semiconductor with a direct band gap of 3.4 eV and an exciton binding energy of 60 meV

at room temperature.[1] Recently, there has been intense interest in one dimensional nanostructures of ZnOfor application in photoelectric semiconductor devices, including light-emitting diodes,[2-6] laser diodes,[7-11] photoelectrochemical solar cells,[12-15] and solid state solar cells.[16-23] Typically, p-n homojunctions are produced in such semiconductor devices. Creation of homojunctions with p-type and n-type ZnO is difficult, however, because native donors in ZnO are known to compensate for holes.[2] Heterojunctions are a viable alternative, which can be fabricated using ZnO and another semiconducting material with a different bandgap (either n-type or p-type), such as Cu_2O,[16-19] GaN,[3,7,24,25] Si,[4,5,8,20-23,26] or SiC.[9,27,28]

Although the epitaxial deposition of ZnO has been reported on many single crystal substrates, such as Au,[29,30] GaN,[31] InP,[32-34] $MgAl_2O_4$,[35] and sapphire,[10] the deposition on Si typically requires buffer layers. The large difference in the thermal expansion coefficients of the two materials[26] and the high reactivity of Si is problematic for producing ZnO/Si epitaxial heterojunctions by conventional thermal processing. The ZnO/Si epitaxial system is interesting because of the fundamental information it may provide about heteroepitaxy in large mismatch systems, and because of the possibility of producing efficient devices such as photovoltaic or photoelectrochemical solar cells. The heteroepitaxial system is relevant for solar cells, because higher efficiencies are possible with cells made with multiple bandgaps because they utilize a larger portion of the solar spectrum. Electron-hole recombination or carrier scattering at grain boundaries should be minimized in the epitaxial system. Also, the high aspect ratio of ZnO should maximize collection of charge carriers. Recently, the fabrication of high-aspect-ratio (length/diameter) semiconductors (Si, GaAs, CdSe) for photoelectrochemical and

photovoltaic devices has attracted much attention compared with the conventional planar geometry.[36-39] The Lewis group has theoretically and experimentally shown that nanorod semiconductor arrays arranged perpendicular to the substrate enhance the overall efficiency.[36]

Recently, our group has exploited the amphoteric nature of ZnO to electrodeposit epitaxial ZnO layers on single crystal Au(111) from alkaline solution.[30] The alkaline solution used for the deposition (pH: 10-14) may be advantageous for growing epitaxial films on Si, because in strong base the amorphous passivating layer of SiO_2 on Si dissolves. One difficulty, however, is that the electrochemical oxidation reactions used to lower the local pH at the working electrode may also lead to Si dissolution. This effect may be minimized using chemical bath deposition.

Peterson et al. reported the chemical bath deposition of highly-ordered ZnO(0001) films on ZnO pre-coated glasses from a supersaturated solution containing $Zn(NO_3)_2$ and NaOH.[40] Adeen et al. reported lateral overgrowth of epitaxial ZnO on $MgAl_2O_4$(111) substrates from $Zn(NO_3)_2$ and ammonia solution at 90^oC.[41] Here, we demonstrate that epitaxial ZnO onto Si(001) can be grown by chemical bath deposition from an alkaline supersaturated solution of Zn(II). Epitaxial growth on Si is achieved in aqueous solution in spite of the high reactivity of the Si surface, the large lattice mismatch, and the propensity of Si to form an amorphous SiO_2 interfacial layer.

EXPERIMENTAL SECTION

Film Deposition. The films were deposited onto degenerate p-type Si(001) wafers supplied by Virginia Semiconductor that were doped with boron to a resistivity of

3.5 mΩ-cm. The wafers were degreased in acetone and ethanol, then rinsed with deionized (DI) water (18 MΩ-cm) obtained from a Milli-Q water purification system. The wafers were etched before deposition to produce an H-terminated surface. The etch consisted of 5% HF for 1 minute, hot DI water for 15 minute, and 5% HF for 10 seconds, followed by a thorough rinsing with DI water. The wafer was then placed vertically in 180 mL of DI water stirred and maintained at 70 ^{o}C. Immediately after immersing the wafer, 20 mL of a concentrated solution containing 2.5 M NaOH and 60 mM $Zn(NO_3)_2 \cdot 6H_2O$ was added, producing an alkaline final solution with slightly supersaturated zincate: 0.25 M of NaOH and 6 mM of Zn(II). ZnO was grown on the substrate for 15 minutes, accompanied by global precipitation in the solution. The silicon wafer was removed, rinsed thoroughly with DI water and air dried.

Characterization. The microstructure of the ZnO was observed with a Hitachi S-4700 field-emission scanning electron microscope. The tilt angle of the ZnO nanospears and the epitaxial relationship between the ZnO and Si were both determined by X-ray pole figure analysis. The pole figures were acquired using a high resolution four-circle diffractometer (Philips X′Pert MRD) with Cu $K_{\alpha 1}$ source radiation. Pole figures were collected in the point-focus mode using a crossed-slit collimator as the primary optics and a flat graphite monochromator as the secondary optics. A model of the interface between ZnO and Si was generated using Molecular Simulations software (Cerius, Version 2). The photoluminescence (PL) spectrum was acquired at room temperature in a backscattering geometry using a Coherent Innova 90C Ar^+ ion laser (λ = 355 nm) with a total power of 150 mW focused into a 20 μm diameter beam as the excitation source.

RESULTS AND DISCUSSION

The key factor of the ZnO deposition is to slightly exceed the saturation state of the solution. The solubility and speciation distribution of ZnO in aqueous solution versus pH (Figure 1) was calculated using the thermodynamic data and equations shown by Lincot and co-workers.[42,43] When the base concentration is chosen to be 0.25 M and the temperature is fixed at 70°C, the maximum solubility of ZnO is 4.0 mM. The soluble species are $Zn(OH)_3^-$ (31.6%) and $Zn(OH)_4^{2-}$ (68.4%). To slightly exceed saturation, 6.0 mM of $Zn(NO_3)_2$ was added, with the state of the solution represented by an asterisk in Figure 1. The deposition mechanism is assumed to be the same as that proposed by Peterson et al.[40] In addition, there may be a decrease in pH at the Si/solution interface due to Si dissolution, which would lower the solubility of Zn(II) (see Equations 1-3).

$$Si + 4H_2O \rightarrow H_2SiO_4^{2-} + 2H^+ + 2H_2 \uparrow \quad (1)$$

$$Zn(OH)_4^{2-} + 2H^+ \rightarrow ZnO + 3H_2O \quad (2)$$

$$Zn(OH)_4^{2-} + Si + H_2O \rightarrow ZnO + H_2SiO_4^{2-} + 2H_2 \uparrow \quad (3)$$

An SEM image of the ZnO is shown in Figure 2. The ZnO grows with a nanospear morphology, with spears that are 100-200 nm in diameter and about 1 micrometer in length. The nanospears grow along the ZnO[0001] direction (c-axis), but they are tilted with respect to the normal of the substrate surface. Also, from the micrograph it appears that there are four orthogonal in-plane orientations. The spear-like morphology is probably due to the hindering effect of OH^- ions as reported by Li et al.[44] They report that the growth velocities (V) of ZnO along different directions in alkaline solutions are in the order: $V_{<0001>} > V_{<01\bar{1}\bar{1}>} > V_{<01\bar{1}0>} > V_{<01\bar{1}1>} > V_{<000\bar{1}>}$.[44] As a result, the

$\{01\bar{1}1\}$ pyramidal facets that grow more slowly remain, while the rapidly growing (0001) facets disappear.

The X-ray θ-2θ scan in Figure 3 only shows Si (002) and (004) peaks, indicating a Si(001) out-of-pane orientation, on peaks from ZnO are observed. There might be two reasons: the ZnO deposited is amorphous, or the tilting of ZnO nanospears brings up an out-of-plane orientation which is of low intensity or even forbidden in X-ray diffraction.

Therefore, the actual tilt angle of the ZnO nanospears and the epitaxial relationship between the ZnO and Si were both determined by X-ray pole figure analysis. Pole figures are run by choosing a diffraction angle (2θ) for a plane that is not parallel with the surface of the material. The tilt of the sample (χ) is then incrementally varied, with the azimuthal angle (φ) varied from 0 to 360^o at each value of χ. Peaks occur in the pole figure when the Bragg condition is satisfied. The peaks show that there is both out-of-plane and in-plane order. Polycrystalline films would produce featureless pole figures, whereas films with a fiber texture (i.e., ordered out-of-plane, but random in-plane) would show rings in the pole figure.

As shown in Figure 4, three ZnO pole figures and one Si pole figure were performed. The (0001) pole figure of the ZnO (2θ = 34.45^o) in Figure 4a is quite simple, exhibiting four equally spaced ($\Delta\varphi = 90^o$) spots at $\chi = 51^o$. This χ corresponds to the angle between the ZnO (0001) planes and the planes parallel with the surface. This is a direct measure of the tilt angle of 51^o of the nanospears. Since more than one set of planes in ZnO is 51^o apart from the (0001) planes, one pole figure is not sufficient to determine the out-of-plane orientation of ZnO. The $(10\bar{1}0)$ and $(10\bar{1}1)$ pole figures were thereby acquired as complements. The $(10\bar{1}0)$ pole figure (2θ = 31.80^o) in Figure 4b

presents four equally spaced spots at $\chi = 38^o$ and eight spots at $\chi = 67^o$. The $(10\bar{1}1)$ pole figure ($2\theta = 36.28^o$) in Figure 4c shows four spots at $\chi = 9^o$ and 66^o, and eight spots at $\chi = 50^o$ and 87^o. Each pole figure is consistent with a $(20\bar{2}3)$ out-of-pane orientation of ZnO with four crystalline domains rotated by 90^o from one another.

To verify the orientations determined from the pole figures, the ZnO $(20\bar{2}3)$ stereographic projections were constructed using CaRIne Crystallography software (Version 3.1), probing the ZnO(0001), $(10\bar{1}0)$, and $(10\bar{1}1)$ type reflections, as shown in Figure 5a, 5b, and 5c respectively. Similar to the pole figures, the radial direction is the tilt angle (χ), and the azimuthal angle (φ) is the rotation about its axis. In Figure 5a, one spot at $\chi = 50.9^o$ is assigned to the {0001} type reflection of the $(20\bar{2}3)$ orientation. In Figure 5b, one spot at $\chi = 38.4^o$ and two spots at $\chi = 66.9^o$ correspond to one set of the $\{10\bar{1}0\}$ type reflections of the $(20\bar{2}3)$ orientation. And in Figure 5c, one spot at $\chi = 10.0^o$, two spots at $\chi = 50.2^o$, one spot at $\chi = 66.8^o$, and two spots at $\chi = 87.2^o$ correspond to one set of the $\{10\bar{1}1\}$ type reflections of the $(20\bar{2}3)$ orientation. Figures 5a, 5b, and 5c assume only one domain of each reflection.

Si has the diamond cubic structure (space group = *Fd3m*; a = 0.54305 nm). Because the Si(001) substrate has four-fold symmetry, it is reasonable to expect four domains of the ZnO crystal to deposit on the surface. Rotating each stereographic projection by 0^o, 90^o, 180^o, and 270^o, then overlaying the four rotated images result in the stereographic projections shown in Figure 5a' 5b' and 5c'. These stereographic projections match the observed pole figures in Figure 4a, 4b, and 4c, respectively. Therefore, the ZnO deposited with the $(20\bar{2}3)$ planes parallel with the Si(001) planes.

The overall epitaxial relationships of ZnO on Si were determined by comparing the ZnO pole figures and stereographic projections with those of Si substrate. The (111) substrate pole figure of Si is shown in Figure 4d, where the four equally spaced peaks at χ = 54º correspond to the angle between (111) and (001) planes in the cubic system. The epitaxial relationships of ZnO and Si were determined to be: $ZnO(20\bar{2}3)[1\bar{2}10]//Si(001)[100]$, $ZnO(20\bar{2}3)[1\bar{2}10]//Si(001)[\bar{1}00]$, $ZnO(20\bar{2}3)[1\bar{2}10]//Si(001)[010]$, and $ZnO(20\bar{2}3)[1\bar{2}10]//Si(001)[100]$. That is the ZnO$(20\bar{2}3)$ planes and Si(001) planes are parallel and the ZnO $[1\bar{2}10]$ and Si <010> in-plane directions are coincident. A cartoon showing the four equivalent in-plane orientations is shown in Figure 6.

A model of the interface (Figure 6) between ZnO and Si was generated based on the measured epitaxial relationships. The larger gray balls represent Si atoms on the Si(001) surface, and the smaller red balls represent O atoms in the ZnO$(20\bar{2}3)$ plane. As mentioned above, ZnO and Si have different crystal structures (one hexagonal wurtzite structure, the other fcc diamond), and the lattice parameter mismatch is large (a = 0.32495 nm, c = 0.52069 nm for ZnO; a = 0.54305 nm for Si). The in-plane lattice mismatch for ZnO aligned with the c-axis perpendicular to the Si surface is -40.16%. The mismatch is dramatically lowered by the observed tilted nanostructure in which the ZnO$(20\bar{2}3)$ on Si(001) planes are brought into coincidence. An interface model is shown in Figure 7. The lattice mismatch for four Si atoms and six O atoms in the $ZnO[1\bar{2}10]$ direction, or the Si[010] direction equivalently, is -0.25%. At an angle of 59^o from the $ZnO[25\bar{\bar{7}}6]$ direction, or the Si[530] direction, the lattice mismatch is -0.99%. We note

that although this orientation seems unusual, it has been observed previously that ZnO grows with a $(20\bar{2}3)$ orientation on $CeO_2(001)$.[45]

The photoluminescence (PL) spectrum is shown in Figure 8. The UV emission at 364 nm (3.41 eV) is assigned to be ZnO exciton emission. A much stronger visible emission at 500-700 nm is attributed to multiple sources, mainly the singly ionized O vacancies and/or the Zn interstitials in the ZnO crystal. [46,47] It has been reported by K. S. Ahn et al. that the ZnO nanorods, deposited onto FTO glass by sputtering in a mixed Ar/N_2 atmosphere, showed photoelectrochemical currents under the illumination of green light.[13] This observation shows the potential application of the ZnO with defects for utilization of the visible portion of solar illumination.

CONCLUSIONS

In this article, we have shown that epitaxial ZnO can be grown directly onto Si(001) by chemical bath deposition from an alkaline supersaturated solution of Zn(II) at 70 ^{o}C. The epitaxial relationships between the tilted ZnO nanospears and the Si substrate have been determined using the X-ray pole figure technique. The lattice mismatch is reduced from -40.16% to -0.25% in the $ZnO[1\bar{2}10]$ in-plane direction and -0.99% in $ZnO[25\bar{7}\bar{6}]$ in-plane direction by tilting the nanospears 51^{o} relative to the surface normal. The ZnO/Si heterojunction leads the way to integration of a large bandgap oxide semiconductor with traditional semiconductor devices. It also may produce efficient photoelectrochemical and photovoltaic solar cells. The two-bandgap cells would use a larger portion of the solar spectrum compared with single-bandgap cells. In addition, the single-crystal nanowire architecture and epitaxial interface should minimize electron-hole

recombination. An important next step in characterizing these ZnO/Si heterojunctions will be to determine the interfacial energetics. For this work it will be ideal to produce junctions with n, n^+, p, and p^+ silicon. A challenge will be to make ohmic contacts to the ZnO nanospears without contacting the Si.

ACKNOWLEDGMENTS

This work is supported by DOE Grant DE-FG02-08ER46518. The authors also thank Dr. Suchi Guha, Dr. Ping Yu, and Keshab R. Paudel from the University of Missouri Columbia for assisting with the PL measurements.

REFERENCES

[1] Ozgur, U.; Alivov, Y. I.; Liu, C.; Teke, A.; Reshchikov, M. A.; Dogan, S.; Avrutin, V.; Cho, S. J.; Morkoc, H. *J. Appl. Phys.* **2005**, *98*, 041301/1.

[2] Kong, J.; Chu, S.; Olmedo, M.; Li, L.; Yang, Z.; Liu, *J. Appl. Phys. Lett*. **2008**, *93*, 132113/1.

[3] Bayram, C.; Teherani, F. Hosseini; Rogers, D. J.; Razeghi, M. *Appl. Phys. Lett*. **2008**, *93*, 081111/1.

[4] Harako, S.; Yokoyama, S.; Ide, K.; Zhao, X.; Komoro, S. *Phys. Status Solidi A* **2008**, *205*, 19.

[5] Bao, J.; Zimmler M. A.; Capasso, F.; Wang, X.; Ren, Z. F. *Nano Lett*. **2006**, *6*, 1719.

[6] Konenkamp, R.; Word, R. C.; Godinez, M. *Nano Lett*. **2005**, *5*, 2005.

[7] Leong, E. S.; Yu, S. F.; Lau, S. P. *Appl. Phys. Lett*. **2006**, *89*, 221109/1.

[8] Chu, S.; Olmedo, M.; Yang, Z.; Kong, J.; Liu, J. *Appl. Phys. Lett*. **2008**, *93*, 181106/1.

[9] Leong, E. S.; Yu, S. F. *Adv. Mater*. **2006,** *18*, 1685.

[10] Huang M. H.; Mao S.; Feick H.; Yan H.; Wu Y.; Kind H.; Weber E.; Russo R.; Yang P. *Science* **2001**, *292*, 1897.

[11] Tang, Z. K.; Wong, G. K. L.; Yu, P.; Kawasaki, M.; Ohtomo, A.; Koinuma, H.; Segawa, Y. *Appl. Phys. Lett*. **1998**, *72*, 3270.

[12] Martinson, A. B.; Goes, M. S.; Fabregat-Santiago, F.; Bisquert, J.; Pellin, M. J.; Hupp, J. T. *J. Phys. Chem*. **2009**, ASAP.

[13] Ahn, K. S.; Shet, S.; Deutsch, T.; Jiang, C. S.; Yan, Y.; Al-Jassim, M.; Turner, J. *J. Power Sources* **2008**, *176*, 387.

[14] Martinson, A. B.; Elam, J. W.; Hupp, J. T.; Pellin, M. J. *Nano Lett*. **2007**, *7*, 2183.

[15] Nonomura, K.; Komatsu, D.; Yoshida, T.; Minoura, H.; Schlettwein, D. *Phys. Chem. Chem. Phys*. **2007**, *9*, 1843.

[16] Yuhas, B. D.; Yang, P. *J. Am. Chem. Soc*. **2009**, *131*, 3756.

[17] Jeong, S. S.; Mittiga, A.; Salza, E.; Masci, A.; Passerini, S. *Electrochim. Acta* **2008**, *53*, 2226.

[18] Izaki, M.; Mizuno, K. T.; Shinagawa, T.; Inaba, M.; Tasaka, A. *J. Electrochem. Soc.* **2006**, *153*, C668.

[19] Minami, T.; Miyata, T.; Ihara, K.; Minamino, Y.; Tsukada, S. *Thin Solid Films* **2005**, *494*, 47.

[20] Mridha, S.; Dutta, M.; Basak, D. *J. Mater. Sci.: Mater. Electron.* **2009**, *20*, 376.

[21] Ajimsha, R. S.; Jayaraj, M. K.; Kukreja, L. M. *J. Electron. Mater.* **2008**, *37*, 770.

[22] Einsele, F.; Rostan, P. J.; Schubert, M. B.; Rau, U. *J. Appl. Phys.* **2007**, *102*, 094507/1.

[23] Wenas, W. W.; Riyadi, S. *Sol. Energy Mater. Sol. Cells* **2006**, *90*, 3261.

[24] Hsueh, K. P.; Huang, S. C.; Li, C. T.; Hsin, Y. M.; Sheu, J. K.; Lai, W. C.; Tun, C. *J. Appl. Phys. Lett.* **2007**, *90*, 132111/1.

[25] Kaminska, E.; Piotrowska, A.; Golaszewska, K.; Kruszka, R.; Kuchuk, A.; Szade, J.; Winiarski, A.; Jasinski, J.; Liliental-Weber, Z. *J. Alloys Compd.* **2004**, *371*, 129.

[26] Lo, K. Y.; Lo, S. C.; Yu, C. F.; Tite, T.; Huang, J. Y.; Huang, Y. J.; Chang, R. C.; Chu, S. Y. *Appl. Phys. Lett.* **2008**, *92*, 091909/1.

[27] El-Shaer, A.; Bakin, A.; Schlenker, E.; Mofor, A. C.; Wagner, G.; Reshanov, S. A.; Waag, A. *Superlattices Microstruct.* **2007**, *42*, 387.

[28] Alivov, Y. I.; Johnstone, D.; Ozgur, U.; Avrutin, V.; Fan, Q.; Akarca-Biyikli, S. S.; Morkoc, H. *Jpn. J. Appl. Phys., Part 1* **2005**, *44*, 7281.

[29] Liu, R.; Vertegel, A. A.; Bohannan, E. W.; Sorenson, T. A.; Switzer, J. A. *Chem. Mater.* **2001**, *13*, 508.

[30] Limmer, S. J.; Kulp, E. A.; Switzer, J. A. *Langmuir* **2006**, *22*, 10535.

[31] Lin, C. W.; Ke, D. J.; Chao, Y. C.; Chang, L.; Liang, M. H.; Ho, Y. T. *J. Cryst. Growth* **2007**, *298*, 472.

[32] Kim, T. W.; Yoon, Y. S. *J. Cryst. Growth* **2000**, *212*, 411.

[33] Keckes, J.; Ortner, B.; Cerven, I.; Jakabovic, J.; Kovac, J. *J. Appl. Phys.* **1996**, *80*, 6204.

[34] Kim, T. W.; Kwack, K. D.; Kim, H. K.; Yoon, Y. S.; Bahang, J. H.; Park, H. L. *Solid State Commun.* **2003**, *127*, 635.

[35] Andeen, D.; Loeffler, L.; Padture, N.; Lange, F. F. *J. Cryst. Growth* **2003**, *259*, 103.

[36] Kayes, B. M.; Atwater, H. A.; Lewis, N. S. *J. Appl. Phys.* **2005**, *97*, 114302/1.

[37] Green, M. A.; Wenham, S. R. *Appl. Phys. Lett.* **1994**, *65*, 2907.

[38] Tian, B; Zheng, X.; Kempa, T. J.; Fang, T.; Yu, N.; Yu, G; Huang, J; Lieber, C. M. *Nature* **2007**, *449*, 885.

[39] Tsakalakos, L.; Balch, J.; Fronheiser, J.; Korevaar, B. A; Sulima, O.; Rand, J. *Appl. Phys. Lett.* **2007**, *91*, 233117/1.

[40] Peterson, R. B.; Fields, C. L.; Gregg, B. A. *Langmuir* **2004**, *20*, 5114.

[41] Andeen, D.; Kim, J. H.; Lange, F. F.; Goh, G. K. L.; Tripathy, S. *Adv. Funct. Mater.* **2006**, *16*, 799.

[42] Goux, A.; Pauporte, T.; Chivot, J.; Lincot, D. *Electrochim. Acta* **2005**, *50*, 2239.

[43] Hubert, C.; Naghavi, N.; Canava, B.; Etcheberry, A.; Lincot, D. *Thin Solid Films* **2007**, *515*, 6032.

[44] Li, W. J.; Shi, E. W.; Zhong, W. Z.; Yin, Z. W. *J. Cryst. Growth* **1999**, *203*, 186.

[45] Duclère, J.-R.; Doggert, B; Henry, M. O.; McGlynn, E.; Kumar R. T. R.; Mosnier, J.-P. *J. Appl. Phys.* **2007**, *101*, 013509/1

[46] Kim, Y.; Seshadri, R. *Inorg. Chem.* **2008**, *47*, 8437.

[47] Roy, V. A. L.; Djurisic, A. B.; Chan, W. K.; Gao, J.; Lui, H. F.; Surya, C. *Appl. Phys. Lett.* **2003**, *83*, 141.

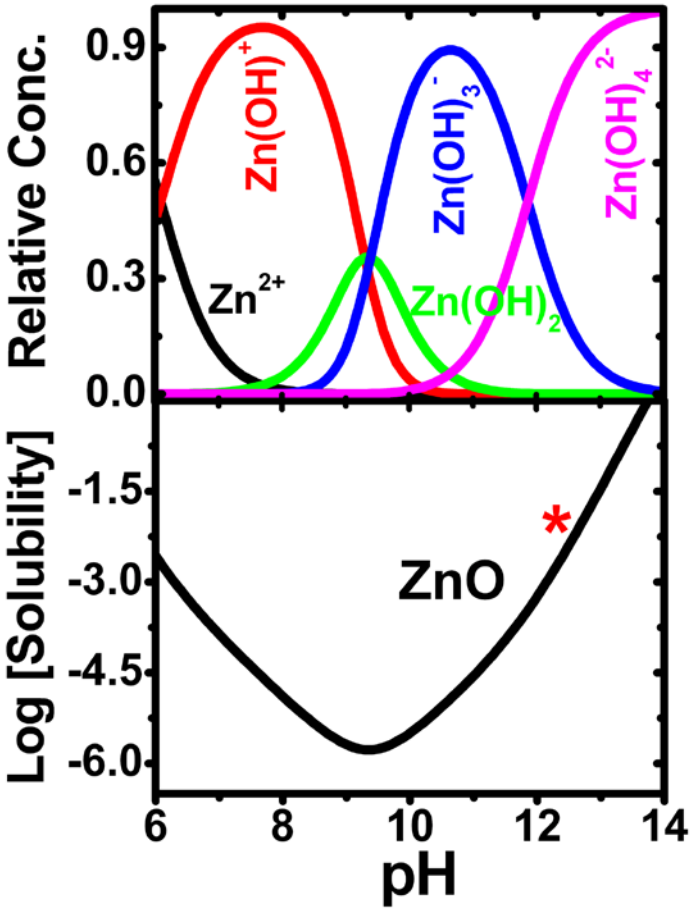

Figure 1. Speciation distribution (upper) and solubility (lower) of Zn(II) versus pH in aqueous solution at 70 ^{o}C. The asterisk represents the slightly supersaturated state of the deposition solution containing 6.0 mM of $Zn(NO_3)_2$ and 0.25 M NaOH.

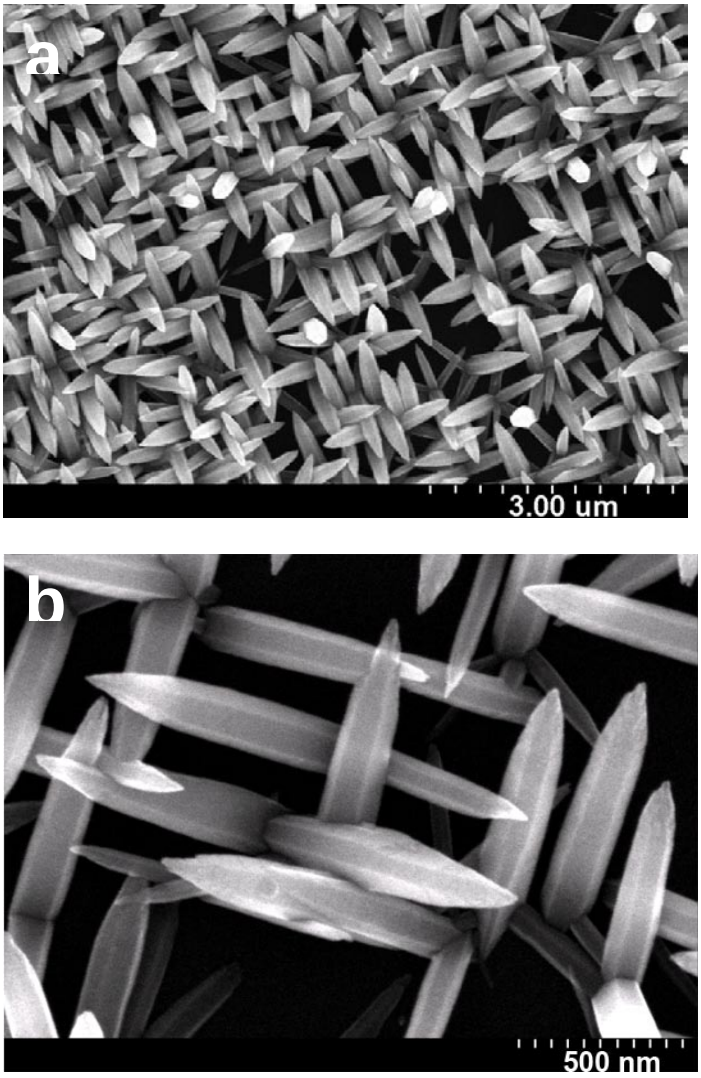

Figure 2. SEM images of as-deposited ZnO on the Si(001) substrate. (a) low- (bar marker = 3 um), and (b) high-magnification (bar marker = 500 nm) images.

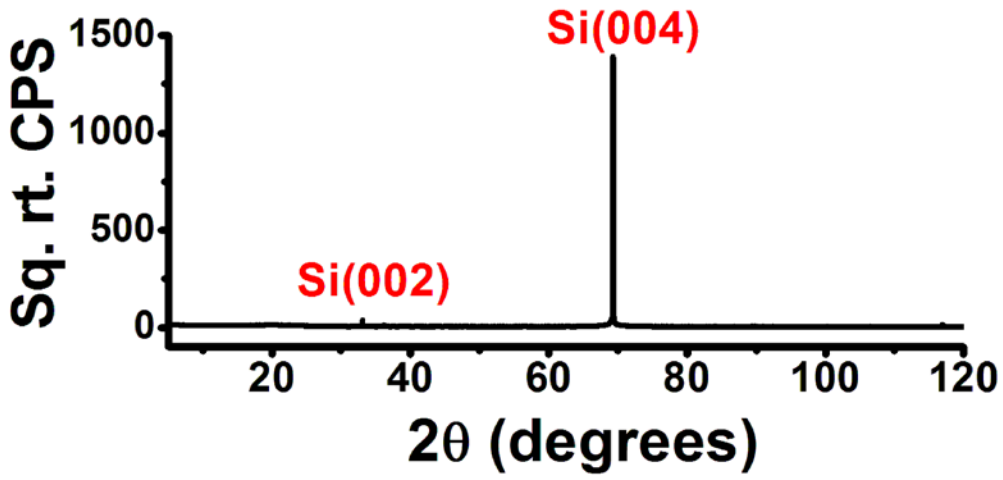

Figure 3. Symetric X-ray diffraction pattern on the as-deposited ZnO on the Si(001) substrate.

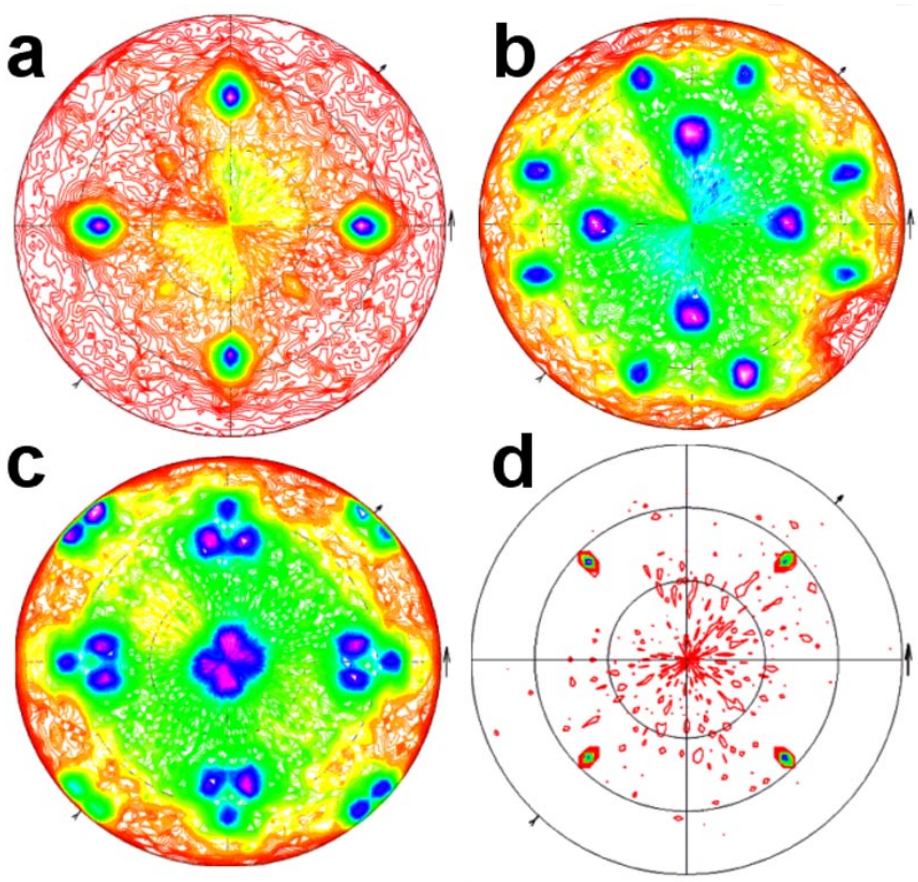

Figure 4. (a) (0001), (b)$(10\bar{1}0)$, and (c) $(10\bar{1}1)$ pole figures for ZnO and (d) (111) pole figure for the Si(001) substrate. The radial grid lines on each pole figure correspond to 30o increments in χ.

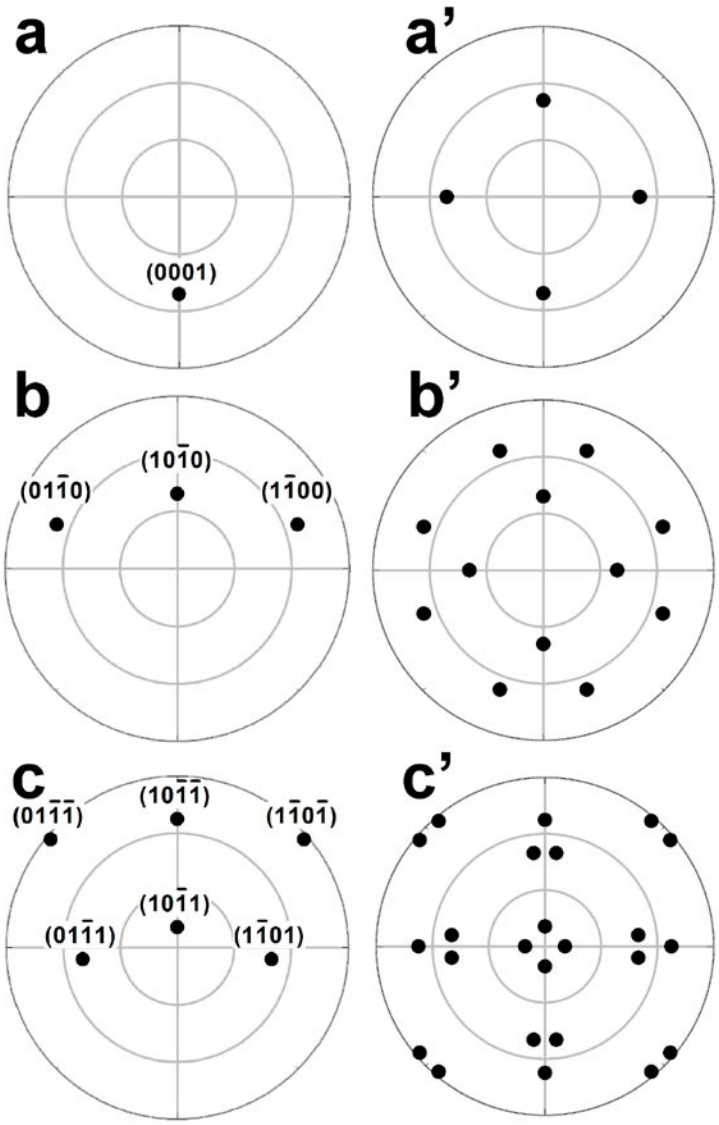

Figure 5. $(20\bar{2}3)$ stereographic projections of ZnO probing the (a) (0001), (b) $(10\bar{1}0)$, and (c) $(10\bar{1}1)$ type reflections. These projections assume only one domain of each reflection. Because Si(001) has four-fold symmetry, four domains of the ZnO are expected. Rotating a, b, and c by 0^o, 90^o, 180^o, and 270^o, and then overlaying the four rotating images results in the stereographic projection shown in a', b', and c', which agrees with the experimentally observed pole figures in Figures 3a-c, respectively. The radial grid lines on each stereographic projection correspond to 30^o increments in χ.

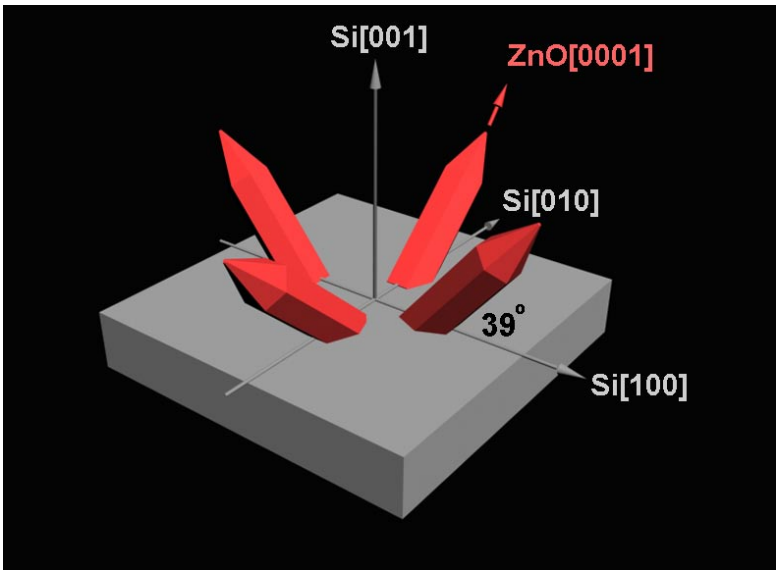

Figure 6. Schematic of the epitaxial ZnO$(20\bar{2}3)$ nanospears on Si(001) substrate. The red spears on the top represent ZnO, whereas the grey base represents Si.

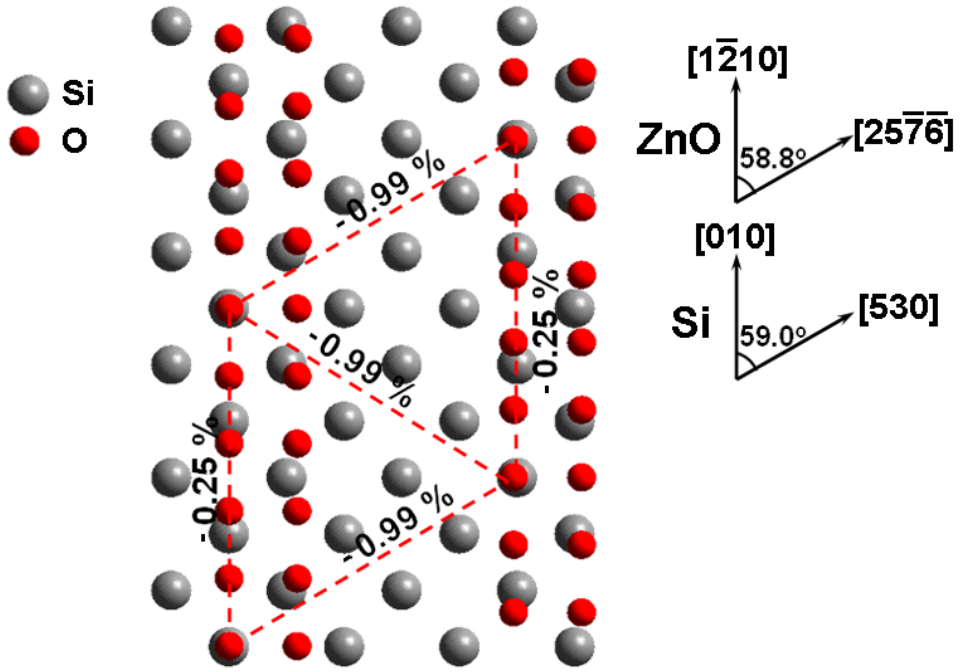

Figure 7. Interface model for the ZnO$(20\bar{2}3)$ on Si(001) planes. The Si atoms are gray, and the O atoms are red. Based on this model, the lattice mismatch is reduced from -40.16% to -0.25% in the ZnO $[1\bar{2}10]$ in-plane direction and -0.99% in ZnO $[25\bar{7}\bar{6}]$ in-plane direction by tilting the nanospears 51^{o} relative to the surface normal.

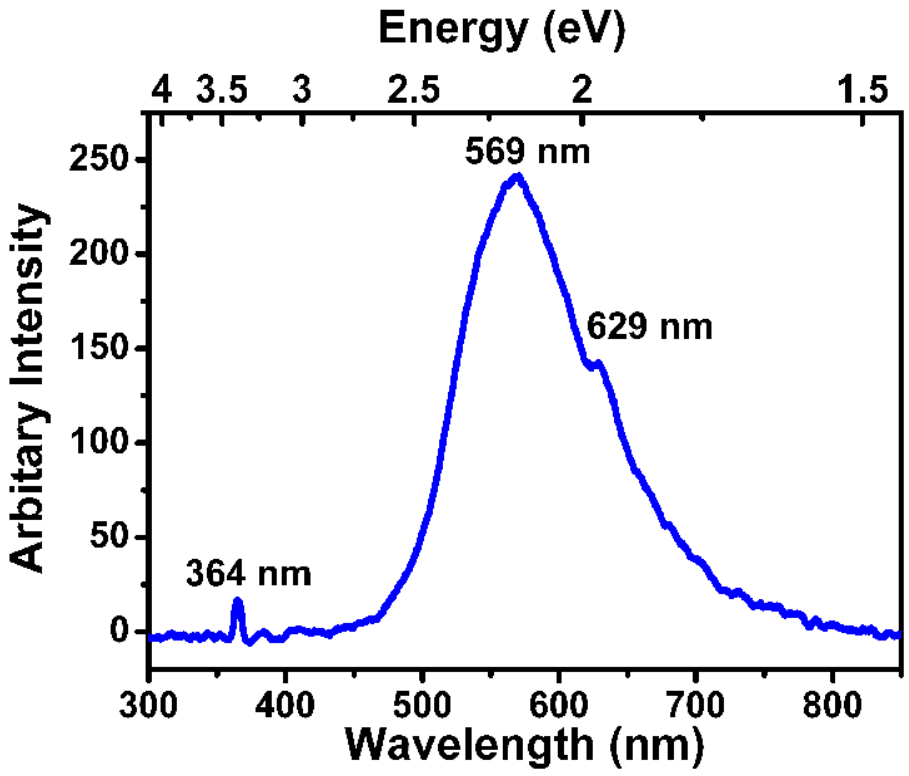

Figure 8. Room temperature PL spectrum of as-deposited ZnO, using an Ar^+ ion laser (λ = 355 nm) as the excitation source.

II. Chemical Bath Deposition of Epitaxial ZnO on Au Single Crystals from Alkaline Solution

*Guojun Mu,[†] Elizabeth A. Kulp,[†] Rakesh V. Gudavarthy,[†] Vishnu Rajasekharan,[†] Xinwei Lan,[‡] and Jay A. Switzer[†,]**

[†] Department of Chemistry and Graduate Center for Materials Research, [‡]Department of Electrical and Computer Engineering, Missouri University of Science and Technology, Rolla, MO 65409

* To whom correspondence should be addressed, e-mail: jswitzer@mst.edu

ABSTRACT

Epitaxial ZnO nanocolumns were deposited onto Au(100), (110) and (111) single crystal substrates from highly alkaline solutions of Zn(II) at 70 ^{o}C using chemical bath deposition. The driving force for deposition is the excess of saturation of Zn(II) in the deposition solution. XRD patterns and SEM micrographs show that below 60 ^{o}C the deposits is ε-$Zn(OH)_2$, whereas at 60 ^{o}C and above pure ZnO is obtained. The activation energy (E_a) is 70 kJ/mol for depositing $Zn(OH)_2$ and 32 kJ/mol for depositing ZnO. The green emission (500-700 nm) of ZnO in PL spectrum is dramatically eliminated by post deposition calcination. And the remaining of the green emission at 333 nm is re Na impurity in the ZnO. The epitaxial relationships between ZnO and Au determined by X-ray θ-2θ scan and X-ray pole figures on Au(100), Au(110), and Au(111) are $ZnO(0001)[1\bar{0}11]$ //$Au(100)[011]$ and $ZnO(0001)[\bar{1}100]$ //$Au(100)[0\bar{1}1]$, $ZnO(0001)[1\bar{0}11]$ //$Au(110)[001]$, and $ZnO(0001)[10\bar{1}1]$ //$Au(111)[\bar{1}10]$.

KEYWORDS zinc oxide, epitaxy, chemical bath deposition, photoluminescence, Raman spectroscopy.

INTRODUCTION

Zinc oxide (ZnO) one-dimensional nanostructures have received considerable attention for their photovoltaic,[1-4] piezoelectric,[5,6] and optoelectronic[7-10] properties. To enhance the film quality, numerous methods have been developed to grow epitaxial ZnO nanostructures on single crystal substrates, including molecular beam epitaxy,[11,12] pulsed laser deposition,[13] chemical vapor deposition,[14] hydrothermal deposition,[15-17] electrodeposition,[18-20] and chemical bath deposition.[22-24] Among these methods, the low-cost solution phase approaches of electrochemical deposition and chemical bath deposition are especially appealing, because the morphology and crystal structures of the deposits can be controlled under low temperatures and ambient pressures.

By exploiting the amphoteric nature of ZnO, our group has recently reported electrodeposition and chemical bath deposition of epitaxial layers of ZnO on single crystal Au[21] and Si.[22] In the electrodeposition of ZnO,[21] the Zn(II) ions were firstly dissolved in highly alkaline solutions, then by electro-oxidizing ascorbate ions, the pH value in the vicinity of the working electrode (Au) was decreased, and ZnO was deposited on the Au surface as a result. In the chemical bath deposition,[22] the Zn(II) ions were maintained in the state of supersaturation in the alkaline solutions, and deposition occurred spontaneously on the Si(001) surface, along with homogeneous precipitation in the solution. In both cases, epitaxial ZnO was produced. On low-index Au single crystals, a strong (0001) orientation was found for the ZnO deposits, whereas on Si the ZnO nanospears tilted at 51^{o} relative to the surface normal bringing ZnO$(20\bar{2}3)$ planes into

coincidence with the of Si(001) planes. The tilted nanostructure on Si(001) produced small mismatches of -0.25% in the $ZnO[1\bar{2}10]$ direction and -0.99% in $ZnO[25\bar{7}\bar{6}]$ direction.

In both chemical bath deposition[25] and electrodeposition,[26] a competition between the formation of ZnO and $Zn(OH)_2$ has been observed previously. D. Lincot and co-workers proposed OH^- groups as a possible reason for the blue shift of the electrodeposited ZnO band gap emission in the photoluminescence spectrum, since $Zn(OH)_2$ is a larger bandgap material.[27] The OH^- groups in ZnO lattice are also considered to be a possible origin for deep level emissions (500-700 nm).[28] In this paper we show that ε-$Zn(OH)_2$ is the main product at temperatures below 60 ^oC, and ZnO as the only product at 60 ^oC or above. The activation energies (E_a) for producing both ZnO and ε-$Zn(OH)_2$ are measured using the quartz crystal microbalance (QCM). The quality of the deposited ZnO, examined with Raman and PL spectroscopy, is improved by post treatment of thermal annealing. In addition, we report that epitaxial ZnO can be chemically deposited on Au single crystals from alkaline solution.

EXPERIMENTAL SECTION

Powder Precipitation. Stock solution was made by dissolving 80 mM $Zn(NO_3)_2 \cdot 6H_2O$ into 2.5 M NaOH solution. 100 mL of this stock solution was added to 900 mL DI water that was stirred at 300 rpm. Both the stock solution and DI water were maintained at a desired temperature (30-90 ^oC). The final deposition solution contained 0.25 M of NaOH and 8 mM of Zn(II). After 30 minutes of precipitation, the powders were filtered, rinsed with DI water, and dried at room temperature.

Film Deposition. 20 mL of the above stock solution was added to 180 mL of DI water that was stirred at 300 rpm. Both the stock solution and DI water were maintained at a desired temperature (30-90 ^{o}C). Immediately after adding the stock solution, the substrates were placed into the deposition solution. After a 30-minute deposition, the substrate was taken out from the solution, rinsed with DI water, and dried at room temperature.

The substrates on which ZnO was deposited include: polycrystalline Au on glass, and Au(100), (110), (111) single crystals. The Au-glass was pretreated by sonicating in a 1:1 water-ethanol solution, and then rinsing with DI water. The gold single crystals were first rinsed with ethanol thoroughly, then they were electrochemically polished by applying an anodic current of 1.6 A/cm^2 with a graphite counter electrode for 30 seconds in a solution containing 2:1:1 ethanol ethylene glycol and HCl. After electropolishing, the crystals were rinsed thoroughly with ethanol and DI water.

For Raman and photoluminescence measurements, purer ZnO sample were deposited on polycrystalline Pt substrate using Teflon beakers and higher grade chemicals ($Zn(NO_3)_2 \cdot 6H_2O$ into 2.5 M NaOH).

Characterization. X-ray powder diffraction patterns on powders were obtained with a Scintag 2000 diffractometer using Cu Kα radiation. X-ray θ-2θ scans on films were obtained with a high-resolution Philips X'Pert diffractometer using Cu Kα source radiation with a combination X-ray mirror and two-crystal Ge(220) two-bounce hybrid monochromator (PW3147/00) as the incident beam module and a 0.18 parallel plate collimator (PW3098/18) as the diffracted beam module. X-ray pole figures of epitaxial films were collected on the same instrument in point-focus mode using a crossed-slit

collimator (PW3084/62) as the primary optics and a flat graphite monochromator (PW3121/00) as the secondary optics. The morphologies of films were studied with a Hitachi S-4700 field-emission scanning electron microscope (SEM). Thermogravimetry (TG) and differential thermal analysis (DTA) on powders were preformed with a Netzsch simultaneous TGA/DTA instrument in air environment, heating from 25 to 1,000 ^{o}C at a rate of 10 ^{o}C/min. The Raman spectrum was obtained using a LabRAM ARAMIS Raman spectroscopy system (Jobin Yvon Inc.). A built-in 632.8 nm HeNe laser was focused onto the center of the sample through a 10× microscope objective (NA=0.25). PL spectra were collected on the ZnO samples deposited on Pt using a Fluorolog-3 spectrofluorometer (Horiba-Yvon, Edison, NJ, USA) with a Xe lamp as excitation source and a front-face emission configuration. The Xe lamp spectrum and a water Raman spectrum were used to calibrate the excitation and the emission gratings. All measurements were taken at room temperature under identical settings: 305 nm excitation wavelength, 250 nm long-pass filter, 5 nm excitation slit width, 5 nm emission slit width, 1.0 seconds integration time, and1.0 nm step size.

Activation Energy (E_a) Determination. The rate of ZnO growth was measured with a gold-coated quartz crystal microbalance (QCM), MAXTEK PM 710 monitor system, at a series of deposition temperatures from 30 to 90 ^{o}C during the first 25 seconds of deposition. The surface area of Au exposed to the solution was 1.37 cm^2.

RESULTS AND DISCUSSION

As an amphoteric material, ZnO can be dissolved in both acidic and basic solutions. To avoid inducing possible impurities into the ZnO deposits, nothing besides NaOH and $Zn(NO_3)_2$ was added into the deposition solution. In the deposition solution

that contains 0.25 M base, Zn(II) ions exist in the forms of zincate, $Zn(OH)_x^{2-x}$ (x=0-4). The mechanism for depositing ZnO is the same as described in our earlier paper,[22] that is to slightly exceed the saturation state of the solution. To determine the solubility of ZnO versus solution pH, the solubility diagram and species distribution of ZnO aqueous solution were calculated under different temperatures.

Equations 1-5 show the expressions of the distribution fraction (α) for each zincate species in the aqueous solution, where β is the accumulated stability constant of the zincate species, $[Zn^{2+}]$ is the concentration of Zn^{2+} free ions, and [Zn(II)] is the saturation concentration of overall Zn(II) ions. According to the definition of K_{sp}, the ratio of $[Zn^{2+}]/[Zn(II)]$ equals to $K_{sp}/[OH^-]^2$. As a result, the distribution fraction α can be solved as a function of solution pH. Similarly, the solubility (S) of ZnO, written as [Zn(II)] in Equation 6, can be also resolved as a function of solution pH.

$$\alpha_{Zn^{2+}} = \frac{[Zn^{2+}]}{[Zn(II)]} \tag{1}$$

$$\alpha_{Zn(OH)^+} = \frac{[Zn(OH)^+]}{[Zn(II)]} = \frac{[Zn^{2+}]\beta_1[OH^-]}{[Zn(II)]} \tag{2}$$

$$\alpha_{Zn(OH)_2} = \frac{[Zn(OH)_2]}{[Zn(II)]} = \frac{[Zn^{2+}]\beta_2[OH^-]^2}{[Zn(II)]} \tag{3}$$

$$\alpha_{Zn(OH)_3^-} = \frac{[Zn(OH)_3^-]}{[Zn(II)]} = \frac{[Zn^{2+}]\beta_3[OH^-]^3}{[Zn(II)]} \tag{4}$$

$$\alpha_{Zn(OH)_4^{2-}} = \frac{[Zn(OH)_4^{2-}]}{[Zn(II)]} = \frac{[Zn^{2+}]\beta_4[OH^-]^4}{[Zn(II)]} \tag{5}$$

$$[Zn(II)] = [Zn^{2+}] + [Zn(OH)^+] + [Zn(OH)_2] + [Zn(OH)_3^-] + [Zn(OH)_4^{2-}] = [Zn^{2+}](1 + \beta_1[OH^-] + \beta_2[OH^-]^2 + \beta_3[OH^-]^3 + \beta_4[OH^-]^4) = \frac{K_{sp}}{[OH^-]^2}(1 + \beta_1[OH^-] + \beta_2[OH^-]^2 + \beta_3[OH^-]^3 + \beta_4[OH^-]^4) \tag{6}$$

The values of β and K_{sp} at above room temperature, as shown in Table 1, were calculated from the Gibbs free energy ($\Delta_r G^o$) and heat capacity (C_p) using Equations 7 & 8 and standard thermodynamic data taken from publications of the Lincot group.[29,30]

$$\Delta_f G_T^o = \Delta_f G_{298}^o + \int_{298}^{T} C_p(T)dT - S_{298}^o(T-298) - T\int_{298}^{T} C_p(T)\frac{dT}{T} \quad (7)$$

$$C_p(T) = a + b\times10^{-3}T + c\times10^{5}T^{-2} + d\times10^{-6}T^{2} \quad (8)$$

The deposition was carried out at temperatures from 25 to 90 ^{o}C. To avoid the formation of $Zn(OH)_2$, however, 70 ^{o}C was used when depositing epitaxial ZnO nanostructures on Au single crystals. The resulting species distribution and solubility diagrams are shown at 25 and 70 ^{o}C (see Figure 1). Due to the change of K_w with temperature, the pH value of a solution containing 0.25 M NaOH is 13.4 at 25 ^{o}C, and shifts to 12.2 at 70 ^{o}C. As shown in Figure 1, a saturated solution at 25 ^{o}C and pH 13.4 can dissolve 6.5 mM ZnO at maximum (81.5% of $Zn(OH)_4^{2-}$ and 18.5% of $Zn(OH)_3^-$); whereas at 70 ^{o}C and pH 12.2 it dissolves 4.0 mM ZnO (68.4% of $Zn(OH)_4^{2-}$ and 31.6% of $Zn(OH)_3^-$). In practice, 20 mL of concentrated solution was added into 180 mL water that was maintained at a certain temperature to make a final deposition solution that contained 0.25 M NaOH and 8 mM $Zn(NO_3)_2$. Such a deposition solution was in the state of supersaturation at temperatures from 30 to 90 ^{o}C. Due to the sluggish nature of the precipitation, a couple of minutes later ZnO thin film was deposited on the substrate surface accompanied with homogeneous precipitated ZnO powders in the solution.

XRD patterns on the powders collected from the solution are shown in Figure 2. The deposition temperature is lower than 60 ^{o}C, the powders are primarily $Zn(OH)_2$, while at 60 ^{o}C or above pure ZnO is obtained. Figure 3 shows the SEM images of the

deposits on Au-glass substrates. Consistent with the powders, at 55 ^{o}C or lower, the deposits are mostly large $Zn(OH)_2$ orthorhombic crystals and a minor amount of smaller ZnO hexagonal crystals. At 60 ^{o}C or above, pure ZnO hexagonal columns were obtained. The ZnO nanocolumns are of a preferred (0001) orientation on the (111)-oriented Au-glass textured substrates.

The kinetics of the deposition process was studied by monitoring the mass increase onto the substrate surface with an Au-coated quartz crystal microbalance (QCM) system in the initial 25 seconds of deposition. Figure 4 shows the mass gain on the microbalance due to the deposition of ZnO at a series of deposition temperatures (30-90 ^{o}C). The slope of each line represents the deposition rate (in the unit of μg/hr) at that temperature. At the initial stage of the deposition, the concentration of each reactant remains constant, and as a result the deposition is regarded as a pseudo-zero order reaction which rate straightly equals to the rate constant (*k*). Figure 5 shows the Arrhenius plot for this reaction, *ln(k)* versus *1/T*, which breaks into two straight lines at around 60 ^{o}C. At temperatures below 60 ^{o}C, $Zn(OH)_2$ deposits with an activation energy of 70 kJ/mol. At temperatures above 60 ^{o}C, ZnO deposits with an activation energy of 32 kJ/mol. The activation energy for ZnO deposition is close to the 33.8 kJ/mol for precipitation of ZnO nanoparticles from NaOH and $Zn(Ac)_2$ solutions that was measured by P. Searson and co-workers.[31]

Based on the standard Gibbs free energy ($\Delta_r G^o$) of the deposition reactions, as in Equations 9 & 10, the producing of ZnO is thermodynamically favored compared to that of $Zn(OH)_2$.

$$Zn(OH)_4^{2-}(aq) \Leftrightarrow Zn(OH)_2(s) + 2OH^-(aq) \qquad \Delta_r G^o_{Zn(OH)_2(s)} = -5.7kJ/mol \tag{9}$$

$$Zn(OH)_4^{2-}(aq) \Leftrightarrow ZnO(s) + H_2O(l) + 2OH^-(aq) \qquad \Delta_r G^o_{ZnO(s)} = -7.4kJ/mol \tag{10}$$

The overall reaction coordinate is shown in Figure 6, taking both products into account. A question may rise up to this point, that is how $Zn(OH)_2$ can become a dominant product at below 60 ^oC if it is not favored either thermodynamically or kinetically. A possible answer could be that $Zn(OH)_2$ may serve as an intermediate product during the deposition process from alkaline solutions, which forms ZnO by a following endothermal dehydration reaction. A growth unit model was proposed earlier by different groups[32,33] to understand the effect of OH^- groups on the pyramid morphology of ZnO nanocolumns grown from alkaline solutions. According to this model, $Zn(OH)_4^{2-}$ dianions, the precursor of growing ZnO crystal from alkaline solutions, are bonded together through a dehydration reaction to form larger $Zn_xO_y(OH)_z^{n-}$ clusters and finally ZnO crystals.

Figure 7a shows the TG/DTA analysis on the $Zn(OH)_2$ powder collected at 40 ^oC. At 32-117 ^oC, the powder underwent an endothermal change accompanied with ~0.3% weight loss, which is due to the evaporation of the surface moisture from the sample. Between 120-680 ^oC, the endothermal change with total mass loss of 17.5 % can be identified as dehydration of the $Zn(OH)_2$ crystal to form ZnO and water vapor(Δm = 18.12%, $\Delta_r H^o$ = +335.4 kJ/mol[34]), which is proved by the XRD analysis on the powders before and after annealing at 200 ^oC for 2 hours. Above 800 ^oC, a small exothermal change with no further mass loss may be assigned as the start of melting of ZnO nanostructures. Although the melting point of ZnO bulk material is much higher (1974 ^oC[35]), the SEM image showed smoother edges in ZnO hexagonal columns. Figure 7b

shows the TG/DTA analysis on the ZnO powder collected at 70 ^{o}C, which is pretty similar with Figure 7a. The surface moisture was removed at 30-121 ^{o}C (Δm = -0.016 %), followed with the dehydration of the $Zn(OH)_2$ impurity in ZnO crystal to form more pure ZnO (Δm = -1.55 %) at 121-650 ^{o}C. Starting from 650 ^{o}C, an exothermal change occurs with no further mass change.

To study the influence of the OH^- impurity on the quality of the deposited ZnO crystal, the ZnO crystal that was deposited on Pt polycrystalline substrate from by chemical bath deposition from alkaline solution, Raman and PL spectra were obtained on the samples as deposited at 70 ^{o}C and after thermal treatment at 700 ^{o}C for 1 hour. The Raman spectrum in Figure 8 shows that the as deposited film exhibits typical Raman scattering of ZnO crystal. The scattering peaks at 375 and 437 cm^{-1} are assigned to ZnO A_1(TO) and E_2-high phonon mode, respectively.[36,37] The scattering at 325 cm^{-1} is due to possible multiple-phonon scattering processes of ZnO.[38] Figure 9a shows the photoluminescence spectra of the ZnO as-deposit (black) and after annealing (blue) on polycrystalline Pt from a deposition solution containing 0.25 M NaOH and 6 mM Zn(II), Figure 9b is the PL spectra of the ZnO as-deposit (black) and after annealing (blue) on polycrystalline Pt from a deposition solution containing 0.25 M NH_4OH and 6 mM Zn(II). For the ZnO as deposited, the UV emission is hard to observe and a much stronger visible emission at 500-700 nm is simulated with three Guassian peaks at 518, 575, and 681 nm. After annealing, the peaks at 575 and 681 nm disappear, only leaving the 518 nm peak visible. Combing the TG/DTA analysis, after annealing at 700 ^{o}C, the water or OH^- groups on the ZnO surface or in the lattices is removed, so the deep level emissions at 575 and 681 nm should be assigned as water or OH^- group impurities in ZnO, while the

emission at 518 nm should be assigned as other reasons. Since the NaOH was used as base in the deposition solution, one possible impurity that could be induced in ZnO is Na^+. Then the ZnO is deposited from amoinia solution to eliminate inducing the impurity of Na^+ to the ZnO crystal, as show in Figure 9b. The as-deposit film dose not show much difference from Figure 9a, however after annealing the green emission is much lower in intensity, and a clear exciton emission show up at 374 nm (3.34 eVs), which means the quality of ZnO is highly improved using NH_4OH as base and by post annealing process.

Epitaxial ZnO nanocolumns were produced on single crystal Au(100), (110), and (111) substrates. The depositions were carried out at 70 ^oC to eliminate the formation of $Zn(OH)_2$. The SEM images in Figure 10 reveal that ZnO are grown into hexagonal nanocolumns with diameter of 100-500 nm. The ZnO nanocolumns show a strong (0001) orientation (c-axis). On the Au(100) substrate (Figure 10a), the hexagons have two in-plane alignments separated by 30^o. Whereas on Au(110) (Figure 10b), and Au(111) (Figure 10c) the hexagons are uniformly aligned. X-ray θ-2θ scan patterns in Figure 11 show only ZnO (0002) and (0004) peaks and corresponding Au peaks, which is coincident with SEM and indicates that the ZnO deposits have a preferred (0001) out-of-plane orientation. To determine the in-plane configurations of ZnO, X-ray pole figure technique is applied. Figure12 (a), (c) and (e) are the ZnO$(10\bar{1}1)$ pole figures for ZnO on Au(100), (110) and (111), respectively. The pole figures were acquired by choosing the 2θ of 35.379^o for ZnO$(10\bar{1}1)$ plane to set up the X-ray source and detector, then tilting the sample surface over an angle (χ) from 0-90^o, and rotating it azimuthally (φ) from 0-360^o at each tilt angle. In each pole figure, the radial grid lines correspond to 30^o increments in tilt angle (χ). The color of the spots differentiates the diffracted intensity. Figure 11 (a)

shows twelve equally spaced spots at χ=62^o, which correspond to two set of ZnO$(10\bar{1}1)$ reflections to the ZnO(0001) plane separated by 30^o (six-fold symmetry for each set of reflection), which is consistent with the SEM image in Figure 10(a). Figure 11(c) and (e) each show six equally spaced spots at χ=62^o, one set of ZnO$(10\bar{1}1)$ reflection to ZnO(0001) plane. The pole figures in Figure 11(b), (d) and (f) are the Au(111) substrate pole figure on Au(100), (110), and (111) respectively. These substrate pole figures were acquired by setting up the X-ray source and detector at 2θ of 38.184^o for Au (111) plane, and then tilting (χ) and rotating (φ) the sample as mentioned above. In Figure 11(b), the four equally spaced spots at χ=56.9^o correspond to one set of Au (111) reflections to an Au (100) plane (four-fold symmetry). Figure 10(d) has two spots at χ=56.9^o, corresponding to one set of Au (111) reflections to an Au (110) plane (two-fold symmetry). And Figure (f) has one spot at the center χ=0^o, and three equally spaced spots at χ=56.9^o, which indicates one set of Au (111) reflections to an Au (111) plane.

By comparing the pole figure to its calculated stereographic projection, the epitaxial relationship between the ZnO deposit and Au substrate can be determined. For ZnO(0001) on Au(100), the epitaxial relationship is ZnO(0001)$[10\bar{1}1]$ //Au(100)[011] and ZnO(0001)$[\bar{1}100]$ //Au(100)$[0\bar{1}1]$, which mean that ZnO (0001) and Au (100) out-of-plane orientation are parallel, ZnO$[10\bar{1}1]$ and Au [011] in-plane orientations are coincident, as well as ZnO$[\bar{1}100]$ and Au$[0\bar{1}1]$ in-plane orientations are coincident. For ZnO(0001) on Au(110) substrate, the epitaxial relationship is ZnO(0001)$[10\bar{1}1]$ //Au(110)[001]; whereas, for ZnO(0001) on Au(111), it is ZnO(0001)$[10\bar{1}1]$ //Au(111)$[\bar{1}10]$.

CONCLUSIONS

Chemical bath deposition of zinc oxide was executed from alkaline solutions. The deposition solutions that contained 0.25 M NaOH and 8 mM $Zn(NO_3)_2$ were supersaturated at temperatures from 25 to 90 ^oC, according to the ZnO solubility diagram. Both homogeneous precipitates and heterogeneous deposits occur from the system. At 55 ^oC and lower, $Zn(OH)_2$ and a small fraction of ZnO mixtures were obtained; while at 60 ^oC and above, pure ZnO were produced. The kinetics of deposition was studied by recording the mass increase on a gold-coated quartz crystal microbalance in the initial 25 seconds of deposition. E_a for $Zn(OH)_2$ deposition (< 60 ^oC) was 70 kJ/mol, and for ZnO deposition (≥ 60 ^oC) was 32 kJ/mol. The photoluminescence and Raman spectra of ZnO samples both as-deposit and after annealing were obtained. They show that the as-deposit ZnO samples have a defect in the crystal structure, which is removed by annealing the sample at 700 ^oC for 1 hour. Epitaxial ZnO films were deposited on Au single crystal substrates. The epitaxial relationships between ZnO and Au were determined by X-ray pole figure technique: $ZnO(0001)[1\bar{0}11]$ //$Au(100)[011]$ and $ZnO(0001)[\bar{1}100]$ //$Au(100)[0\bar{1}1]$, $ZnO(0001)[1\bar{0}11]$ //$Au(110)[001]$ and $ZnO(0001)[1\bar{0}11]$ //$Au(111)[\bar{1}10]$.

ACKNOWLEDGEMENTS. This work was supported by the U.S. Department of Energy, Office of Basic Energy Sciences under Grant No. DE-FG02-08ER46518.

REFERENCES

1. Martinson, A. B.; Goes, M. S.; Fabregat-Santiago, F.; Bisquert, J.; Pellin, M. J.; Hupp, J. T. *J. Phys. Chem.* **2009**, *113*, 4015.
2. Ahn, K. S.; Shet, S.; Deutsch, T.; Jiang, C. S.; Yan, Y.; Al-Jassim, M.; Turner, J. *J. Power Sources* **2008**, *176*, 387.
3. Kong, J.; Chu, S.; Olmedo, M.; Li, L.; Yang, Z.; Liu, J. *Appl. Phys. Lett*. **2008**, *93*, 132113/1.
4. Konenkamp, R.; Word, R. C.; Godinez, M. *Nano Lett*. **2005**, *5*, 2005.
5. Hu, Y.; Chang, Y.; Fei, P.; Snyder, R. L; Wang, Z. L. *ACS nano* **2010**, *4*, 1234.
6. Wang, Z. L.; Song, J. *Science* **2006**, *312*, 242.
7. Bayram, C.; Teherani, F. Hosseini; Rogers, D. J.; Razeghi, M. *Appl. Phys. Lett*. **2008**, *93*, 081111/1.
8. Bao, J.; Zimmler M. A.; Capasso, F.; Wang, X.; Ren, Z. F. *Nano Lett*. **2006**, *6*, 1719.
9. Huang M. H.; Mao S.; Feick H.; Yan H.; Wu Y.; Kind H.; Weber E.; Russo R.; Yang P. *Science* **2001**, *292*, 1897.
10. Tang, Z. K.; Wong, G. K. L.; Yu, P.; Kawasaki, M.; Ohtomo, A.; Koinuma, H.; Segawa, Y. *Appl. Phys. Lett*. **1998**, *72*, 3270.
11. Hamdani, F.; Yeadon, M.; Smith, D. J.; Tang, H.; Kim, W.; Salvador, A.; Botchkarev, A. E.; Gibson, J. M.; Polyakov, A. Y.; Skowronski, M.; Morkoc, H. *J. Appl. Phys*. **1998**, *83*, 983.
12. Lim, S. H.; Shindo, D.; Kang, H. B.; Nakamura, K. *J. Cryst. Grow*. **2001**, *225*, 208.
13. Pant, P.; Budai, J. D.; Aggarwal, R.; Narayan, R. J.; Narayan, J. *J. Phys. D* **2009**, *42*, 105409/1.
14. Kim, D. C.; Kong, B. H.; Jeon, S. Y.; Yoo, J. B.; Cho, H. K.; Park, D. J.; Lee, J. Y. *J. Mater. Res.* **2007**, *22*, 2032.
15. Le, H. Q.; Chua, S. J.; Koh, Y. W.; Loh, K. P.; Fitzgerald, E. A. *J. Cryst. Growth* **2006**, *293*, 36.
16. Andeen, D.; Loeffler, L.; Padture, N.; Lange, F. F. *J. Cryst. Growth* **2003**, *259*, 103.
17. Andeen, D.; Kim, J. H.; Lange, F. F.; Goh, G. K. L.; Tripathy, S. *Adv. Funct. Mater*. **2006**, *16*, 799.
18. Pauporte, T.; Lincot, D.; Viana, B.; Pelle, F. *Appl. Phys. Lett*. **2006**, *89*, 233112/1.
19. Ichinose, K.; Yoshida, T. *Phys. Stat. Sol. A* **2008**, *205*, 2376.

20. Liu, R.; Vertegel, A. A.; Bohannan, E. W.; Sorenson, T. A.; Switzer, J. A. *Chem. Mater*. **2001**, *13*, 508.

21. Limmer, S. J.; Kulp, E. A.; Switzer, J. A. *Langmuir* **2006**, *22*, 10535.

22. Mu, G.; Gudavarthy, R. V.; Kulp, E. A.; Switzer, J. A. *Chem. Mater*. **2009**, *22*, 3960.

23. Peterson, R. B.; Fields, C. L.; Gregg, B. A. *Langmuir* **2004**, *20*, 5114.

24. Wessler, B.; Steinecker, A.; Mader, W. *J. Cryst. Growth* **2002**, *242*, 283.

25. Cruz-Vazquez, C.; Rocha-Alonzo, F.; Burruel-Ibarra, S. E.; Barboza-Flores, M.; Bernal, R.; Inoue, M. *Appl. Phys. A* **2004**, *79*, 1941.

26. Peulon, S.; Lincot, D. *J. Electrochem. Soc.* **1998**, *145*, 864.

27. Pauporte´, T; Lincot, D. *Electrochimica Acta* **2000**, *45*, 3345.

28. Wang, Q.; Wang, G.; Jie, J.; Han, X.; Xu, B.; Hou, J. G *Thin Solid Films* **2005**, *492*, 61.

29. Goux, A.; Pauporte, T.; Chivot, J.; Lincot, D. *Electrochim. Acta* **2005**, *50*, 2239.

30. Hubert, C.; Naghavi, N.; Canava, B.; Etcheberry, A.; Lincot, D. *Thin Solid Films* **2007**, *515*, 6032.

31. Hu, Z. S.; Oskam, G.; Penn, R. L.; Pesika, N.; Searson, P. C. *J. Phys. Chem. B* **2003**, *107*, 3124.

32. Li, W.-J.; Shi, E.-W.; Zhong, W.-Z.; Yin, Z.-W. *J. Cryst. Grow*. **1999**, *203*, 186.

33. Cryst. Res. Technol. 32 (1997) 5]

34. Dean, J. A. *Lange's Handbook of Chemistry*; McGraw-Hill Professional. **1998**

35. David R. Lide CRC *Handbook of Chemistry and Physics* **2003** pp4-95

36. Klingshirn, C. *Phys. Stat. Sol*. **2007**, *244*, 3027.

37. Chassaing, P. M.; Demangeot, P.; Paillard, V.; Zwick, A.; Combe, N. *Appl. Phys. Lett*. **2007**, *91*, 053108.

38. C. Bundesmann,C.; Ashkenov, N.; Schubert, M.; Spemann, D.; Butz, T.; Kaidashev, E. M.; Lorenz, M.; Grundmann, M. *Appl. Phys. Lett*. **2003**, *83*, 1974.

Table 1. The possible reactions in an aqueous solution containing only base and Zn(II), and their equilibrium constants determined from the free energy of reaction $\Delta_r G_0^o$.

Equations	Constants at 25 °C	Constants at 70 °C
$Zn^{2+}(aq)+OH^-(aq) \leftrightarrows Zn(OH)^+(aq)$	$\beta_1 = \frac{[Zn(OH)^+]}{[Zn^{2+}][OH^-]}$ $10^{6.18}$	$10^{6.72}$
$Zn^{2+}(aq)+2OH^-(aq) \leftrightarrows Zn(OH)_2(aq)$	$\beta_2 = \frac{[Zn(OH)_2]}{[Zn^{2+}][OH^-]^2}$ $10^{10.09}$	$10^{10.22}$
$Zn^{2+}(aq)+3OH^-(aq) \leftrightarrows Zn(OH)_3^-(aq)$	$\beta_3 = \frac{[Zn(OH)_3^-]}{[Zn^{2+}][OH^-]^3}$ $10^{14.28}$	$10^{13.64}$
$Zn^{2+}(aq)+4OH^-(aq) \leftrightarrows Zn(OH)_4^{2-}(aq)$	$\beta_3 = \frac{[Zn(OH)_4^{2-}]}{[Zn^{2+}][OH^-]^4}$ $10^{15.50}$	$10^{14.59}$
$Zn^{2+}(aq)+2OH^-(aq) \leftrightarrows ZnO(s)+H_2O(l)$	$K_{sp,ZnO} = [Zn^{2+}][OH^-]^2$ $10^{16.80}$	$10^{-16.44}$
$H^+(aq)+OH^-(aq) \leftrightarrows H_2O(l)$	$K_w = [H^+][OH^-]$ $10^{13.99}$	$10^{-12.81}$

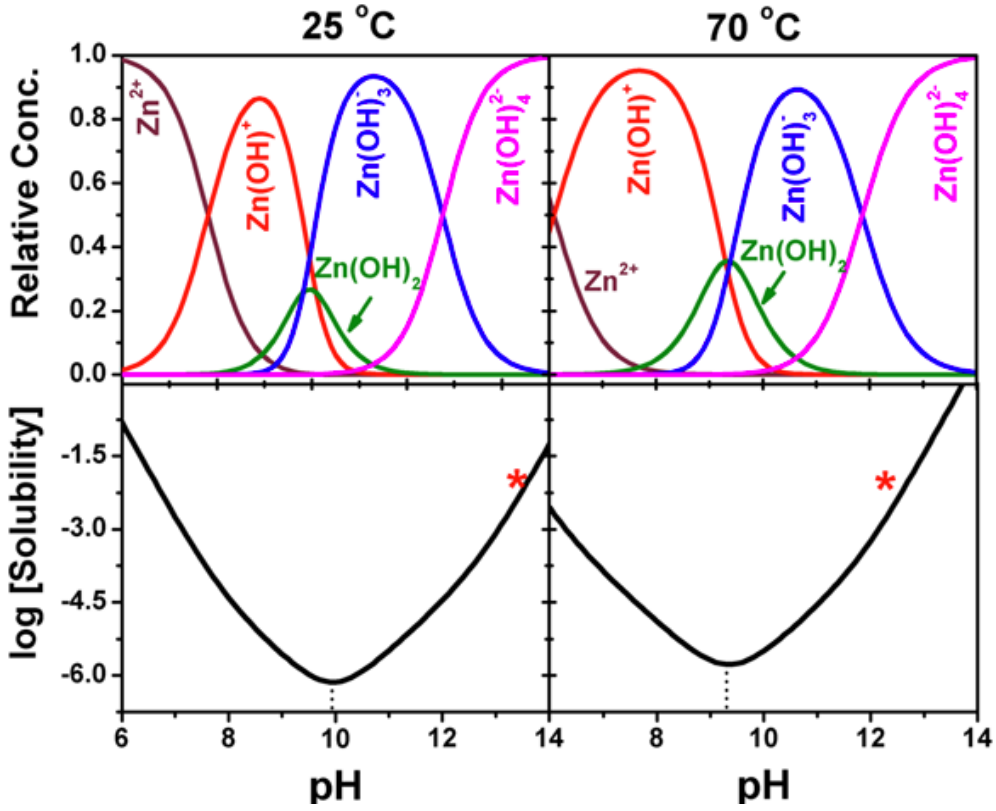

Figure 1. Speciation distributions (upper) and solubility diagrams (lower) of Zn(II) versus pH in aqueous solution at 25 ^{o}C (left) and 70 ^{o}C (right), asterisks representing the slightly oversaturated state of the deposition solution that contains 0.25 M NaOH and 8 mM $Zn(NO_3)_2$.

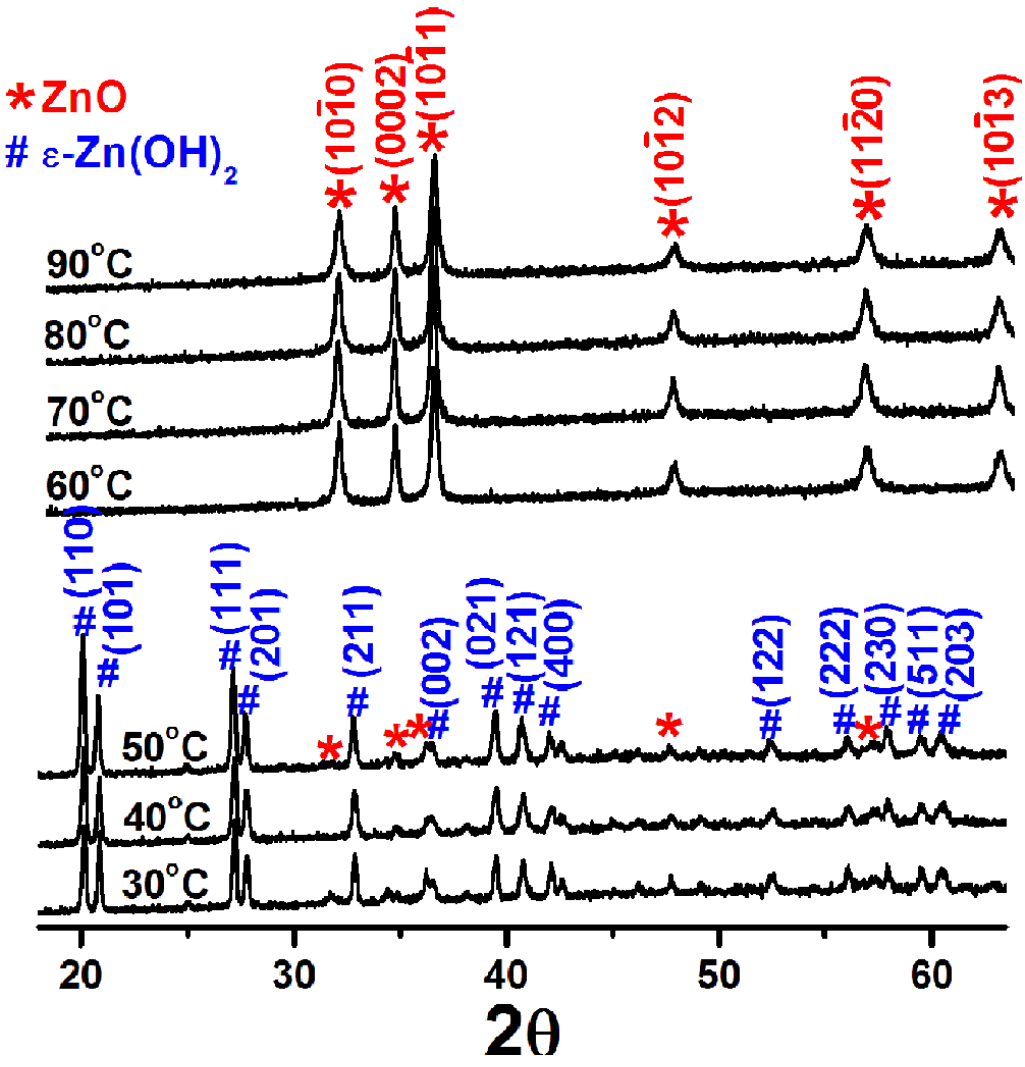

Figure 2. X-ray powder diffraction patterns of the powders collected from the deposition solutions that were maintained at different temperatures of 30-90 ^{o}C, showing the presence of ε-$Zn(OH)_2$ (JCPDS card No. 38-0385) below 60 ^{o}C as well as ZnO (JCPDS card No. 36-1451) at and above 60 ^{o}C.

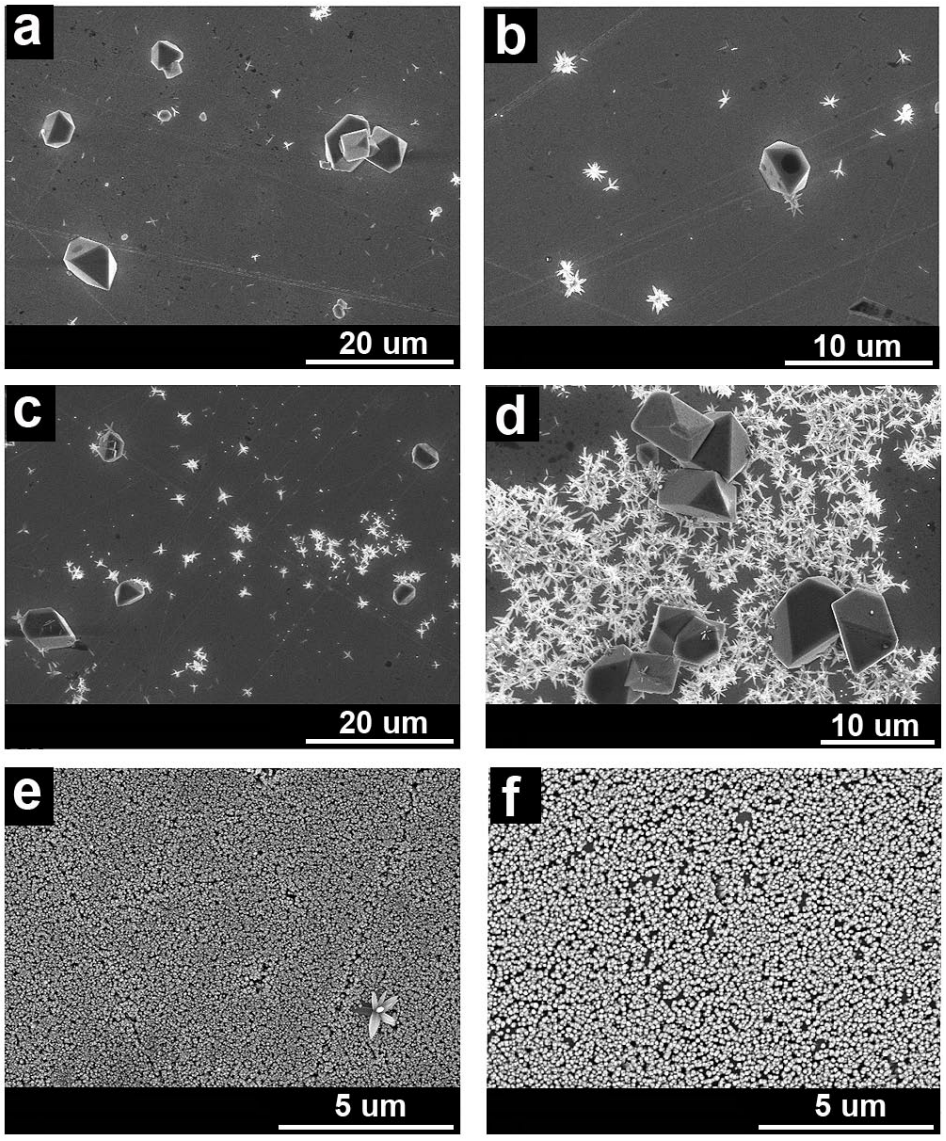

Figure 3. SEM micrographs of the deposits on Au-glass substrates grown at 30 ^{o}C (a), 40 ^{o}C (b), 50 ^{o}C (c), 55 ^{o}C (d), 60 ^{o}C (e), and 70 ^{o}C (f). The large orthorhombic crystals are ε-$Zn(OH)_2$ crystals, and the smaller hexagonal nanocolumns are ZnO.

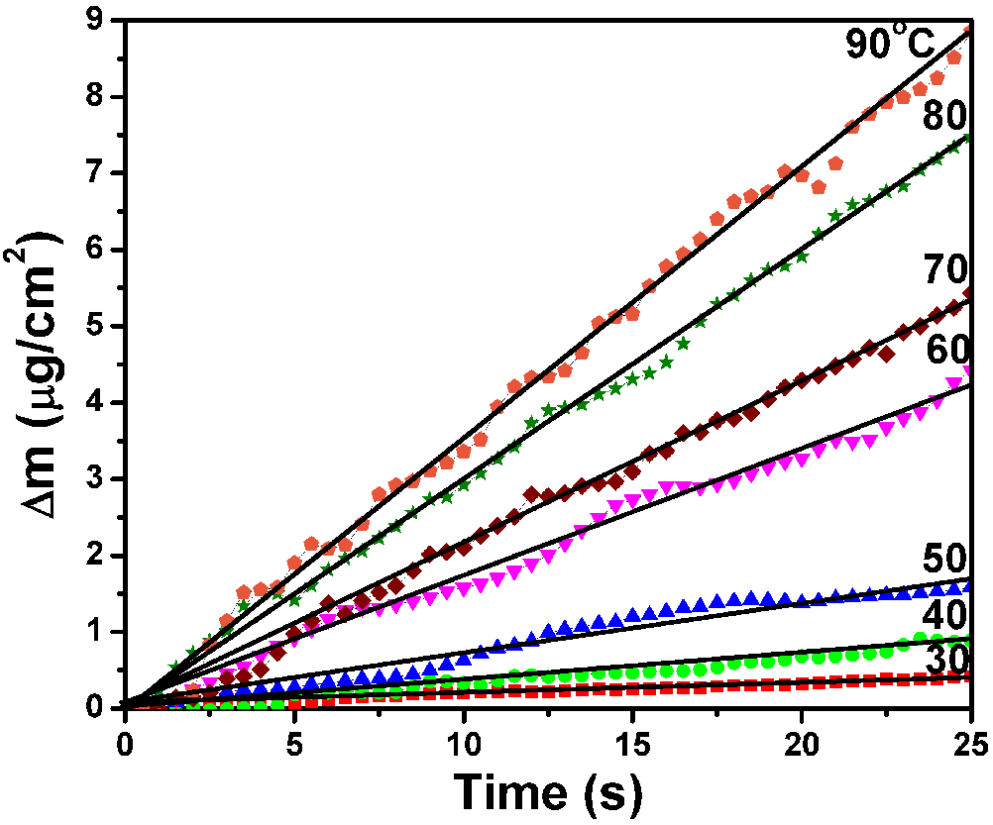

Figure 4. Mass increase (*Δm*) versus time (*t*) measured with an Au-coated quartz crystal microbalance (QCM) system in the initial 25 seconds of deposition at a series of temperatures from 30 to 90 ^{o}C. In a pseudo-zero order reaction, the deposition rate (calculated from the slope of each line) equals to its rate constant (*k*).

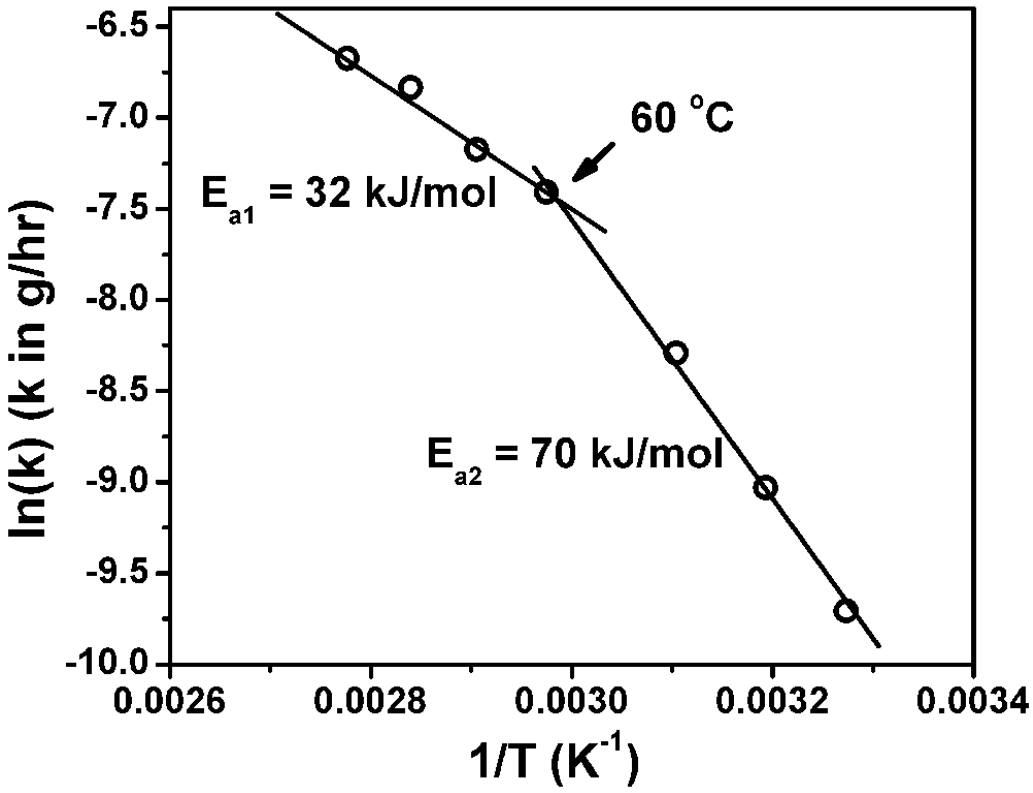

Figure 5. Arrhenius plot of the deposition process, *ln(k)* versus *1/T*, where temperature (*T*) is in the unit of *Kelvin* and rate constant (*k*) is in the unit of *μg/hr*. The breakpoint is due to two different products (ZnO and ε-$Zn(OH)_2$) that are deposited at the two side of this point.

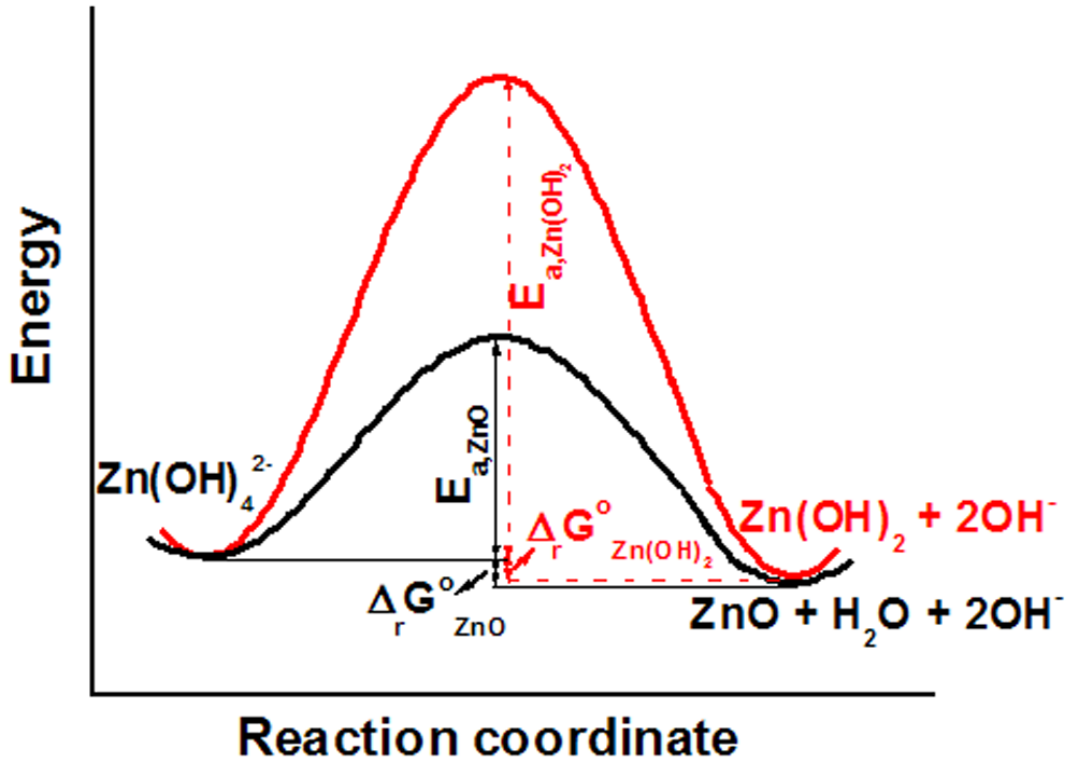

Figure 6. Overall reaction coordinates of the chemical bath deposition processes considering both ZnO and ε-$Zn(OH)_2$ as products.

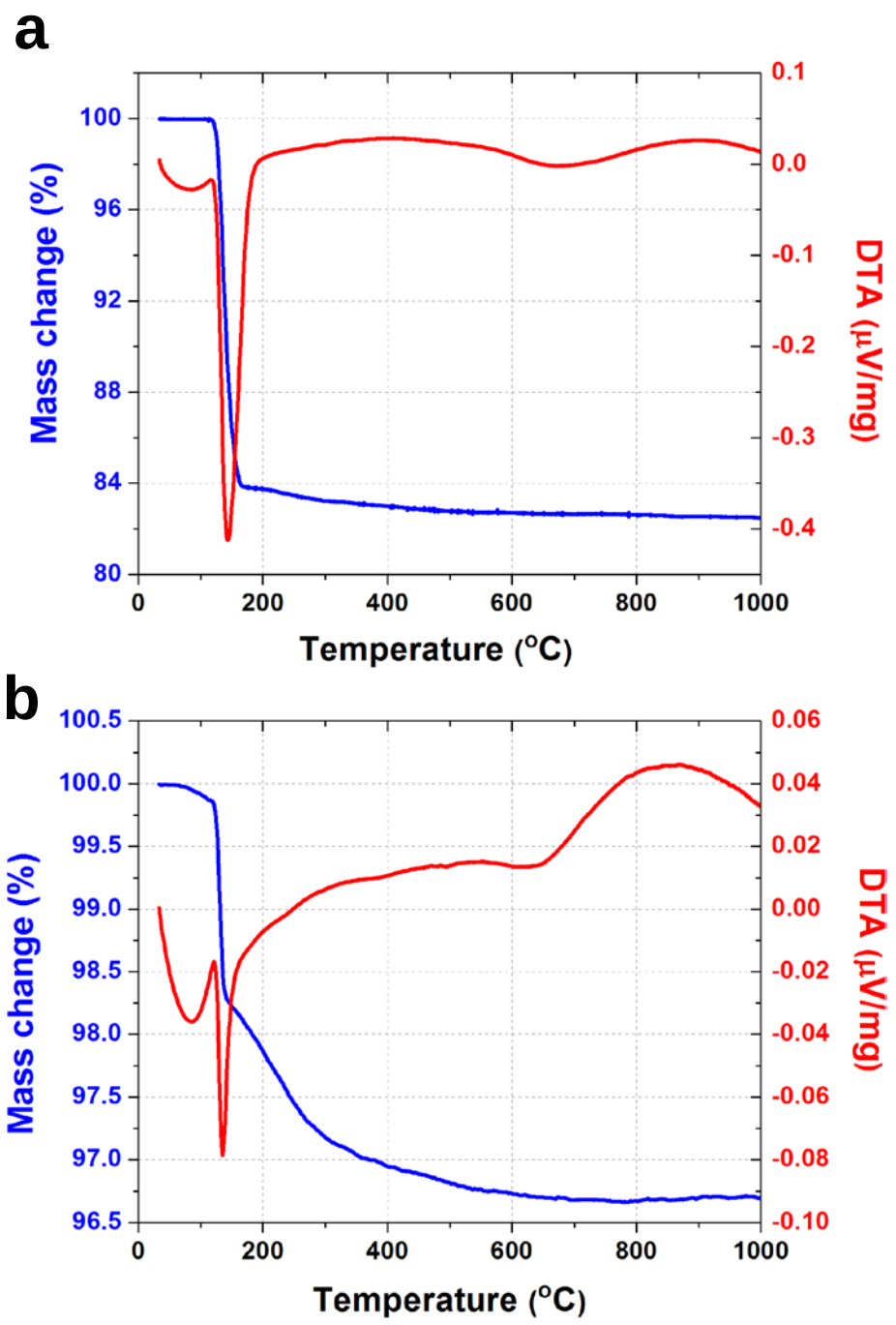

Figure 7. Thermogravimetry (TG) and differential thermal analysis (DTA) on the powders collected at 40 ^{o}C (a) and 70 ^{o}C (b), which were carried out in air environment, temperature increasing from 25 to 1,000 ^{o}C at a rate of 10 ^{o}C/min.

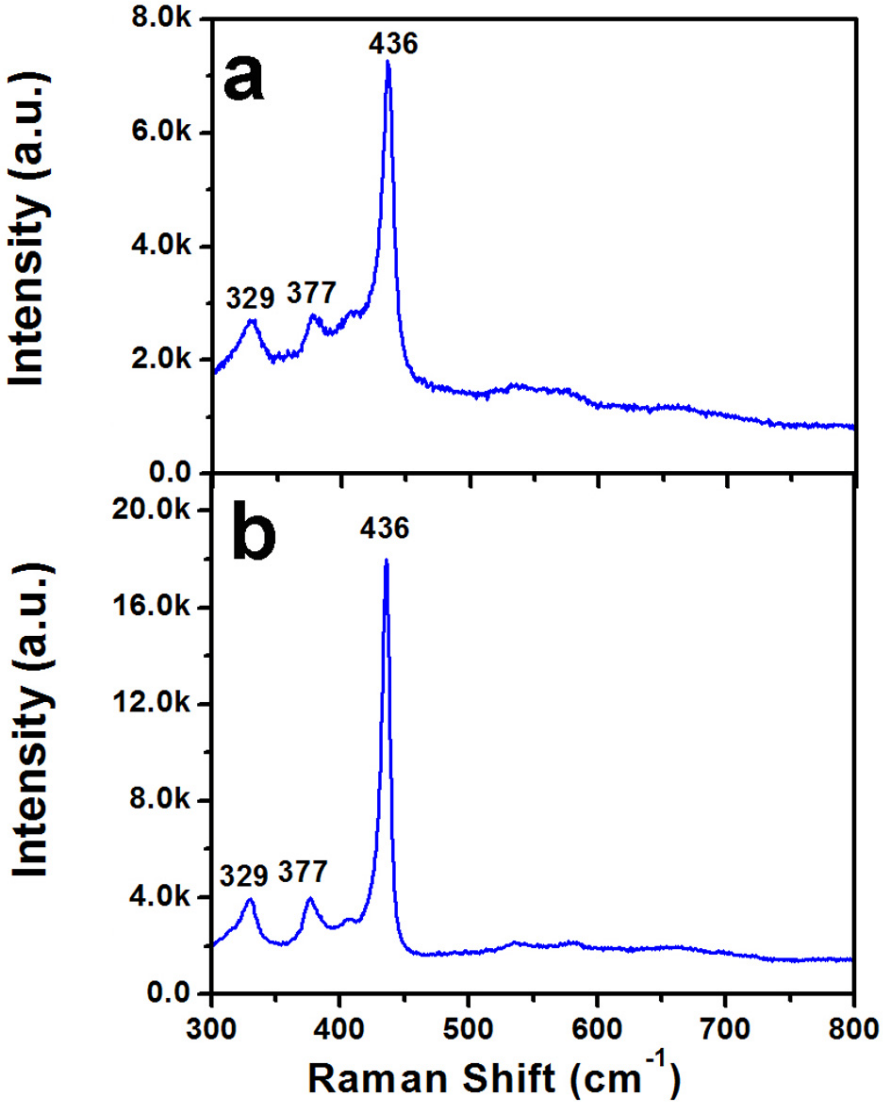

Figure 8. Raman spectra on the ZnO as deposited on polycrystalline Pt (a) and after calcination at 700 ^{o}C for 1 hour (b).

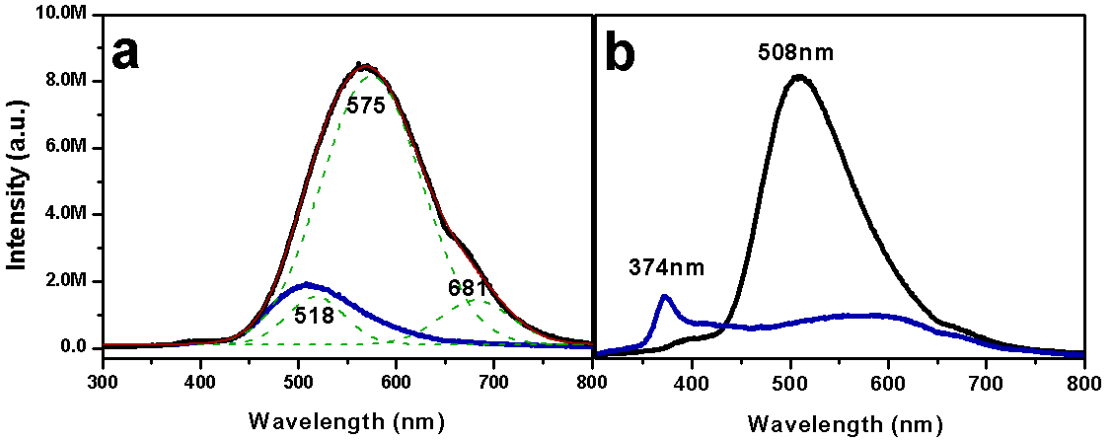

Figure 9. PL spectra with excitation source of 250 nm Xe lamp on the ZnO deposited on polycrystalline Pt as deposited (black) and after calcination at 700 ^{o}C for 1 hour (blue). (a) is the ZnO deposited from a deposition solution containing 0.25 M NaOH and 6 mM ZnO, (b) is the ZnO deposited from a deposition solution containing 0.25 M NH_4OH and 6 mM ZnO.

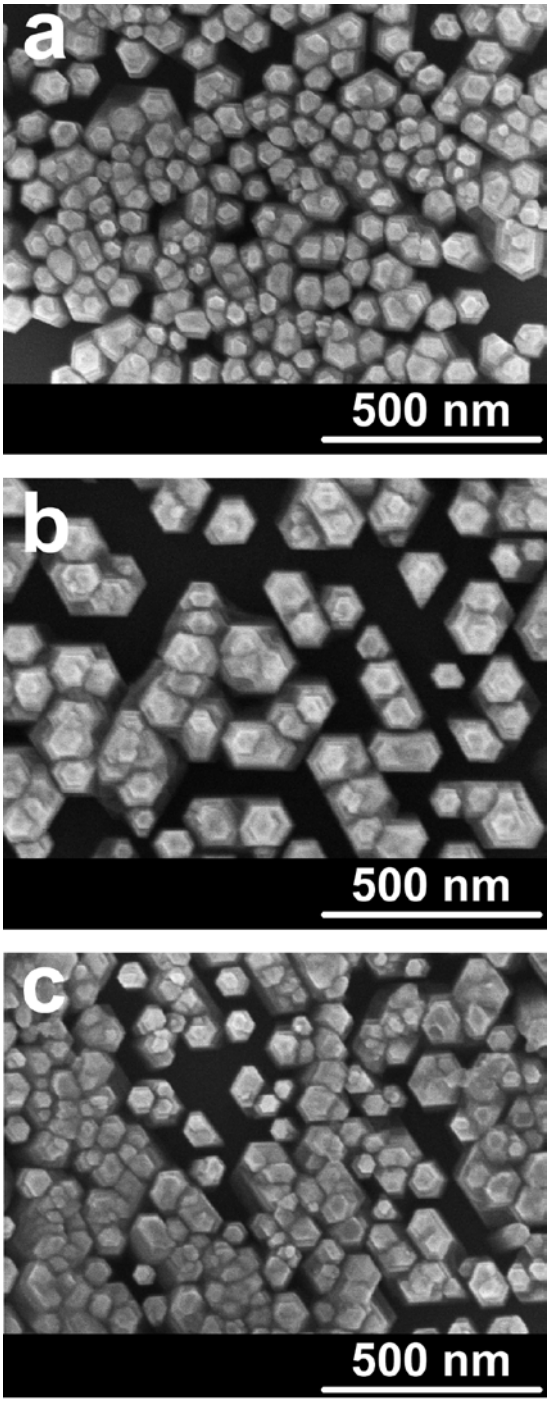

Figure 10. SEM images of the epitaxial ZnO deposited on single crystal substrates of Au(100) (a), Au(110) (b) and Au(111) (c).

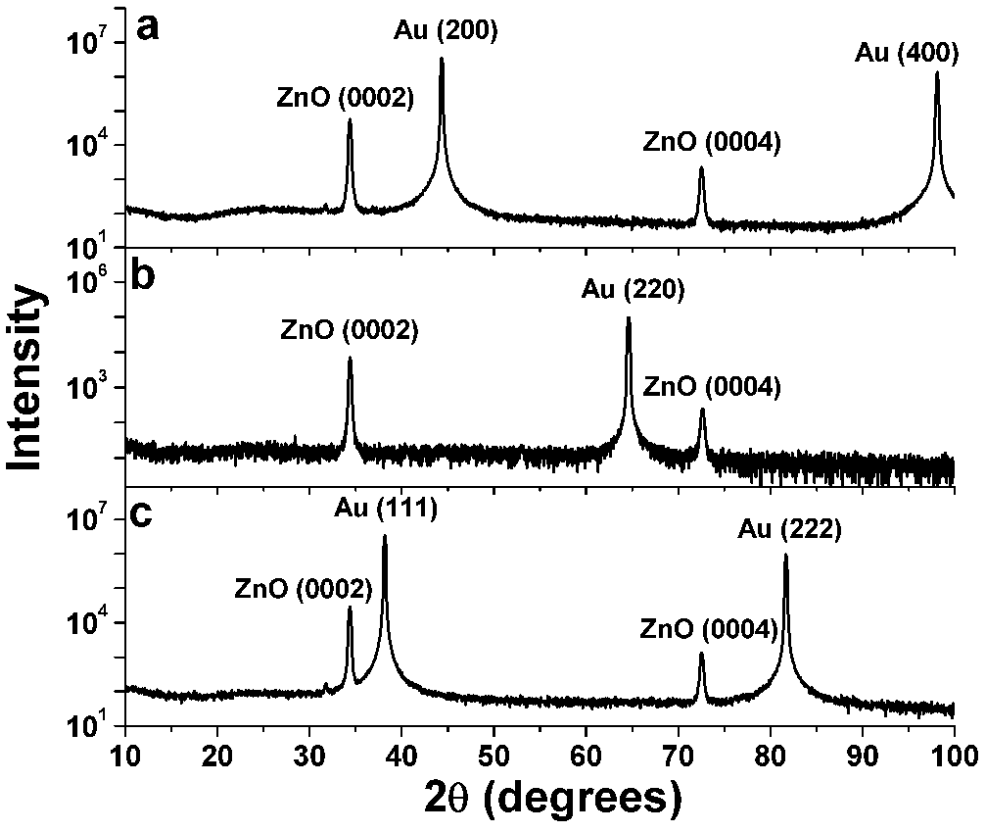

Figure 11. X-ray symmetric θ-2θ scans on the epitaxial ZnO deposited on the single crystal substrates of Au(100) (a), Au(110) (b) and Au(111) (c).

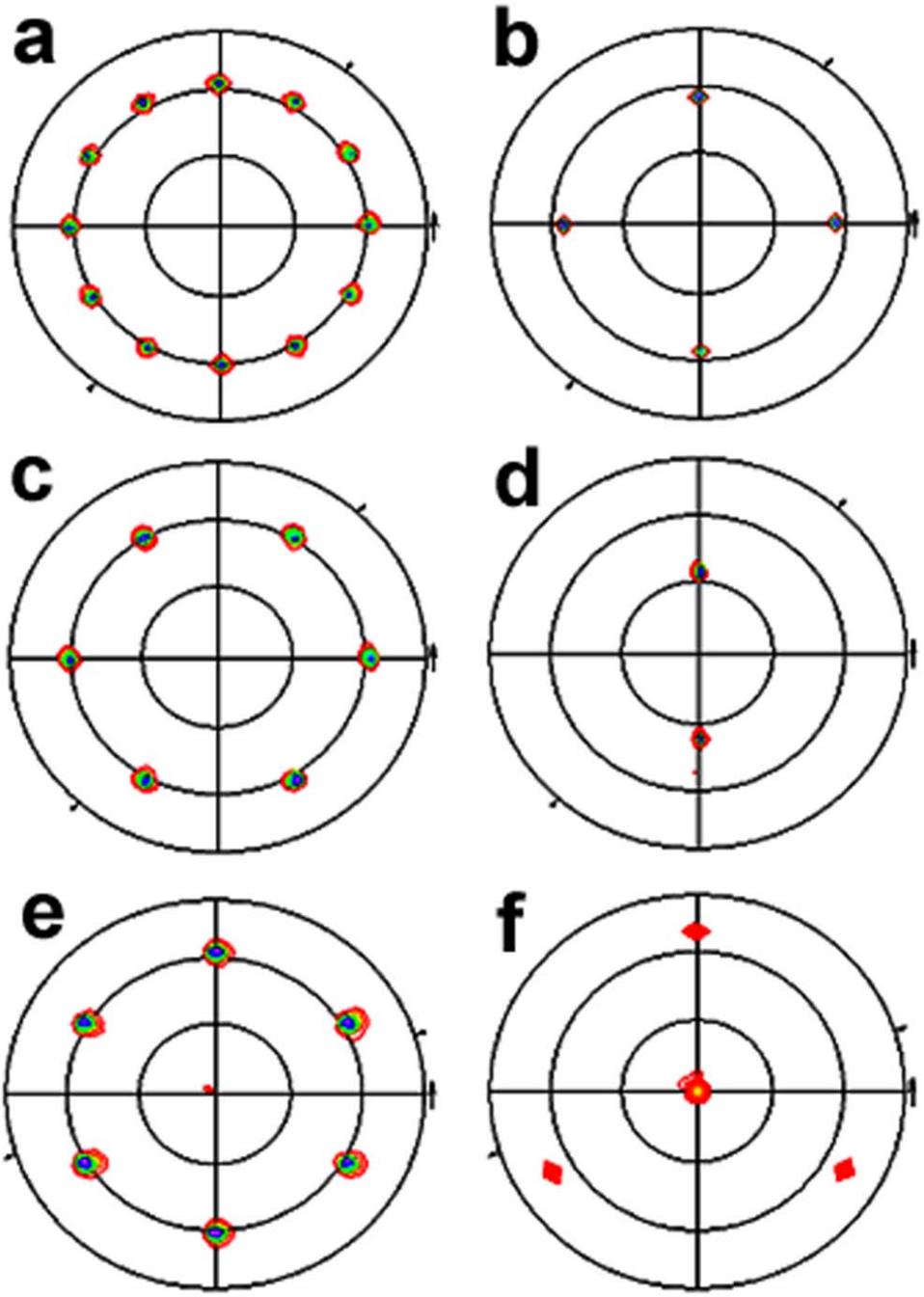

Figure 12. ZnO $(10\bar{1}1)$ pole figures on the ZnO deposited on the single crystal substrates of Au(100) (a), Au(110) (c) and Au(111) (e), as well as the corresponding Au(111) substrate pole figures for Au (100) (b), Au(110) (d) and Au(111) (f) substrates. The radial grid lines on each pole figure correspond to 30^{o} increments in χ.

III: Electrodeposition of Epitaxial Cuprous Iodide Thin Films on Au(100) Single Crystals

*Guojun Mu, Rakesh V. Gudavarthy, Eric W. Bohannan, and Jay A. Switzer**

Department of Chemistry and Graduate Center for Materials Research, Missouri University of Science and Technology, Rolla, MO 65409

* To whom correspondence should be addressed, e-mail: jswitzer@mst.edu

ABSTRACT

Epitaxial γ-CuI thin films were electrodeposited onto Au(100) single crystals from a slightly acidic Cu(II)-EDTA-KI solution (pH = 3) at 50 ^{o}C. The generation of CuI could occur at more negative potentials than predicated from the linear sweep voltammogram, which is believed due to a chemical oxidation of electrochemically deposited Cu metal by I_2 in the solution. XRD shows that the films deposited at potentials of -0.1, -0.2, and -0.3 V versus Ag/AgCl are all pure CuI, whereas the one deposited at -0.4 V is a mixture of Cu and CuI. The PL spectra of these films show a sharp free-exciton emission peak of CuI at 409 nm, along with a weak bound-exciton emission at 413 nm and broad a red emission at 680 nm due to the crystal defect. Epitaxial CuI films were deposited on Au(100) single crystals. The epitaxial relationships for the four CuI domains on Au(100) are $CuI(111)[2\bar{1}\bar{1}]$ //Au(100)[001], $CuI(111)[2\bar{1}\bar{1}]$ //Au(100)[010], $CuI(111)[2\bar{1}\bar{1}]$ //$Au(100)[00\bar{1}]$, and $CuI(111)[2\bar{1}\bar{1}]$ //$Au(100)[0\bar{1}0]$. That is, the CuI(111)

planes and Au(100) planes are parallel and the CuI$[2\bar{1}\bar{1}]$and Au<010> in-plane directions are coincident.

KEYWORDS: electrodeposition, epitaxy, cuprous iodide, Au (100) single crystal

INTRODUCTION

Below the melting temperature of 873 K, cuprous iodide (CuI) crystal has three phases. The high temperature α phase (stable at above 680 K) has distorted face-centered cubic. The β phase that only exists in a narrow temperature range of 642-680 K has hexagonal wurtzite.[1] Both α phase and β phase CuI are superionic conductors with Cu^+ ions being the mobile species,[2-4] which conductivity level is comparable to those of liquid electrolytes.[5] Whereas the low temperature γ phase is of ordered face-centered cubic zincblende structure. It is one of the few p-type semiconductors with wide band-gap of 3.1 eV and exciton binding energy of 62 meV.[6] The γ phase CuI obtains increasing attention in recent years. It has been used in the dye-sensitized solid-state solar cells serving as the electrolyte layer to provide much higher hole mobilities than molecular solids or polymers, which comes from the stoichiometric excess of iodide.[7-9] In addition, it is one of the inorganic scintillation crystal materials with ultrafast scintillation property at a decay time of about 90 ps under room temperature.[10]

Many methods have been developed to synthesize this material, including pulsed laser deposition,[11] hydrothermal deposition,[12] and vacuum evaporation method.[13] Electrodeposition is a low-cost solution phase approach, where the substrate (working electrode) provides a template for the growth of deposits. The morphology and crystal structures of the deposits can be controlled by varying temperature or deposition

potential. Penner and coworkers have applied a hybrid electrochemical/chemical method to deposit CuI on sapphire.[14] By using this method, the high temperature hexagonal β phase CuI was produced at room temperature on the hexagonal sapphire substrates. More recently, H. Kang et al. [15] has shown a simple electrodeposition method to generate γ-CuI on ITO glass substrates from a slightly acidic Cu(II)-EDTA-KI solution (pH = 3) at low temperatures (25 - 90 ^{o}C). An electrochemical-chemical mechanism is proposed for CuI deposition, as described Equations 1 & 2. The Cu(II) ion is first electrochemically reduced into Cu(I), followed by a chemical reaction of the produced Cu(I) cation with the I^- anion in the solution to form CuI.

$$Cu(EDTA)^{2+}(aq) + e^- \rightarrow Cu^+(aq) + EDTA(aq) \quad (1)$$

$$Cu^+(aq) + I^-(aq) \rightarrow CuI(s) \quad (2)$$

In this case, the chemical reaction in Equation 2 happens spontaneously ($\Delta_r G^o$ = -67.9 kJ/mol). The generation of CuI should be favored comparing to that of Cu_2O, because it has a more negative free energy ($\Delta_r G^o$ = -8.9 kJ/mol) than the latter one.

Herein, using this electrodeposition method, we show that epitaxial thin films of γ-CuI can be produced on the surface of Au(100) single crystal. Additionally, the effect of deposition potentials on the film composition and photoluminescence is studied on Au coated microscope slide substrates. This simple electrodeposition method may also be applied in producing other epitaxial thin films of cuprous halides or silver halides on the surface of electric conductive single crystal substrates.

EXPERIMENTAL SECTION

CuI was electrochemically deposited using the method developed by H. Kang et al.[15] The deposition solution was prepared by dissolving 1 g of copper (II) sulfate

pentahydrate, 0.66 g of potassium iodide, and 1.49 g of ethylenediaminetetraacetic acid disolium into 200 mL water, resulting a deposition solution of pH 3, containing 20 mM Cu(II), 20 mM I^-, and 20 mM EDTA. All the chemicals were ACS grade and purchased from Sigma-Aldrich. The water was produced in lab by a Millipore system (18 MΩ-cm). A three-electrode cell was used for deposition, consisting of a Pt counter electrode and an Ag/AgCl (KCl sat'd) reference electrode. The substrate on that CuI was deposited, including gold coated microscope slides and Au(100) single crystal, served as the working electrode. Gold coated microscope slides (1000 Å Au coating) were purchased from Sigma-Aldrich and were sonicated in a 1:1 water-ethanol solution then rinsed thoroughly with water before use. Au(100) single crystal was purchased from Monocrystals Company (purity 99.99+%, diameter 10 mm, thickness 2 mm). For pretreatment, the gold single crystal was first rinsed with ethanol thoroughly, and then electrochemically polished by applying an anodic current of 1.6 A/cm^2 with a graphite counter electrode for 30 seconds in a solution containing 2:1:1 ethanol, ethylene glycol, and HCl. After electro-polishing, the crystal was rinsed thoroughly with ethanol and water. Polycrystalline CuI films on Au-glasses were deposited at 50 ^oC by applying potentials from -0.1 V to -0.4 V versus Ag/AgCl to a total charge density of 1 C/cm^2. The epitaxial CuI films on Au(100) were deposited at 50 ^oC by applying a potential of -0.2 V versus Ag/AgCl to a total charge density of 0.1 and 0.5 C/cm^2.

For characterization, a Hitachi S-4700 field-emission scanning electron microscope was used to observe the morphology of the films. X-ray diffraction symmetric scans were used to identify the polycrystalline films on Au-glasses and to determine the out-of-plan orientations of the epitaxial films on Au(100). XRD symmetric

scans were run from 2θ values of 10^o to 120^o with a high-resolution Philips X'Pert MRD diffractometer using Cu Kα source radiation with a combination X-ray mirror and two-crystal Ge(220) two-bounce hybrid monochromator (PW3147/00) as the incident beam module and a 0.18 parallel plate collimator (PW3098/18) as the diffracted beam module. The in-plane orientations of the epitaxial films relative to the Au substrates were determined by X-ray pole figures. Pole figures were collected on the same instrument in point-focus mode using a crossed-slit collimator (PW3084/62) as the primary optics and a flat graphite monochromator (PW3121/00) as the secondary optics. To perform the pole figure analysis, the 2θ was set to the angle of the CuI(311) plane ($2\theta = 49.96^o$) for the film analyses and to the angle of the Au(111) plane ($2\theta = 38.18^o$) for the substrate analyses. The sample was moved through a sequence of tilt angles (χ) from 0^o to 90^o, and at each χ, the sample was rotated azimuthally (φ) from 0^o to 360^o. Data were collected in the continuous mode over 3^o intervals for both χ and φ, with a count time of 5 s/point. PL spectra were collected on the CuI samples deposited on Au-glasses using a Fluorolog-3 spectrofluorometer (Horiba-Yvon, Edison, NJ, USA) with a Xe lamp as excitation source and a front-face emission configuration. The Xe lamp spectrum and a water Raman spectrum were used to calibrate the excitation and the emission gratings. All measurements were taken at room temperature under identical settings: 320 nm excitation wavelength, 385 nm long-pass filter, 5 nm excitation slit width, 1 nm emission slit width, 1.0 seconds integration time, and1.0 nm step size.

RESULTS AND DISCUSSION

Figure 1 shows the linear sweep voltammograms on a polycrystalline Au electrode with area of 0.02 cm^2 in the unstirred EDTA-KI bath (blue dots) and Cu(II)-EDTA-KI deposition solution (black solid line) at 50 ^oC. The linear sweeps were scanned from the open circuit potential (OCP) to -0.8 V versus Ag/AgCl at a scan rate of 50 mV/s. The linear sweep voltammogram in the EDTA-KI solution (blue dots) shows that EDTA and KI is electrochemically inert within the scanning range and that the electrochemical generation of hydrogen gas starts around -0.5 V versus Ag/AgCl. The reduction of Cu(II)-EDTA-KI solution (black solid line) to produce Cu metal begins around -0.1 V versus Ag/AgCl. The initial stage of the linear sweep in Cu(II)-EDTA-KI solution is shown in the inserted figure, indicating that the reduction of Cu(II) to Cu^+ occurs from OCP to -0.1V, which is consistent with the situation in a basic Cu(II) solution. The electrochemically reduced Cu^+ ions further react with I^- to generate CuI deposit. According to Figure 1, CuI can only be deposited in the potential range from OCP to -0.1 V versus Ag/AgCl, and at more negative potentials Cu metal should be produced. During the deposition process, however, the CuI white films could be deposited at -0.1, -0.2 and -0.3 V versus Ag/AgCl, a film mixed with Cu and CuI was deposited at -0.4 V versus Ag/AgCl, and red films of Cu were deposited at more negative potentials. The generation of CuI at more negative potentials than predicated from the linear sweep voltammogram can be explained by a chemical oxidation of electrochemically deposited Cu metal by I_2 in the solution. The iodine (I_2) is produced on the counter electrode as a result of anodic oxidation of I^- ions during the deposition, which is indicated by the gradual change in coloration of the deposition solution from

blue to greenish color. By immersing a Cu foil in this greenish solution, surface of the Cu foil is immediately covered by a white film that is verified by X-ray diffraction to be a polycrystalline CuI layer. This reaction is described by Equation 3. Oxidation of Cu metal in contact with I_2 solutions was reported elsewhere[16] and was used for deposition of CuI microcrystals from ethanol solutions that contain I_2.[17]

$$2Cu(s) + I_2(aq) \rightarrow 2CuI(s) \quad (3)$$

Figure 2 is the X-ray diffraction symmetric scans of the films deposited on Au coated microscope slides at -0.1, -0.2, -0.3, and -0.4 V versus Ag/AgCl. All these films were deposited in a stirred solution at 50 ^{o}C to a charge density of 1 C/cm^2. The films deposited at potentials of -0.1V (Figure 2a), -0.2 V (Figure 2b), and -0.3 V (Figure 2c) versus Ag/AgCl are CuI crystals (JCPDS # 6-246). From the relative peak intensities, no preferred orientation is observed for the CuI grown on the polycrystalline Au substrates that have a preferred orientation of (111). At deposition potential of -0.4 V versus Ag/AgCl (Figure 2d), the deposit is a mixture of CuI and Cu (JCPDS # 4-836). SEM images of the polycrystalline CuI films deposited on Au-glass substrates at -0.1, -0.2, -0.3, and -0.4 V versus Ag/AgCl are shown in Figure 3. The surface morphologies of these films are highly faceted with triangle shape, dense yet not completely covered. These films are randomly aligned with no preferred orientations. The crystal size decreases when the deposition potential becomes more negative. At -0.4 V, large crystal grains of Cu is mixed with smaller CuI crystals.

Figure 4 shows the photoluminescence (PL) spectra of these films. All spectra were acquired at room temperature using excitation energy of 320 nm (3.91 eV). The intensity of the emission spectra is normalized according to the height of the free-exciton emission peaks at 409 nm (3.06 eV), which is in the range from 4×10^5 to 8×10^5 a.u.

varied with the film density. The energy of the maximum emission peak is not shifted with the deposition potential, whereas the shape of the peak is not symmetric. The shoulder at 413 nm (3.03 eV) is assigned to the bound-exciton emission,[18] which relative intensity becomes higher with more negative deposition potentials. The broad red emission at around 680 nm (1.84 eV) is assigned to the donor-acceptor pair recombination.[18] The real intensity of the free-exciton emission peak for the film deposited at -0.4 V is 2×10^4 a.u., much lower than those of the other films, since this film is only partially composed with CuI. Whereas, the donor-acceptor pair recombination increases dramatically for the film deposited at -0.4 V, since at this potential impurity of Cu metal is likely induced into the CuI film.

For epitaxial study, the films were deposited on Au (100) single crystal at -0.2 V versus Ag/AgCl to charge density 0.1 and 0.5 C/cm^2. To determine the out-of-plane orientation of the epitaxial films, X-ray Bragg-Brentano θ-2θ scans were used, as shown in Figure 5. The XRD patterns of the films deposited at 0.1 C/cm^2 (Figure 5a) and 0.5 C/cm^2 (Figure 5b) exhibit the CuI(111) family peaks only, revealing a strong preferred orientation of (111) for the CuI films grown on Au(100) single crystal.

The in-plane orientations of the films were determined by X-ray pole figures. The CuI pole figures were acquired by selecting the CuI (311) plane to probe ($2\theta = 49.96^o$) and measuring the diffracted intensity as a function of the sample tilt (χ) and rotation angle (φ). While measuring, the sample is titled from $\chi = 0\text{-}90^o$ and for each tilt angle the sample is rotated azimuthally of $\varphi = 0\text{-}360^o$. Peaks occur in the pole figure when Bragg condition is satisfied. Polycrystalline films would produce featureless pole figures, films with a fiber texture would show rings in the pole figures, whereas epitaxial films exhibit

spots in the pole figures. The radial grid lines in the pole figures correspond to a 30^o increments in χ. Figure 6a is the (311) pole figure of the CuI that was deposited to a charge density of 0.1 C/cm^2. The pole figure presents 12 equally spaced ($\Delta\varphi = 30^o$) spots at $\chi = 29^o$, 12 equally spaced spots at $\chi = 59^o$, and 12 equally spaced spots at $\chi = 80^o$. This pole figure is in agreement with the calculated angles ($\chi = 29.5^o$, 58.5^o, and 80.0^o) between {311} planes and (111) plane in a cubic system. Figure 6b is the (311) pole figure of the CuI that was deposited to a charge density of 0.5 C/cm^2, revealing a weak (511) orientation besides the predominant (111) orientation. The presence of (511) is difficult to verify by examining an X-ray diffraction pattern, since the (333) and (511) planes have the same d-spacing, whereas pole figure provides clear indications of the presence of the (511) orientation. When running a (311) pole figure, the (311)-type reflections relative to the (511) orientation at $\chi = 9.5^o$, 29.5^o, 41.0^o, 58.5^o, 66.0^o, 80.0^o, and 86.7^o. The (111) substrate pole figure for Au(100) single crystal is shown in Figure 6c, consisting of 4 spots at $\chi = 54.7^o$, which correspond to the angle between the {111} planes and the (100) plane in the cubic crystal.

To verify the assignment of the in-plane orientations for the pole figures, stereographic projections were constructed using CaRIne Crystallography software (Version 3.1). Figure 7a and c show the CuI(111) and (511) stereographic projections respectively, probing CuI(311) type reflections. Similar to pole figures, the radial grid lines in the stereographic projections correspond to a 30^o increments in χ. In Figure 7a, three equally spaced ($\Delta\varphi = 120^o$) spots at $\chi = 29.5^o$, six equally spaced ($\Delta\varphi = 60^o$) spots at $\chi = 58.5^o$, and three equally spaced ($\Delta\varphi = 120^o$) spots at $\chi = 80.0^o$ correspond to one set of (311)-type reflections of the (111) orientation. Since the Au(100) substrate has four-fold

symmetry, it is reasonable to expect four domains of the CuI crystal to deposit on the surface rotating by 90^o to each other. The resulting stereographic projection in Figure 7b is consistent with the pole figure in Figure 6a. In Figure 7c, one spot at $\chi = 9.5^o$ and 41.0^o, and two spots at χ = 29.5^o, 58.5^o, 66.0^o, 80.0^o, and 86.7^o respectively correspond to one set of the (311)-type reflections relative to the (511) orientation. The pole figure in Figure 6b is consistent of 12 domains of (511) orientation. The number of domains of (511) orientation was determined using the number of spots at $\chi = 41.0^o$, since a single domain of (511) has one peak at this angle. The two perpendicular in-plane directions for the (511) orientation shown in Figure 6b are (511)[$2\bar{5}\bar{5}$] and (511)[$0\bar{1}1$]. The presence of (511) orientation is due to the twinning of the {111} planes with the stacking of (111) atoms not following the fcc sequence of ABCABC…... Similar kind of twinning was previously observed in electrochemically deposited magnetite films.

The epitaxial relationships for the four CuI domains on Au(100) are CuI $(111)[2\bar{1}\bar{1}]$ //Au(100)[001], CuI $(111)[2\bar{1}\bar{1}]$ //Au(100)[010], CuI$(111)[2\bar{1}\bar{1}]$//Au$(100)[00\bar{1}]$, and CuI$(111)[2\bar{1}\bar{1}]$//Au$(100)[0\bar{1}0]$. That is, the CuI(111) planes and Au(100) planes are parallel and the CuI$[2\bar{1}\bar{1}]$ and Au<010> in-plane directions are coincident. The SEM images of the epitaxial CuI films deposited on Au (100) single crystal to charge density 0.1 and 0.5 C/cm^2 are shown in Figure 8a and b respectively. The surface morphologies of the film deposited to 0.1 C/cm^2 (Figure 9a) are highly faceted yet not dense, whereas the one deposited to 0.5 C/cm^2 (Figure 9b) are highly faceted and dense. Both SEM images are consistent with the pole figures.

CONCLUSIONS

An electrodeposition method[15] is used here to deposit γ-CuI thin films on to Au coated microscope slides from a slightly acidic Cu(II)-EDTA-KI solution (pH = 3) at 50 ^{o}C. CuI is deposited with a electrochemical-chemical mechanism that Cu(II) ions are first electrochemically reduced into Cu(I) and then the produced Cu(I) ions spontaneously react with I^- in the solution to form CuI. During deposition, it is found that the generation of CuI at more negative potentials than predicated from the linear sweep voltammogram, which is believed due to a chemical oxidation of electrochemically deposited Cu metal by I_2 in the solution. The iodine (I_2) is produced on the counter electrode as a result of anodic oxidation of I^- ions during the deposition, which is indicated by the gradual change in coloration of the deposition solution from blue to greenish color.XRD shows that the films deposited at potentials of -0.1, -0.2, -0.3, and -0.4 V versus Ag/AgCl are all pure CuI, whereas the one deposited at -0.4 Vis a mixture of Cu and CuI. The PL spectra of these films show that the CuI deposited exhibit a sharp free-exciton emission peak at 409 nm, and a weak bound-exciton emission peak at 413 nm and broad red emission at 680 nm due to the crystal defect. The epitaxial CuI film was deposited on the surface of Au(100) single crystal. The epitaxial relationships for the four CuI domains on Au(100) are $CuI\,(111)[\bar{2}\bar{1}\bar{1}]$ //Au(100)[001], $CuI\,(111)[\bar{2}\bar{1}\bar{1}]$ //Au(100)[010], $CuI(111)[\bar{2}\bar{1}\bar{1}]//Au(100)[00\bar{1}]$, and $CuI(111)[\bar{2}\bar{1}\bar{1}]//Au(100)[0\bar{1}0]$. That is, the CuI(111) planes and Au(100) planes are parallel and the CuI$[\bar{2}\bar{1}\bar{1}]$ and Au<010> in-plane directions are coincident.

ACKNOWLEDGEMENTS. This work was supported by the U.S. Department of Energy, Office of Basic Energy Sciences under Grant No. DE-FG02-08ER46518.

REFERENCES

1. Shan, Yu; Li, Guangwu; Tian, Guang; Han, Jingzhi; Wang, Changsheng; Liu, Shunquan; Du, Honglin; Yang, Yingchang. "Description of the phase transitions of cuprous iodide." *J. Alloy. Compd.* (2009), 477(1-2), 403-406.

2. Darlington, C. N. W. "Atomic vibrations in cuprous iodide." *J. Phys. C Solid State* (1986), 19(26), 5095-102.

3. Zheng-Johansson, J. X. M.; Ebbsjoe, I.; McGreevy, R. L. "A molecular dynamics study of ionic conduction in CuI. I. Derivation of the interionic potential from dynamic properties." *Solid State Ionics* (1995), 82(3,4), 115-22.

4. Zheng-Johansson, J. X. M.; McGreevy, R. L. "A molecular dynamics study of ionic conduction in CuI. II. Local ionic motion and conduction mechanisms." *Solid State Ionics* (1996), 83(1,2), 35-48.

5. Dhere, Sunetra L.; Latthe, Sanjay S.; Kappenstein, Charles; Mukherjee, S. K.; Rao, A. Venkateswara. "Comparative studies on p-type CuI grown on glass and copper substrate by SILAR method." *Appl. Surf. Sci.* (2010), 256(12), 3967-3971.

6. Ichida, H.; Kanematsu, Y.; Shimomura, T.; Mizoguchi, K.; Kim, D.; Nakayama, M. "Photoluminescence dynamics of exciton-exciton scattering processes in CuI thin films." *Phys. Rev. B* (2005), 72(4), 045210/1-045210/5.

7. Rusop, Mohamad; Shirata, Tetsuya; Sirimanne, Prasad M.; Soga, Tetsuo; Jimbo, Takashi. "Properties of pulsed-laser-deposited CuI and characteristics of constructed dye-sensitized TiO2|Dye|CuI solid-state photovoltaic solar cells." *Jpn. J. Appl. Phys.* (2003), 42(8), 4966-4972.

8. Kumara, G. R. A.; Kaneko, S.; Okuya, M.; Tennakone, K. "Fabrication of Dye-Sensitized Solar Cells Using Triethylamine Hydrothiocyanate as a CuI Crystal Growth Inhibitor." *Langmuir* (2002), 18(26), 10493-10495.

9. Rusop, M.; Soga, T.; Jimbo, T.; Umeno, M. "Copper iodide thin films as a p-type electrical conductivity in dye-sensitized p-CuI|Dye|n-TiO2 heterojunction solid state solar cells." *Surf. Rev. Lett.* (2004), 11(6), 577-583.

10. Gao, Pan; Gu, Mu; Liu, Xiao-Lin; Liu, Bo; Huang, Shi-Ming. “X-ray excited luminescence of cuprous iodide single crystals: On the nature of red luminescence.” *Appl. Phys. Lett.* (2009), 95(22), 221904/1-221904/3.

11. Sirimanne, P. M.; Rusop, M.; Shirata, T.; Soga, T.; Jimbo, T. “Characterization of transparent conducting CuI thin films prepared by pulse laser deposition technique.” *Chem. Phys. Lett.* (2002), 366(5,6), 485-489.

12. Zheng, Zhi; Liu, Airuo; Wang, Shumin; Huang, Baojun; Wong, Ka Wai; Zhang, Xitian; Hark, Siu Kong; Lau, Woon Ming. “Growth of highly oriented (110) -CuI film with sharp exciton band.” *J. Mater. Chem.* (2008), 18(8), 852-854.

13. Kim, D.; Nakayama, M.; Kojima, O.; Tanaka, I.; Ichida, H.; Nakanishi, T.; Nishimura, H. “Thermal-strain-induced splitting of heavy- and light-hole exciton energies in CuI thin films grown by vacuum evaporation.” *Phys. Rev. B* (1999), 60(19), 13879-13884.

14. Hsiao, G. S.; Anderson, M. G.; Gorer, S.; Harris, D.; Penner, R. M. “Hybrid Electrochemical/Chemical Synthesis of Supported, Luminescent Semiconductor Nanocrystallites with Size Selectivity: Copper(I) Iodide.” *J. Am. Chem. Soc.* (1997), 119(6), 1439-1448.

15. Kang, H.; Liu, R.; Chen, K.; Zheng, Y.; Xu, Z. “Electrodeposition and Optical Properties of Highly Oriented CuI Thin Films” *Electrochem. Acta*, 2010 XX, XX

16. Gana, R.; Figueroa, M.; Arancibia, V.; Baeza, M. “Electrochemical production of cuprous iodide using the anode-support system.” *Hydrometallurgy* (1999), 51(1), 87-95.

17. Li, Xin; Wan, Meixiang. “Morphology and Hydrophobicity of Micro/Nanoscaled Cuprous Iodide Crystal.” *Crystal Growth & Design* (2006), 6(12), 2661-2666.

18. Kondo, S.; Hata, Y.; Saito, T. “Extremely-high-intensity photoluminescence from CuBr films fabricated by film-substrate chemical reaction of CuCl films on KBr-crystal substrate.” *Mater. Lett.* (2008), 62(1), 33-36.

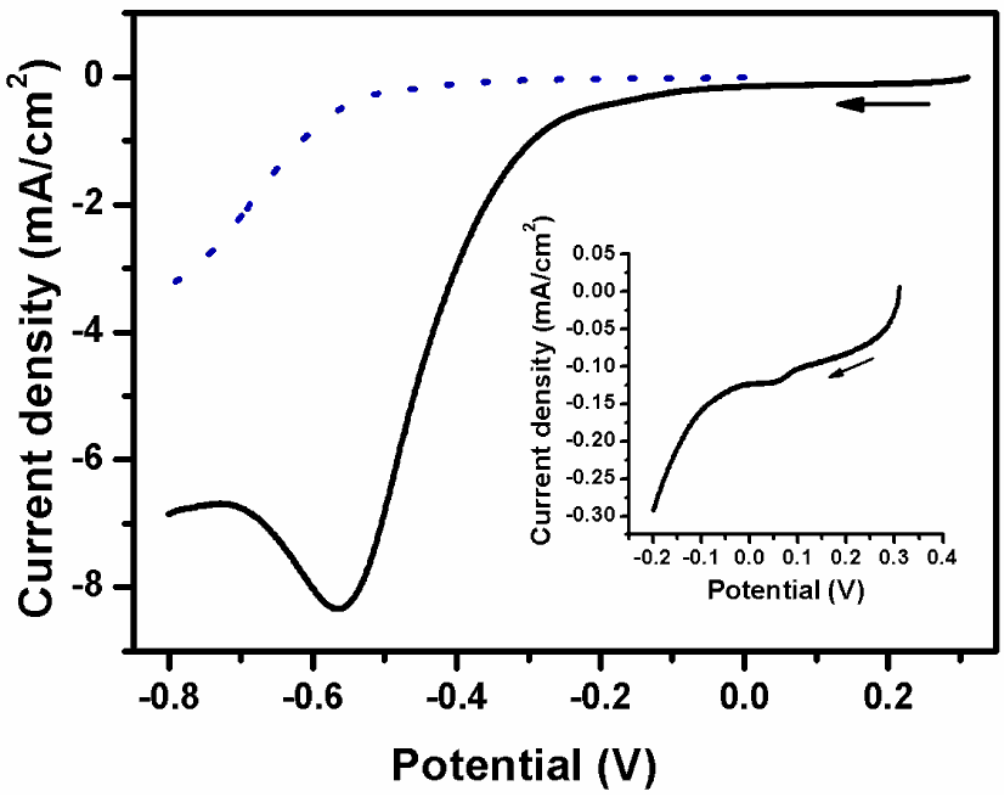

Figure 1. Linear sweep voltammograms on a polycrystalline Au electrode with area of 0.02 cm^2 in an unstirred EDTA-KI solution (blue dots) and Cu(II)-EDTA-KI deposition bath (black solid line) at 50 ^oC. The linear sweeps were scanned at 50 mV/s from their open circuit potentials (OCP) to -0.8 V versus Ag/AgCl (KCl sat'd) reference electrode. The insert graph is the initial stage of the linear sweep in Cu(II)-EDTA-KI solution (black line).

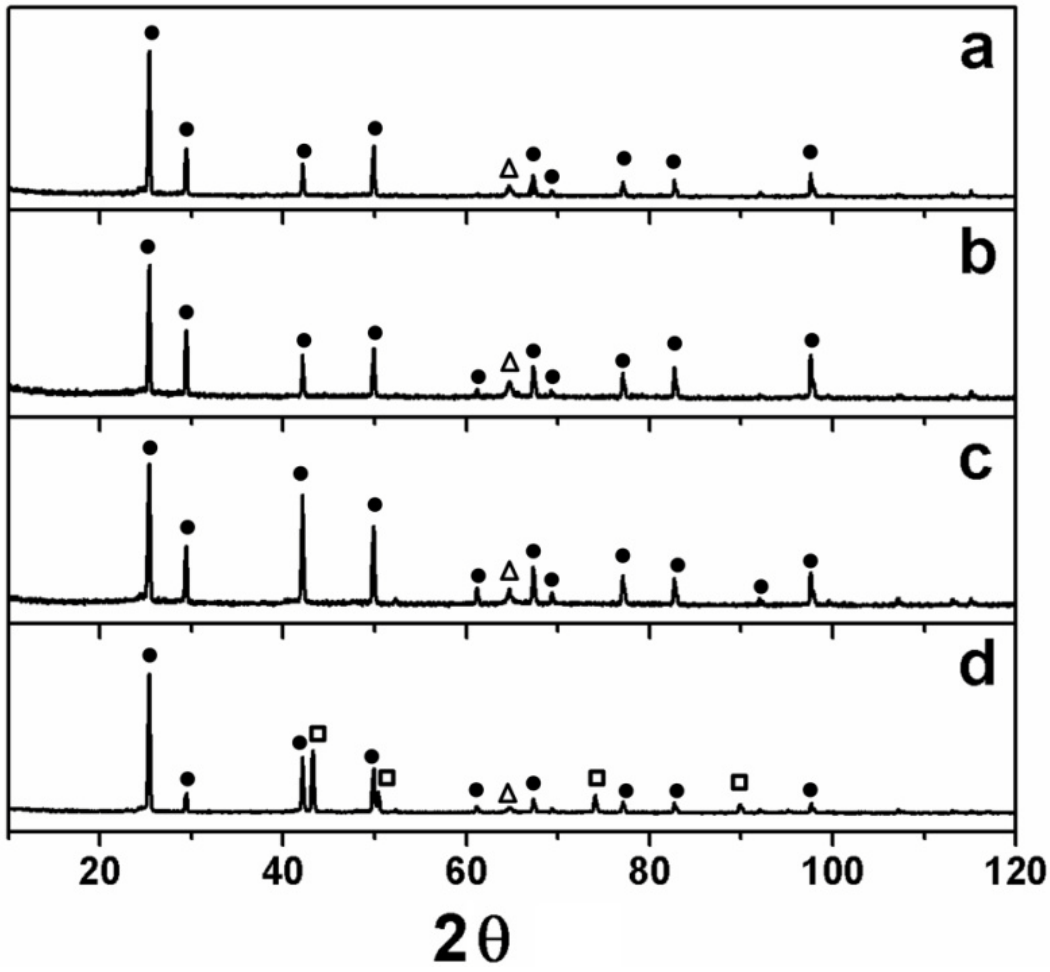

Figure 2. X-ray diffraction symmetric scans of the films deposited on Au coated microscope slides at -0.1V (a), -0.2 V (b), -0.3 V (c), and -0.4 V (d) versus Ag/AgCl. The solid circles represent the X-ray diffraction peaks for CuI, the hollow triangles represent the peaks for Au, and the hollow squares represent the peaks for Cu.

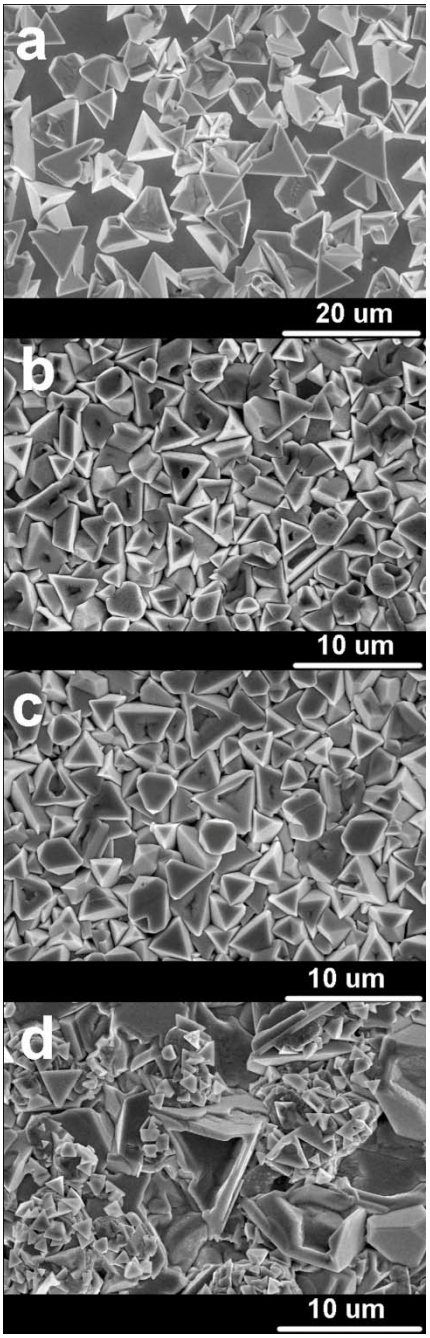

Figure 3. SEM images of the films deposited on Au-glasses at -0.1V (a), -0.2 V (b), -0.3 V (c), and -0.4 V (d) versus Ag/AgCl.

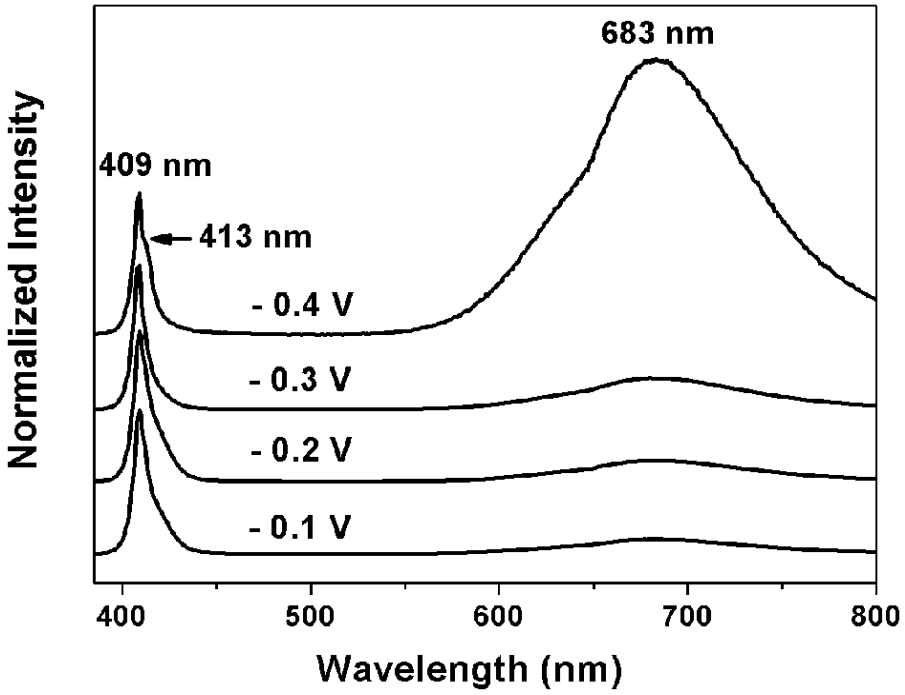

Figure 4. PL spectra of the films deposited on Au-glasses by applying deposition potentials of -0.1V, -0.2 V, -0.3 V, and -0.4 V versus Ag/AgCl. The intensity of each emission peak is normalized according to the maximum of the emission peak at 409 nm.

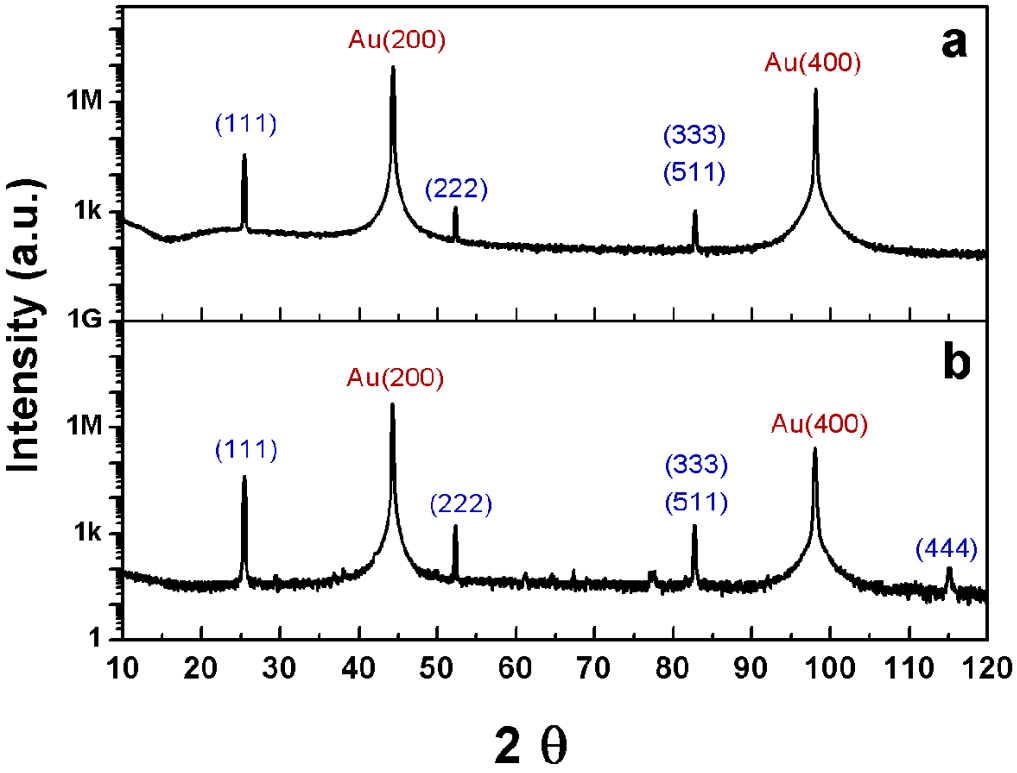

Figure 5. X-ray Bragg-Brentano θ-2θ scans on the epitaxial CuI films deposited on Au (100) single crystal at -0.2 V versus Ag/AgCl to charge density 0.1 C/cm^2 (a) and 0.5 C/cm^2 (b).

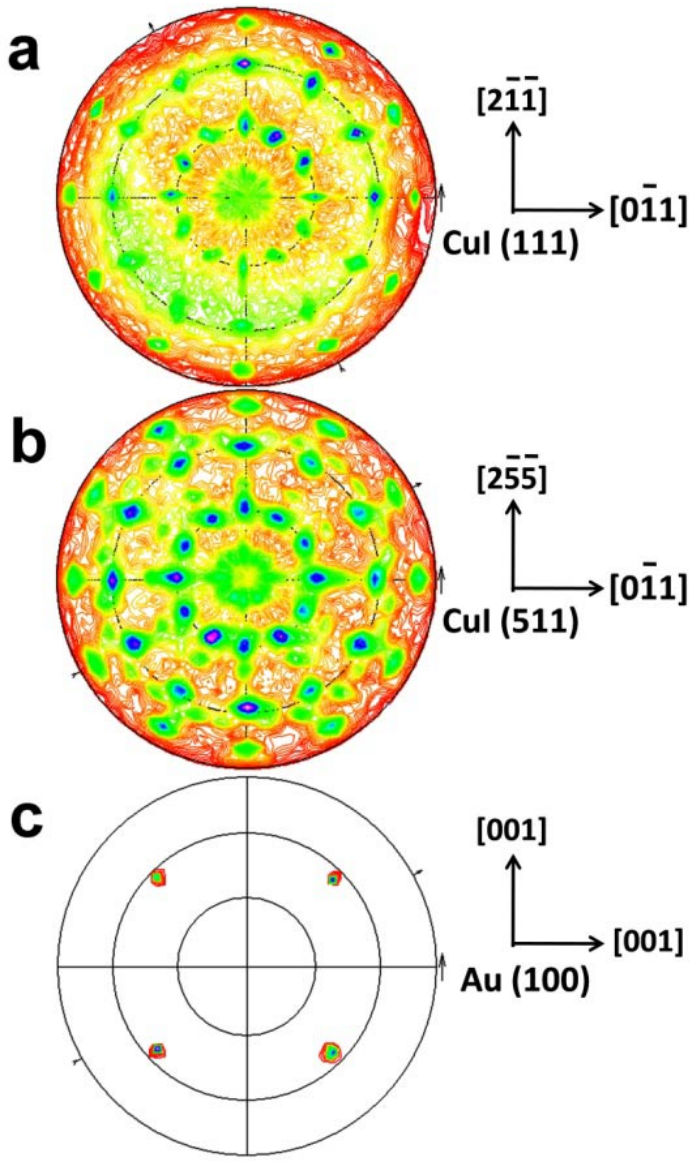

Figure 6. The CuI (311) pole figures of the epitaxial CuI films deposited to charge density 0.1 C/cm^2 (a) and 0.5 C/cm^2 (b), and the Au(111) substrate pole figure (c) of the Au(100) substrate.

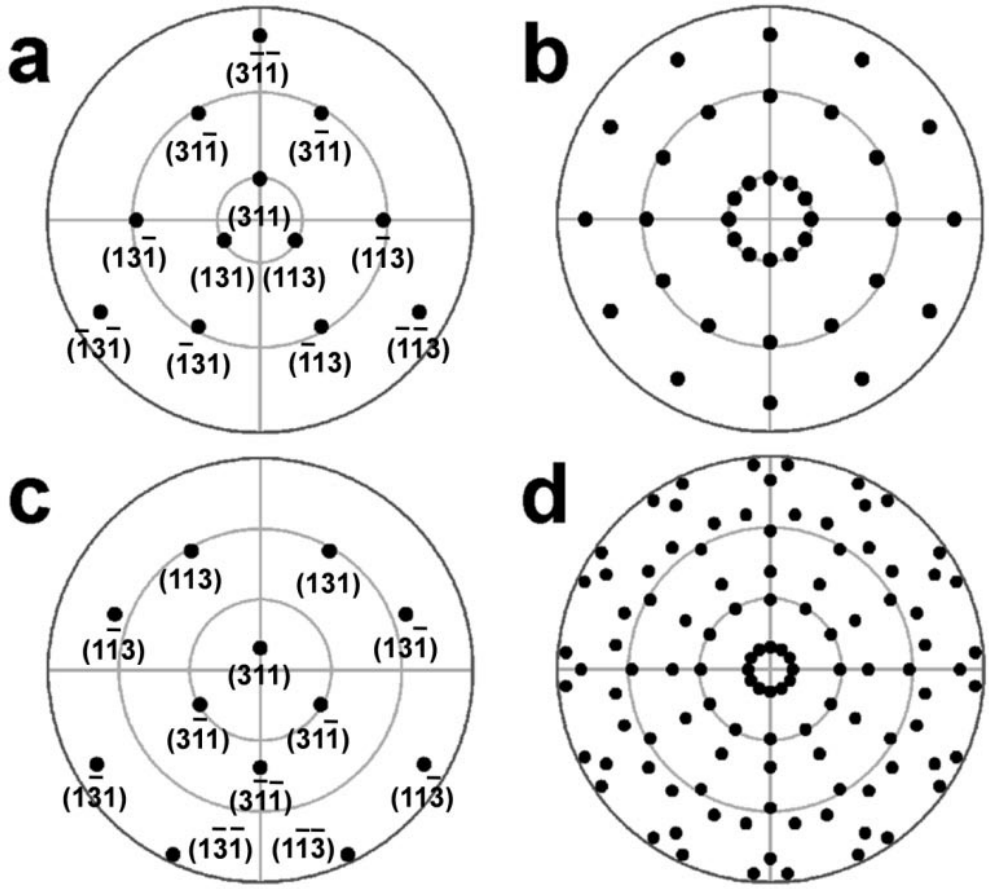

Figure 7. The (111) (a) and (511) (c) stereographic projections of CuI probing (311)-type reflections. Rotating (a) and (c) by 0^o, 90^o, 180^o, and 270^o and then overlaying the four rotating images results the stereographic projections in (b) and (d) respectively, which are consistent with the pole figures in Figure 6 (a) and (b).

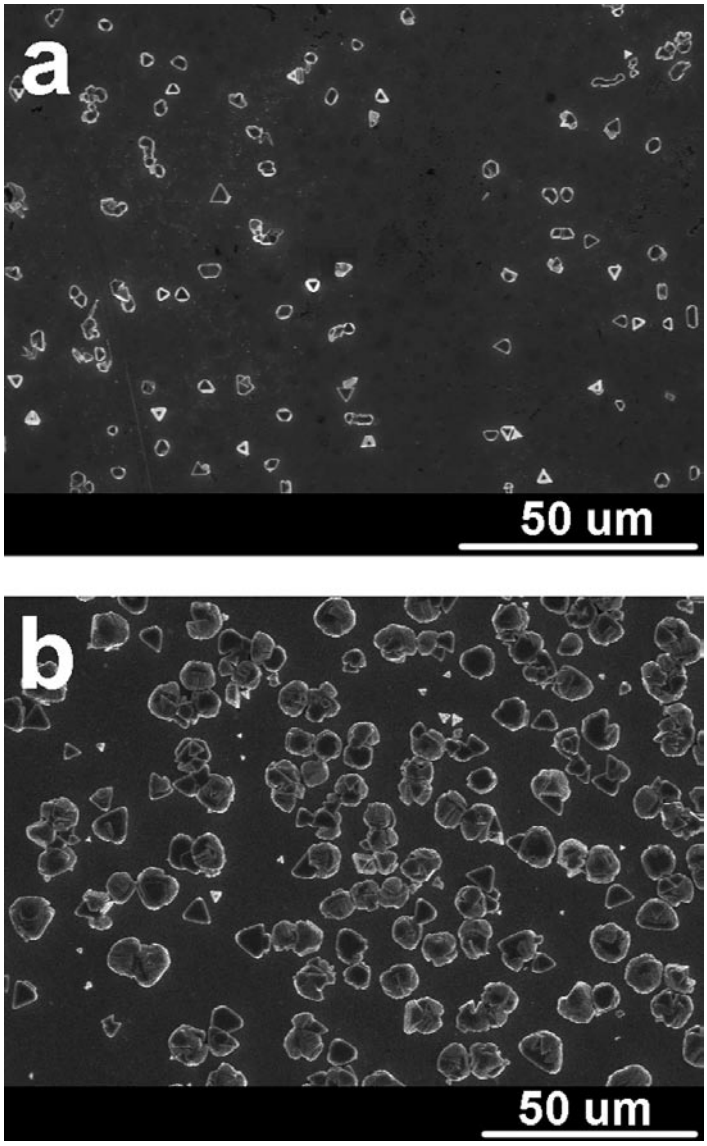

Figure 8. SEM images of the CuI films on Au(100) substrate to charge density 0.1 C/cm^2 (a) and 0.5 C/cm^2 (b).

APPENDIX A.

THERMODYNAMIC CALCULATIONS OF SATURATION AND SPECIATION OF ZINC(II) AQUEOUS SOLUTIONS

As an amphoteric material, ZnO dissolves in aqueous solutions since Zn(II) and hydroxide ions form complexes: $Zn(OH)_x^{x-4}$ (x = 0, 1, 2, 3, 4). Lincot and co-workers have studied the speciation distribution and solubility of ZnO in aqueous solutions at varied temperatures.[1,2] The calculations demonstrated here are based on their work. For calculation, crystalline ZnO(s) is considered to be the solid state compound, $Zn(OH)_x^{x-4}$, H_2O, OH^-, and H^+ are regarded as the aqueous species. The basic thermodynamic data for each compound are listed in Table A.1.

Table A.1. Standard thermodynamic data for Zn(II) aqueous solution at 25°C and 1 bar.

Species	$\Delta_f H^o$ (kJ/mol)	S^o (J/mol·K)	$\Delta_f G^o$ (kJ/mol)	$C_p{}^o(T)$			
				a (J/mol·K)	b (J/mol·K^2)	c (J·K/mol)	d (J/mol·K^3)
Zn^{2+} (aq)	-153.1	-109.9	-147.2	19327	-79748	-3374	92469
$Zn(OH)^+$ (aq)	-364.0	-62.8	-339.7	4481	-18292	-774	21214
$Zn(OH)_2$ (aq)	-327.6	-8.4	-282.1	17460	-72300	-3071	84490
$Zn(OH)_3^-$ (aq)	-595.7	-66.9	-463.2	2084	-8009	-323	8450
$Zn(OH)_4^{2-}$ (aq)	-552.7	-167.4	-390.3	32537	-134143	-5663	154874
ZnO (s)	-350.5	43.6	-320.4	47.0	3.0	-7.0	1.3
H_2O (l)	-285.8	70.0	-237.1	0	140	0	0
OH^- (aq)	-230.0	10.9	-157.1	40928	-169401	-7180	197089
H^+ (aq)	0	0	0	0	0	0	0

The Gibbs free energy of formation ($\Delta_f G^o_{(T)}$) was obtained as function of the absolute temperature (T) for each species using Equation 1:

$$\Delta_f G^o_{(T)} = \Delta_f G^o_{(298)} + \int_{298}^{T} C_p^o(T)d(T) - S^o_{298}(T-298) - T\int_{298}^{T} C_p^o(T)\frac{d(T)}{T} \quad (1)$$

where the $\Delta_f G^o_{(298)}$, S^o_{29} are standard Gibbs free energy of formation and standard entropy, respectively, and their values are shown in Table A.1. $C^o_p(T)$ is heat capacity, empirically determined by the Kelle'y equation (Equation 2).

$$C^o_p(T) = a + b\times10^{-3}T + c\times10^{5}T^{-2} + d\times10^{-6}T^{2} \quad (2)$$

where constants a, b, c, and d are varied for each material. The resulting $\Delta_f G^o_{(T)}$values from 30 to 90 ^{o}C are shown in Table A.2.

Table A.2. The values of Gibbs free energy of formation ($\Delta_f G^o_{(T)}$) for each species at temperatures from 30 to 90 ^{o}C.

Species	$\Delta_f G^o$ (kJ/mol)						
	25 ^{o}C	**40 ^{o}C**	**50 ^{o}C**	**60 ^{o}C**	**70 ^{o}C**	**80 ^{o}C**	**90 ^{o}C**
Zn^{2+} (aq)	-147.2	-145.5	-144.4	-143.3	-142.2	-141.1	-139.9
$Zn(OH)^{+}$ (aq)	-339.7	-340.7	-341.3	-342.0	-342.7	-343.4	-344.1
$Zn(OH)_2$ (aq)	-282.1	-282.0	-281.9	-281.7	-281.6	-281.5	-281.4
$Zn(OH)_3^{-}$ (aq)	-463.2	-462.2	-461.6	-461.0	-460.4	-459.9	-459.3
$Zn(OH)_4^{2-}$ (aq)	-390.3	-387.8	-386.1	-384.3	-382.6	-380.8	-379.0
ZnO (s)	-320.4	-321.0	-321.5	-322.0	-322.5	-323.0	-323.5
H_2O (l)	-237.1	-238.2	-238.9	-239.7	-240.4	-241.2	-242.0
OH^- (aq)	-157.2	-157.0	-156.8	-156.6	-156.3	-156.1	-155.8

Considering the equilibrium reaction in Equation 3, the accumulated stability constant (β) can be obtained from Gibbs free energy of reaction ($\Delta_r G^o_{(T)}$) of the corresponding reactions:

$$Zn^{2+} + xOH^- \Leftrightarrow Zn(OH)_x^{2-x} \qquad (x = 1, 2, 3, 4) \quad (3)$$

$$\beta = \frac{[Zn(OH)_x^{2-x}]}{[Zn^{2+}][OH^-]^x} \quad (4)$$

Table A.3. The values of equilibrium constants for each reaction at temperatures at 25 and 70 ^{o}C.

Equations	25 ^{o}C	70 ^{o}C
$Zn^{2+} + OH^- \Leftrightarrow Zn(OH)^+$	$\log(\beta_1) =$ 6.18	6.72
$Zn^{2+} + 2OH^- \Leftrightarrow Zn(OH)_2$	$\log(\beta_2) =$ 10.09	10.22
$Zn^{2+} + 3OH^- \Leftrightarrow Zn(OH)_3^-$	$\log(\beta_3) =$ 14.28	13.64
$Zn^{2+} + 4OH^- \Leftrightarrow Zn(OH)_4^{2-}$	$\log(\beta_4) =$ 15.50	14.59
$Zn^{2+} + 2OH^- \Leftrightarrow ZnO(s) + H_2O$	$\log(k_{sp,ZnO}) =$ -16.80	-16.44
$H^+ + OH^- \Leftrightarrow H_2O$	$\log(k_w) =$ -13.99	-12.81

The distribution fraction (α) of each zincate species and the overall solubility (S) were resolved as a function of the solution pH from Equations 5-10. Where, the accumulated stability constant (β) for the zincate anions and the solubility product (K_{sp}) for ZnO(s) and $Zn(OH)_2$(s) were obtained from the corresponding Gibbs free energy of reaction ($\Delta_r G^o_{(T)}$), as shown in Table A.1.

$$\alpha_{Zn^{2+}} = \frac{[Zn^{2+}]}{[Zn(II)]} \quad (5)$$

$$\alpha_{Zn(OH)^+} = \frac{[Zn(OH)^+]}{[Zn(II)]} = \frac{[Zn^{2+}]\beta_1[OH^-]}{[Zn(II)]} \quad (6)$$

$$\alpha_{Zn(OH)_2} = \frac{[Zn(OH)_2]}{[Zn(II)]} = \frac{[Zn^{2+}]\beta_2[OH^-]^2}{[Zn(II)]} \quad (7)$$

$$\alpha_{Zn(OH)_3^-} = \frac{[Zn(OH)_3^-]}{[Zn(II)]} = \frac{[Zn^{2+}]\beta_3[OH^-]^3}{[Zn(II)]} \quad (8)$$

$$\alpha_{Zn(OH)_4^{2-}} = \frac{[Zn(OH)_4^{2-}]}{[Zn(II)]} = \frac{[Zn^{2+}]\beta_4[OH^-]^4}{[Zn(II)]} \quad (9)$$

$$[Zn(II)] = [Zn^{2+}] + [Zn(OH)^+] + [Zn(OH)_2] + [Zn(OH)_3^-] + [Zn(OH)_4^{2-}] = [Zn^{2+}](1 + \beta_1[OH^-] + \beta_2[OH^-]^2 + \beta_3[OH^-]^3 + \beta_4[OH^-]^4) = \frac{K_{sp}}{[OH^-]^2}(1 + \beta_1[OH^-] + \beta_2[OH^-]^2 + \beta_3[OH^-]^3 + \beta_4[OH^-]^4) \quad (10)$$

The resulting speciation distributions and solubility diagrams of ZnO at 25 and 70 ^oC are shown in Figure A.1. Due to the change of K_w with temperature, the pH value of a solution containing 0.25 M NaOH at 25 ^oC is 13.4, and shifts to 12.2 when heated to 70 ^oC. As shown in Figure A.1, the saturated solution at 25 ^oC and pH 13.4 can dissolve ZnO to a maximum concentration of 6.5 mM (81.5% of $Zn(OH)_4^{2-}$ and 18.5% of $Zn(OH)_3^-$); whereas at 70 ^oC and pH 12.2 it dissolves 4.0 mM ZnO (68.4% of $Zn(OH)_4^{2-}$ and 31.6% of $Zn(OH)_3^-$). In practice, 20 mL of concentrated solution was added into 180 mL water that was maintained at a certain temperature to make a final deposition solution that contained 0.25 M NaOH and 8 mM $Zn(NO_3)_2$. Such a deposition solution was in the state of supersaturation at temperatures from 25 to 90 ^oC. Due to the sluggish nature of the precipitation, a couple of minutes later a ZnO thin film was deposited on the substrate surface accompanied with homogeneous precipitation of ZnO powders in the solution.

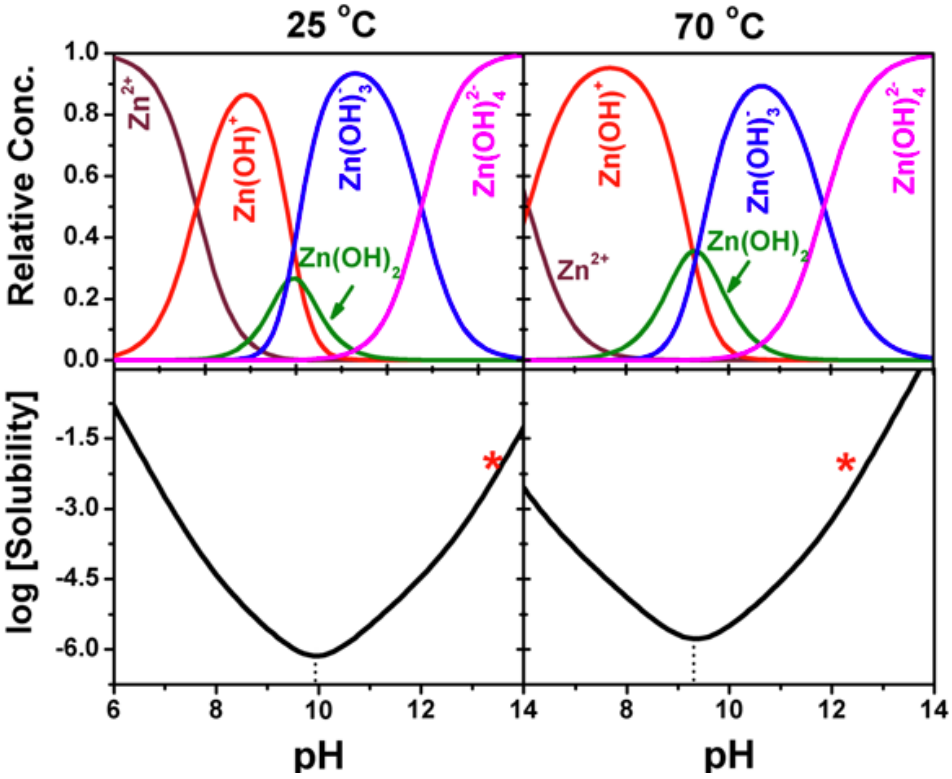

Figure A.1. Speciation distributions (upper) and solubility diagrams (lower) of Zn(II) versus pH in aqueous solution at 25 °C (left) and 70 °C (right). The asterisks represent the slightly oversaturated state of the deposition solution that contains 0.25 M NaOH and 8 mM $Zn(NO_3)_2$.

APPENDIX B.

SEM IMAGES OF ZINC OXIDE NANOSTRUCTURES DEPOSITED UNDER DIFFERENT CONDITIONS

In this section, the SEM images of ZnO nanostructures that are deposited under different conditions are discussed.

By using chemical bath deposition, from the solution containing Zn(II), citrate, and ammonia, the ZnO nanostructures that are different from the common nanocolumnar structures were obtained. The solution was made by diluting 3 mL of concentrated ammonia water (0.25 M) into 50 mL D.I. water, then adding 10 mM $Zn(NO_3)_2$ and 3 mM citric acid into the solution (final pH 11.5, clear). And then the solution was heated to 70 ^oC, and another 150 mL of D.I. water at 70 ^oC was mixed with the above solution. An Au coated microslide was placed in the solution immediately and the deposition process lasted for 30 minutes at 70 ^oC after precipitation formed. In Figure B.1, (a) is the ZnO nanostructures deposited on Au-glass substrate, (b) is the spherical ZnO powders collected from the same solution. Both film and powders were proven by X-ray diffraction to be ZnO. The ZnO thin film has a preferred out-of-plane orientation of (0001) on the polycrystalline substrate of Au that has a prepared orientation of (111), whereas the ZnO powder shows a random powder diffraction pattern.

ZnO is also grown on Cu_2O substrates. Figure B.2 shows SEM micrographs of the Cu_2O thin films electrodeposited on Au(100) (a), Au(110) (b), and Au(111) (c) single crystalline substrates from a solution containing 0.2 M $CuSO_4$, 0.2 M L(+)-tartaric acid, and 3 M NaOH. The electrodeposition of Cu_2O was conducted at a potential of -0.30V versus Ag/AgCl (with the open circuit potential of -0.177 V versus Ag/AgCl) with the solution stirred at 100 rpm at 30 ^oC for 360 seconds. Figure B.2 (d), (e), (f) show the ZnO nanospears deposited on the Cu_2O thin films on Au(100) (a), Au(110) (b), and Au(111)

(c), respectively. The ZnO was produced by chemical bath deposition from a solution containing 0.25 M NaOH and 8 mM $Zn(NO_3)_2$ at 70 ^oC for 15 minute.

Figure B.3 shows the ZnO deposited on Si(001) single crystals using different bases LiOH (a), NaOH (b), KOH (c), CsOH (d) by chemical bath deposition from the solutions contacting 0.25 M base and 8 mM $Zn(NO_3)_2$ at 70 ^oC for 15 minute. According to Figure B.3, the ZnO deposited using NaOH and KOH are epitaxial nanospears titled in four directions, while the ZnO deposited using CsOH remains the same morphology but with random arrangement, and the ZnO deposited using LiOH shows a totally different morphology.

By applying electrochemical deposition method, ZnO nanostructures can also be deposited from alkaline solutions. The electrolyte contains 0.25 M base, 5 mM $Zn(NO_3)_2$, and 10 mM amino acids. Figure B.4 shows the chemical structures of the six amino acids that were used to deposit ZnO from alkaline solutions: alanine, arginine, aspartic acid, serine, threonine, and valine. During deposition, the amino acid is electrochemically oxidized to generate protons, and lower the local pH in the vicinity of the working electrode. As a result, the ZnO is deposited on the surface of the electrode for excess of saturation state around the electrode. Cyclic voltammograms (CVs) are first acquired to determine the proper deposition potentials, as shown in Figure B.5. All the samples deposited using these six amino acids are proven by X-ray diffraction to be ZnO crystals with a preferred out-of-plane orientation of (0001), and the SEM images show that they have similar morphologies (see Figure B.6).

Figure B.7 shows two SEM images of ZnO electrochemically deposited on Au coated microscope slides from acidic solution that contain 0.1 M $Zn(NO_3)_2$ (top, left) and

from alkaline solution that contain 0.25 M NaOH and 8 mM $Zn(NO_3)_2$ (top, right). From the SEM images, the ZnO grown from acidic solution has a nanocolumnar structure, whereas the ZnO grown from alkaline solutions has an elongated nanospear structure with pyramidal top surfaces. The illustrations in Figure B.7 show that the ZnO nanocolumns have $(10\bar{1}0)$and (0001) facets and that the ZnO nanospears have $(10\bar{1}0)$and $(10\bar{1}1)$facets. The illustrations at lower part of Figure B.7 show that according to the crystal growth habit, the fastest growing planes grow out of existence, and the slowly growing planes remain. Therefore, from acidic solutions the fast growing planes of ZnO should be the $(10\bar{1}1)$planes, whereas from alkaline solutions the fast growing plane of ZnO should be the (0001) plane.

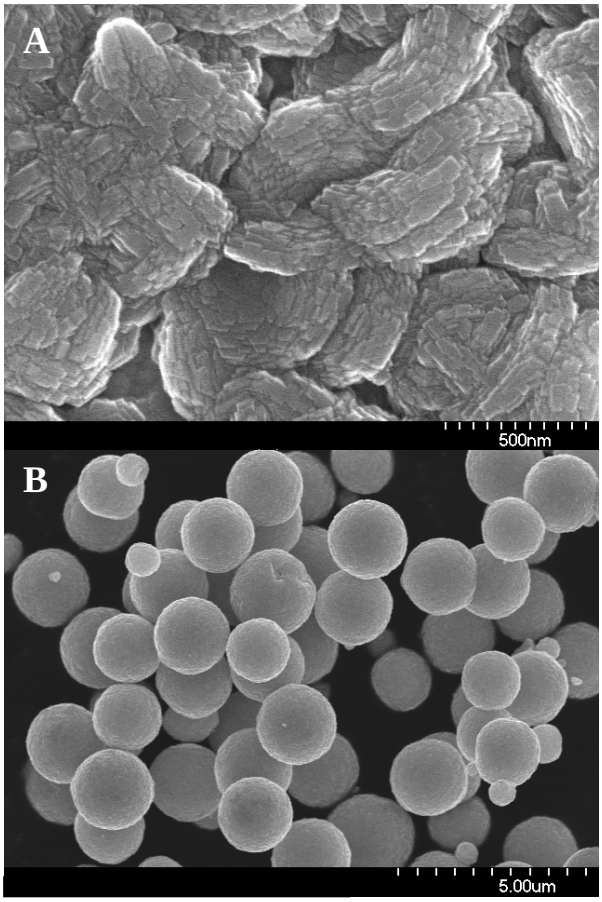

Figure B.1. ZnO thin films (a) deposited on Au-glass substrate and the ZnO powders collected from the solution (b) by chemical bath deposition from a solution containing Zn(II), citrate, and ammonia.

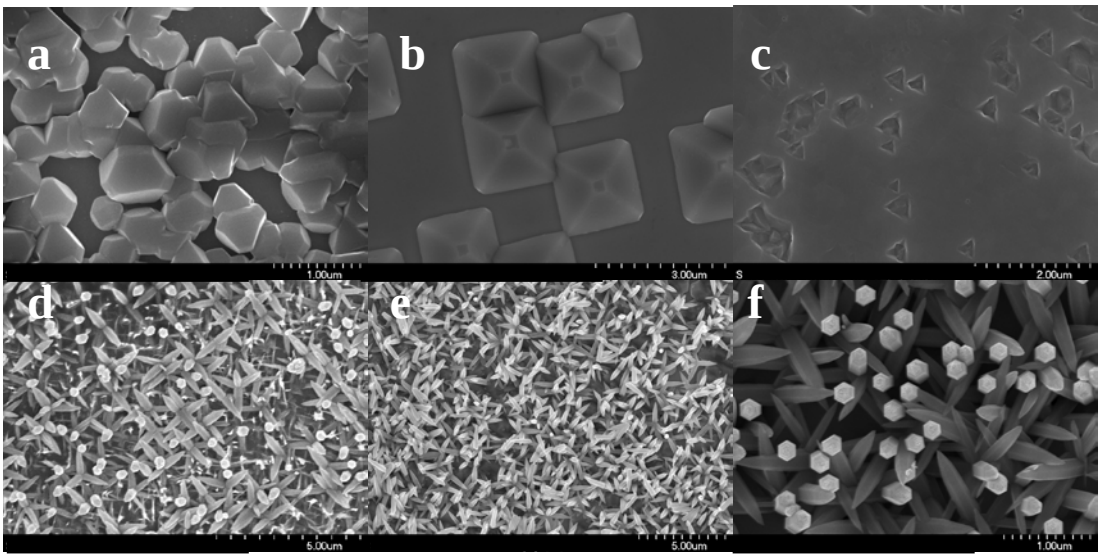

Figure B.2. Cu_2O thin films electrodeposited on Au(100) (a), Au(110) (b), and Au(111) (c) single crystalline substrates from a solution containing 0.2 M $CuSO_4$, 0.2 M L(+)-tartaric acid, 3 M NaOH, and ZnO nanospears (D, E, F) deposited on the corresponding Cu_2O thin films by chemical bath deposition from a solution containing $Zn(NO_3)_2$, and NaOH at 70 ^oC for 15 minute.

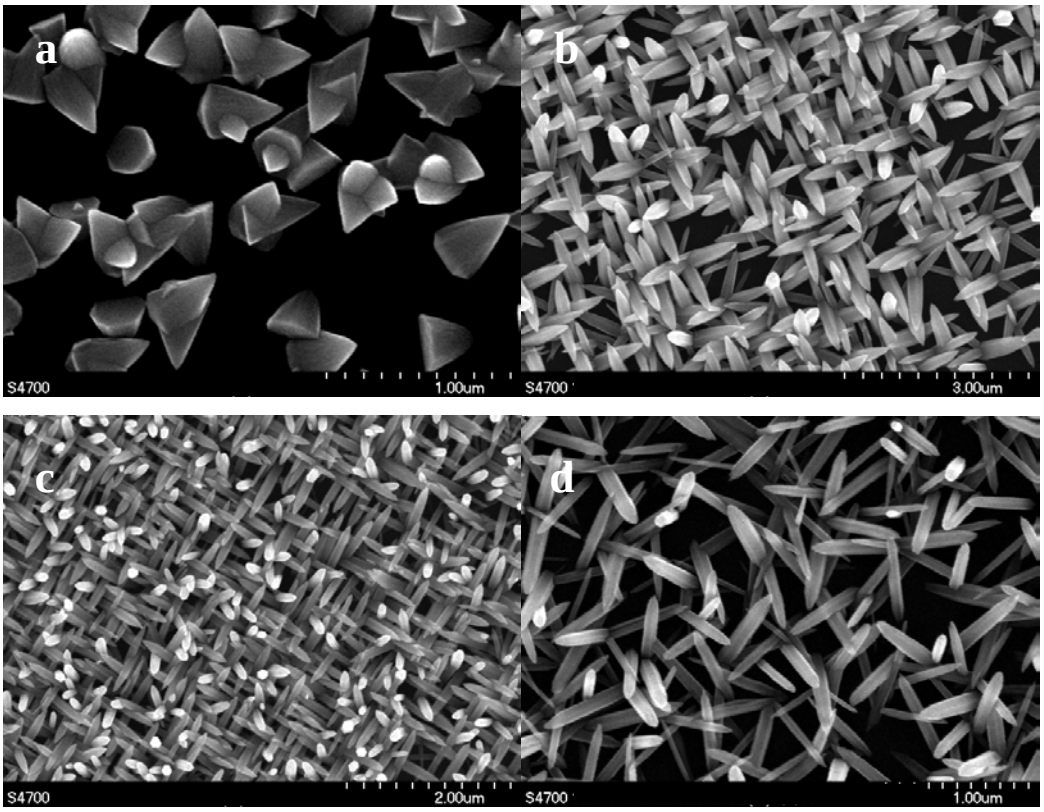

Figure B.3. ZnO chemically deposited on Si(001) substrates from solutions containing 0.25 M base and 8 mM $Zn(NO_3)_2$ at 70 ^oC for 15 minute using different bases (a) LiOH, (b) NaOH, (c) KOH, and (d) CsOH.

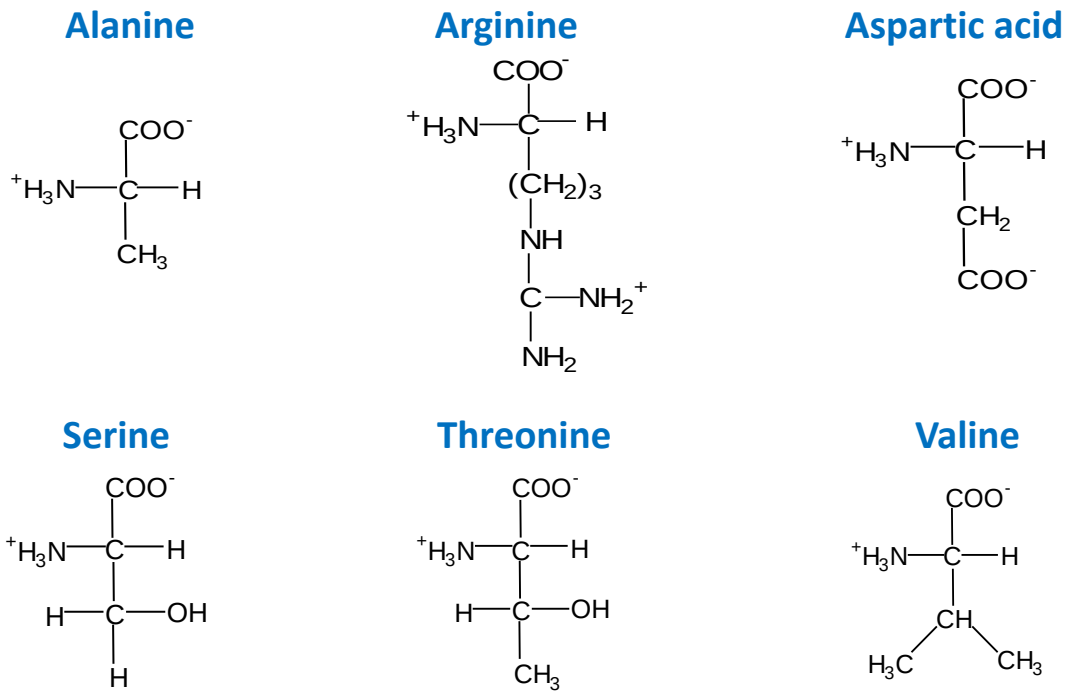

Figure B.4. Six different amino acids that can be used to be electroxidized to generate proton in the alkaline solutions for ZnO deposition: alanine, arginine, aspartic acid, serine, threonine, and valine.

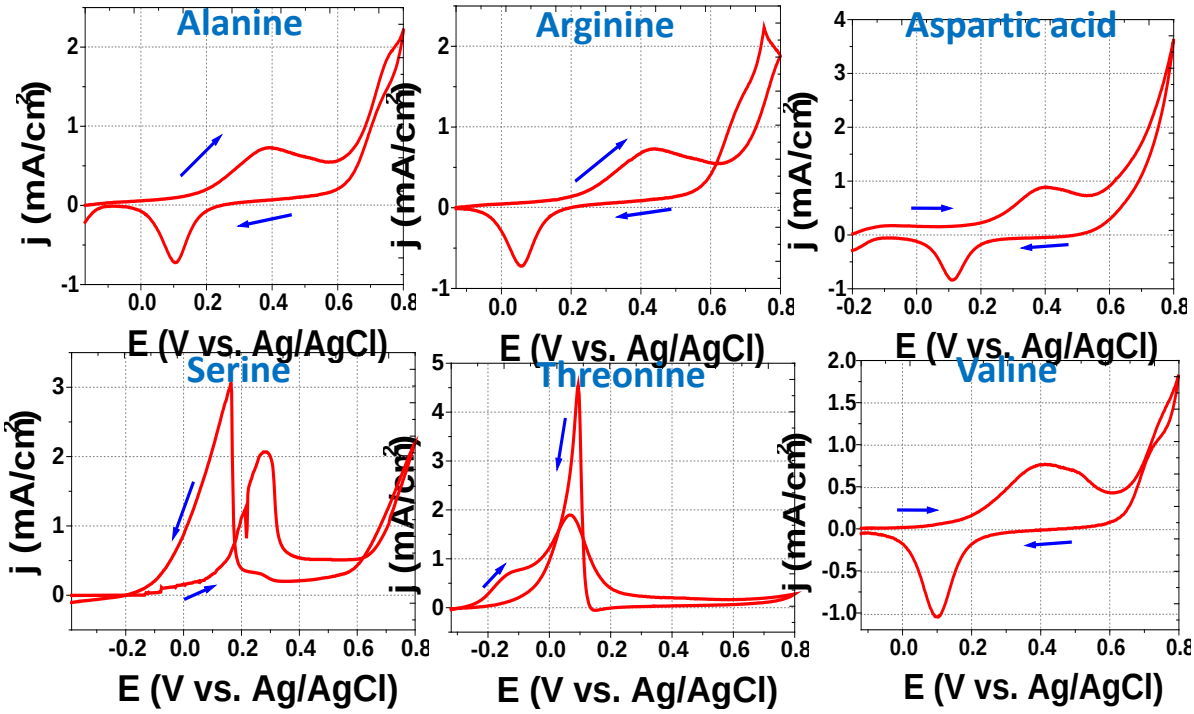

Figure B.5. Cyclic voltammetry (CV) analyses at 70 ^{o}C on the solutions containing 0.25 M base and 10 mM amino acids: alanine, arginine, aspartic acid, serine, threonine, and valine.

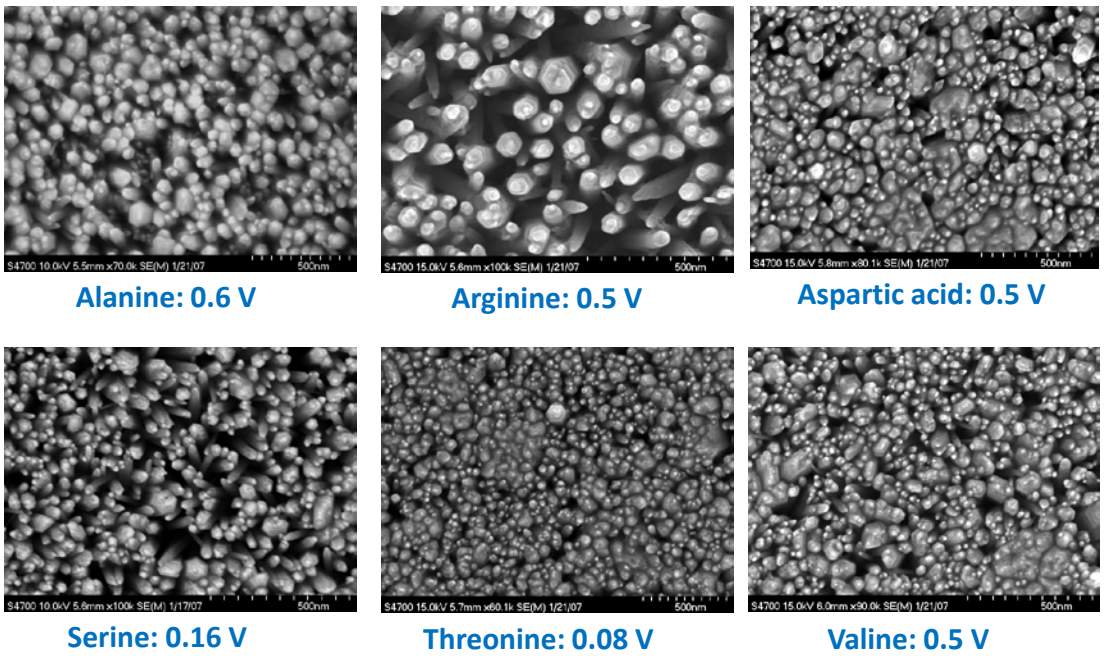

All the deposition potentials are refered to the Ag/AgCl (KCl saturated) reference electrode.

Figure B.6. SEM images of ZnO electrochemically deposited on Au coated microscope slides from solutions containing 0.25 M base, 5 mM $Zn(NO_3)_2$ and 10 mM amino acids (alanine, arginine, aspartic acid, serine, threonine, and valine) at 70 ^{o}C for 15 minute. The constant potential versus Ag/AgCl applied for deposition is as shown under each image.

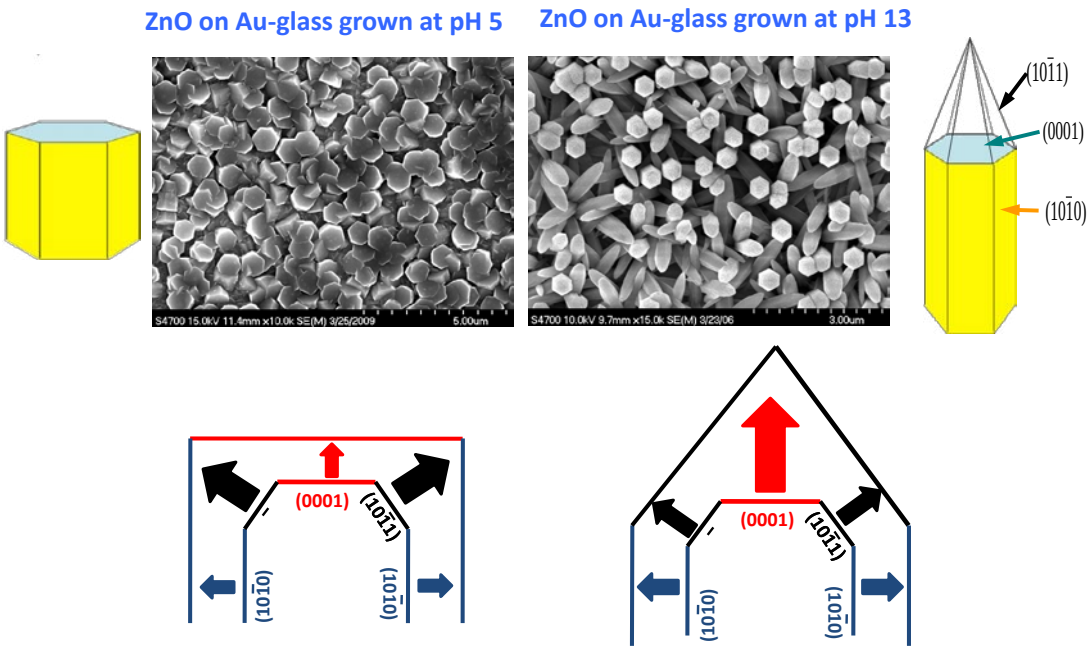

Figure B.7. SEM images of ZnO electrochemically deposited on Au coated microscope slides from acidic solution that contain 0.1 M $Zn(NO_3)_2$ (top, left) and from alkaline solution that contain 0.25 M NaOH and 8 mM $Zn(NO_3)_2$ (top, right), along with the illustrations showing the crystal growth habit.

APPENDIX C.

THERMAL TRANSFORMATION OF ELECTRODEPOSITED MAGNETITE AND FERRIHYDRITE INTO HEMATITE

In this section, the results of thermal transformations of electrodeposited magnetite (Fe_3O_4) thin films and ferrihydrite nanoribbons into ferric oxide including hematite and maghemite are discussed.

Figure C.1 shows the linear sweep voltammograms on a gold rotating disk electrode at rotating rate of 100 rpm in an alkaline TEA bath (blue squares) and the alkaline Fe(III)-TEA deposition bath (black solid line) at 80 ^{o}C. The linear sweep voltammograms are scanned from their open circuit potentials to -1.40 V versus Ag/AgCl at scan rate of 50 mV/s. The linear sweep voltammogram of 0.1M TEA in 2M NaOH (blue squares) shows that the alkaline TEA is electrochemically inactive and that the electrochemical generation of hydrogen gas begins around -1.25 V. Black films of magnetite are produced from -1.01 to -1.09 V. At more negative deposition potentials, the electrodeposited films are a Fe(II) rich compound: green rust. After air drying, they turn black and finally become ferrihydrite with the reddish brown color. When the potential becomes more negative than -1.23 V, a two-electron process occurs as the Fe(II) is reduced to Fe. Gray films of iron are produced at -1.3 V versus Ag/AgCl. The competing reaction of hydrogen evolution continues as the potential becomes more negative.

Figure C.2 shows the symmetric X-ray diffraction patterns of the magnetite film as deposited and after calcination in an O_2 atmosphere at 400 ^{o}C for 4 hours. The magnetite was deposited on single crystalline Au(111) substrate at -1.065 V versus Ag/AgCl until 1 C/cm^2 was passed. The film is estimated to be 2 μm thick. The XRD pattern in Figure C.2 shows that as deposited film is magnetite with strong (111) type reflection. After calcination, the film is primarily converted into hematite with (0001) out-of-plane orientation. One peak is also observed from maghemite (333) or (511)

reflection indicating that part of the film is thermally converted into the cubic ferrioxide maghemite. The hematite $(10\bar{1}4)$ pole figure in Figure C.3 contains 6 spots at 19°, 6 spots at 39°, and 6 spots at 54°. To understand the pole figures, the stereographic projection with hematite $(10\bar{1}4)$ type reflection is generated. With (0001) out-of-plane orientation (a), 6 spots are found at 38.24°. With $(11\bar{2}6)$ out-of-plane orientation (b), 2 spots are found at 19.66°, 2 are at 54.48°, another 2 are at 77.28°. The Figure (c) is the resulting stereographic projection by rotating the stereographic projection in (b) 120° and 240°, then overlaying each other. By comparing the pole figures and its stereographic projections, the hematite has two out-of-plane orientations, (0001) and $(10\bar{1}4)$. The (0001) orientation has one in-plane arrangement, whereas the $(10\bar{1}4)$ orientation has three in-plane configurations. Moreover, by comparing the film pole figure with the substrate pole figure, the epitaxial relationship of hematite and Au(111) can be determined.

Figure C.5 shows the symmetric X-ray diffraction patterns of the 200 nm thick magnetite film (by passing 0.1 C/cm^2 charge) as deposited and after calcination in an O_2 atmosphere at 400 °C for 4 hours. The XRD pattern shows that the film as deposited is magnetite with a strong (111) type reflection. After calcination, the peaks look similar to the as-deposited film. From the enlarged figure in Figure C.6, the shift of the peaks can be clearly observed. The annealed film is maghemite. Figure C.7 shows both $(10\bar{1}4)$ pole figure of hematite and the (311) pole figure of maghemite. Both layers are epitaxial. Figure C.8 is the SEM images for the annealed films with 200 nm and 2 um thickness. Figure C.9 is the Raman spectra of the film before and after annealing. For the thick film annealed at 400 °C, peaks are typical hematite scattering: 223 (A_{1g}), 291 (A_{1g}), 408 (E_g), 495 (A_{1g}), 609 (E_g), 814 (?), 1094 (?), and 1312 (2-magnon scattering) cm^{-1}. For the thin

film annealed at 400 ^{o}C and the as-deposited film, the peaks are similar, for the Raman scattering peak positions are determined by the crystal structure, and maghemite has similar structure with magnetite. The scattering peaks are at 296 (T_{2g}), 505 (E_{1g}), and 666 (A_{1g}) cm^{-1}. The Raman results are consistent with the XRD results.

A possible composition of maghemite and hematite when annealing an electrodeposited magnetite film is illustrated in Figure C.10. A possible explanation would be that when the thin film (200 nm) is annealed, the structure of ferrioxide layer is determined by the cubic structure of gold substrate, so the cubic maghemite is produced. Whereas when the film is thicker, only the lower part of the film follows the cubic structure; and the upper layer of the film turn into hexagonal hematite structure that is more thermodynamically stable. The $(11\bar{2}6)$ orientation of hematite is believed to come from the (511) twining of the precursor magnetite film.

Ferrihydrite is produced when the deposition potential is -1.10 to -1.20 V versus Ag/AgCl from the Fe(III)-TEA solution. Figure C.11 shows the EQCM study on the electrodeposition of ferrihydrite. The red line is the current recorded; the blue line represents the mass increase on the working electrode. The EQCM study shows that when the rate of mass increase is almost constant under the deposition condition, and the mass gain reaches a maximum of 5 mg on the electrode because the maximum of frequency is reached for the microbalance. Figure C.12 shows the photo images of the three samples deposited on Au coated microscope slides. The film is of green color immediately taken out from the deposition solution. Then it slowly changes color in air to be black and finally reddish. Figure C.13 shows the SEM images of the powders that are made by peeling off multiple electrodeposited ferrihydrite films from the Au-glass

substrate annealing in O_2 at 400 ^oC for 4 hours. The film shows a ribbon like morphology. Figure C.14 shows the SEM images of the electrodeposited ferrihydrite films on Au(110) substrate annealed. Figure C.14 (c) is the cross-section image of film deposited on Au-glass substrate. Figure C.15 shows the symmetric X-ray diffraction patterns of ferrihydrite films on Au(110) substrate before and after annealing. Only one peak is observed for each sample indicating that the film has a preferred out-of-plane orientation. The X-ray pole figures of the sample are in Figure C.16. Figure C.16 (a) is a ferrihydirte (110) pole figure, (b) is a hematite $(11\bar{2}0)$ pole figure. Only one broad spot at the center of the pole figure can be observed on each pole figure, which indicates that the in-plane alignment of the film is weak.

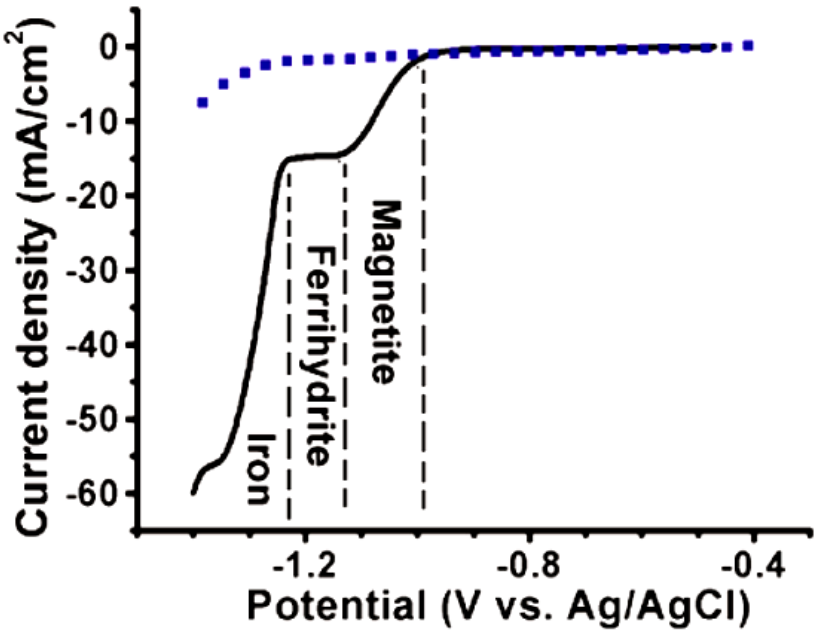

Figure C.1. Linear sweep voltammograms of an alkaline TEA solution (blue squares) and Fe(III)-TEA solution (black solid line) at 80 ^{o}C scanned at 50 mV/s at a rotation of 100 rpm on a gold rotating disk electrode. The alkaline TEA solution consisted of 0.1 M TEA in 2 M NaOH. The alkaline Fe(III)-TEA solution consisted of 43 mM Fe_2SO_4, 0.1M TEA, and 2M NaOH.

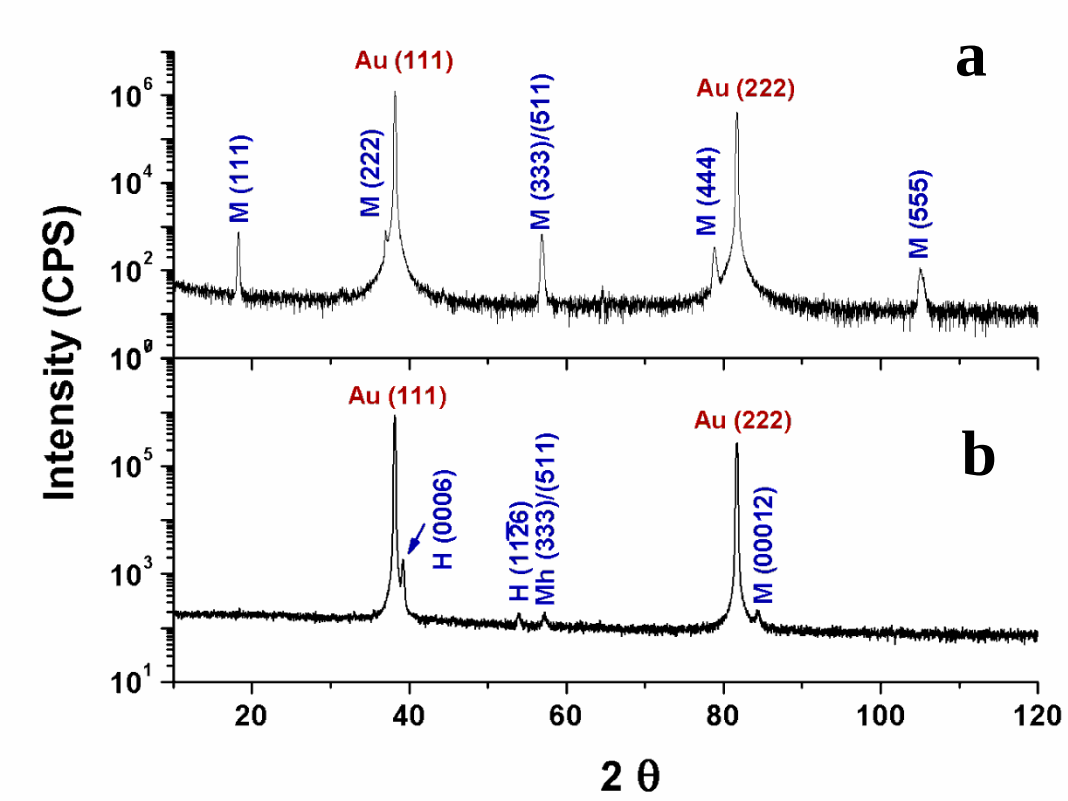

Figure C.2. Symmetric X-ray diffraction patterns of the magnetite film (Fe_3O_4) as deposited (a) and after calcination (a) in an O_2 atmosphere at 400 ^oC for 4 hours. The magnetite was deposited on single crystalline Au(111) substrate at -1.065 V versus Ag/AgCl until 1 C/cm^2 was passed. The film is estimated to be 2 μm thick.

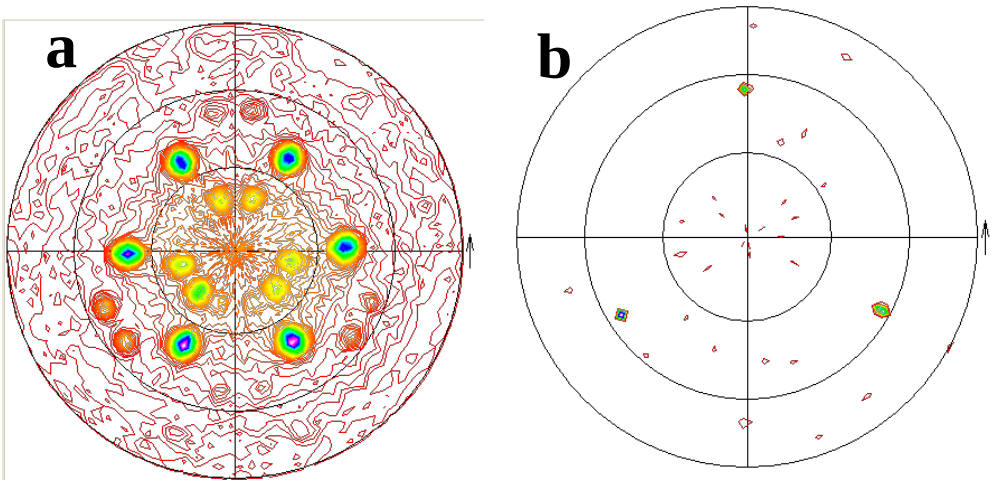

Figure C.3. The $(10\bar{1}4)$ pole figure of hematite (a) on the magnetite film after calcination in an O_2 atmosphere at 400 ^{o}C for 4 hours, and the Au(100) substrate pole figure (b) on Au(111) single crystalline substrate. The magnetite was electrodeposited on single crystalline Au(111) substrate at -1.065 V versus Ag/AgCl until 1 C/cm^2 was passed. The film is estimated to be 2 μm thick.

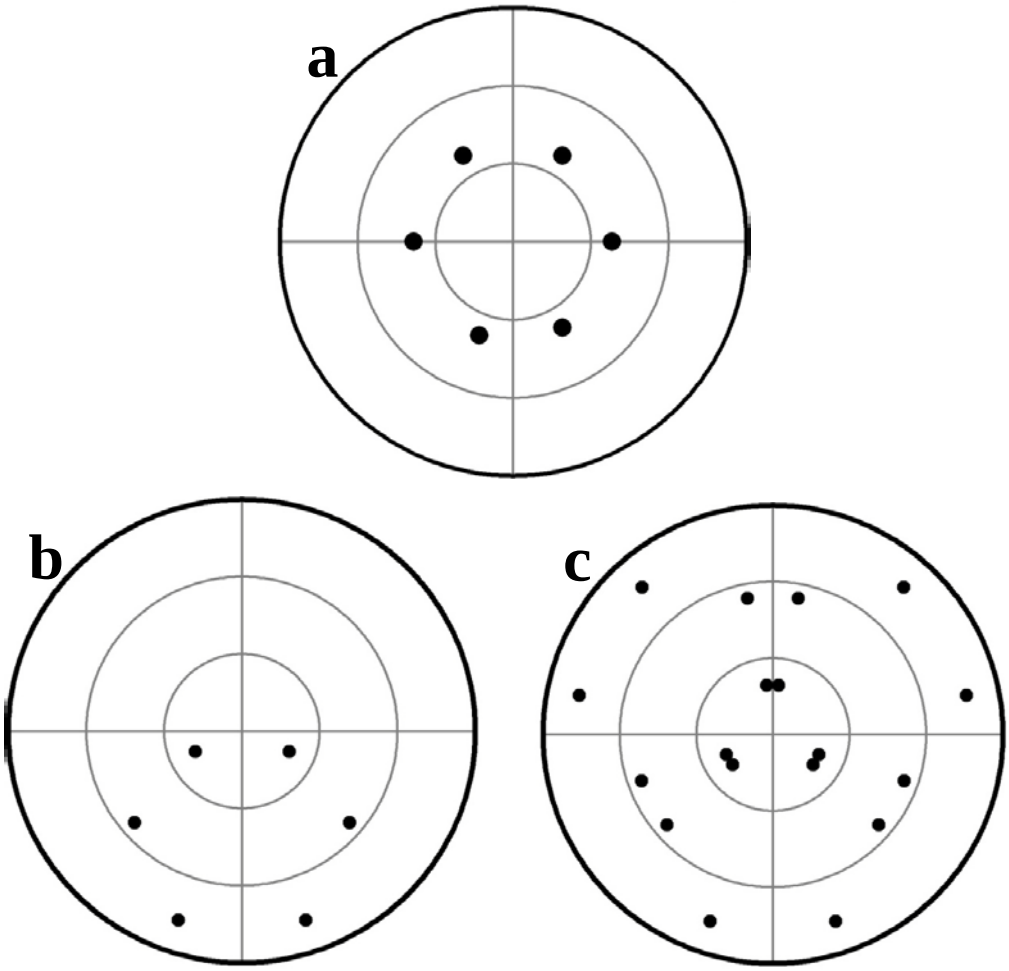

Figure C.4. Stereographic projection with hematite $(10\bar{1}4)$ type reflection. (a) with (0001) out-of-plane orientation, 6 spots are found at 38.24°. (b) with $(11\bar{2}6)$ out-of-plane orientation, 2 spots are found at 19.66°, 2 are at 54.48°, another 2 are at 77.28°. (c) the resulting stereographic projection after rotating the stereographic projection in (b) by 120° and 240°, then overlaying each other.

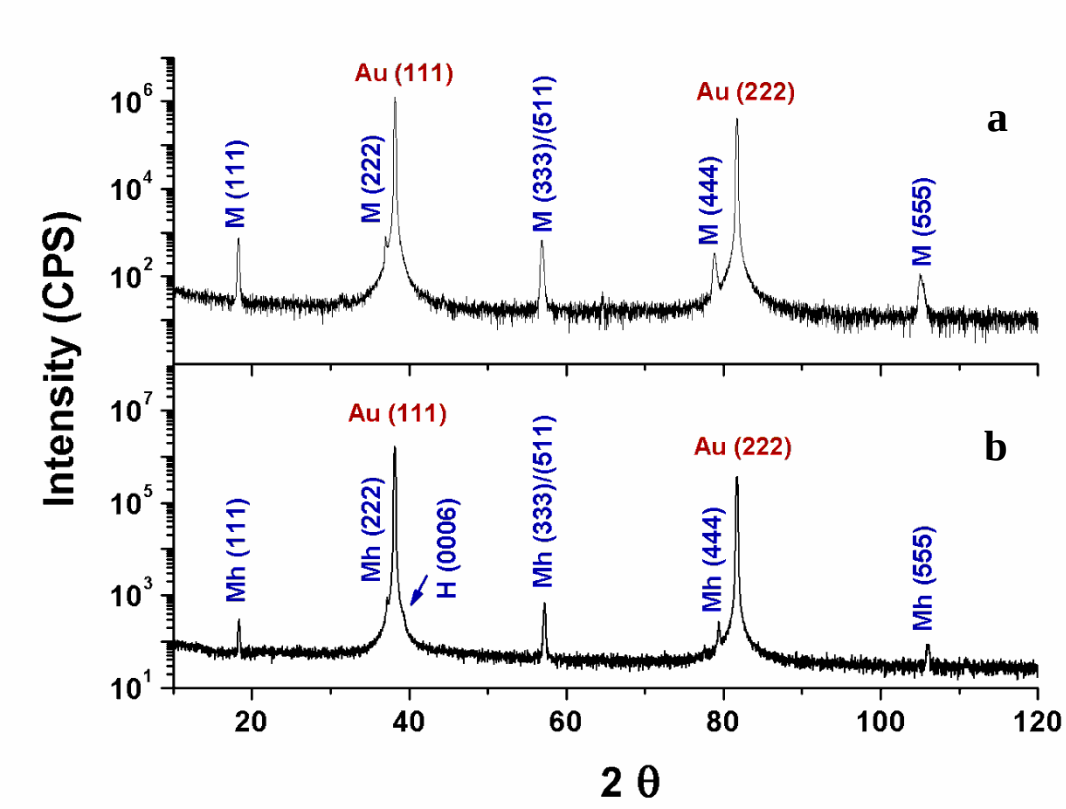

Figure C.5. Symmetric X-ray diffraction patterns of the magnetite film (Fe_3O_4) as deposited (a) and after calcination (b) in an O_2 atmosphere at 400 ^oC for 4 hours. The magnetite is deposited on single crystalline Au(111) substrate at -1.065 V versus Ag/AgCl until 0.1 C/cm^2 was passed. The film is estimated to be 200 nm thick.

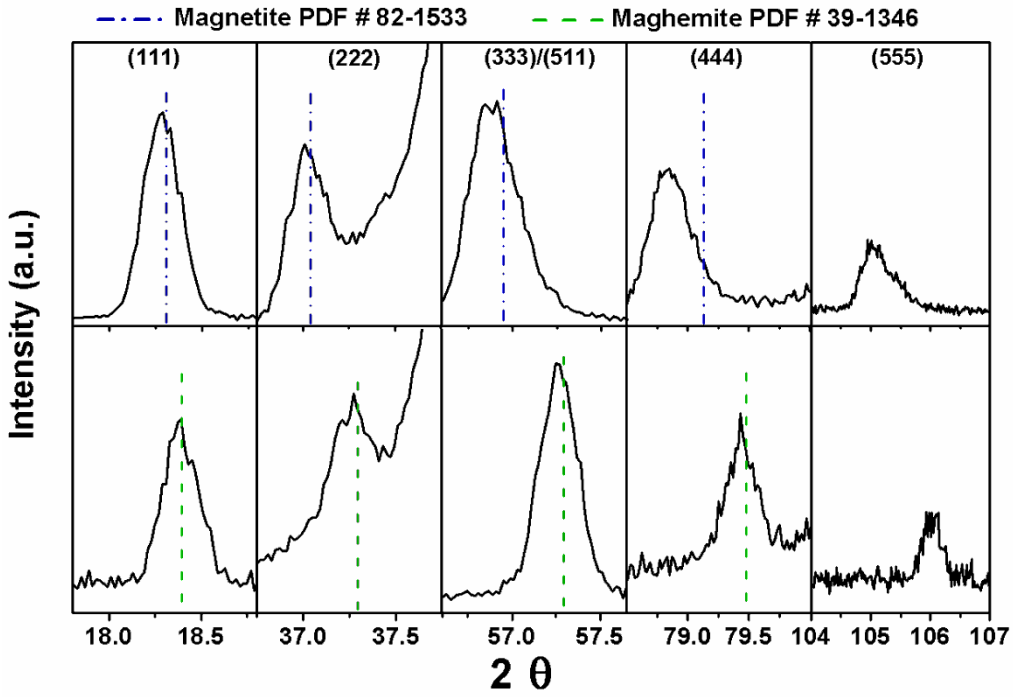

Figure C.6. The enlarged pictures of each peak in the symmetric X-ray diffraction patterns (Figure C.5) of the magnetite film (Fe_3O_4) as deposited (upper) and after calcination (lower) in an O_2 atmosphere at 400 ^oC for 4 hours. The magnetite is deposited on single crystalline Au(111) substrate at -1.065 V versus Ag/AgCl until 0.1 C/cm^2 was passed. The film is estimated to be 200 nm thick.

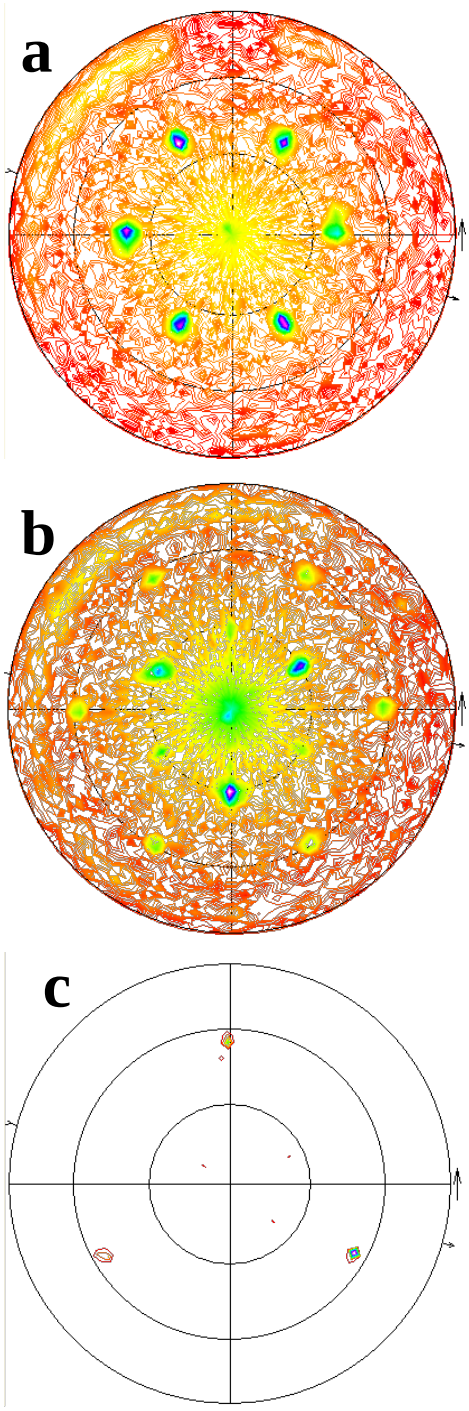

Figure C.7. The $(10\bar{1}4)$ pole figure of hematite (a) and the (311) pole figure of maghemite on the magnetite film after calcination in O_2 atmosphere at 400 ^{o}C for 4 hours, and the Au(100) substrate pole figure (b) on Au(111) single crystalline substrate. The magnetite is electrodeposited on single crystalline Au(111) substrate at -1.065 V versus Ag/AgCl until 0.1 C/cm^2 was passed. The film is estimated to be 200 nm thick.

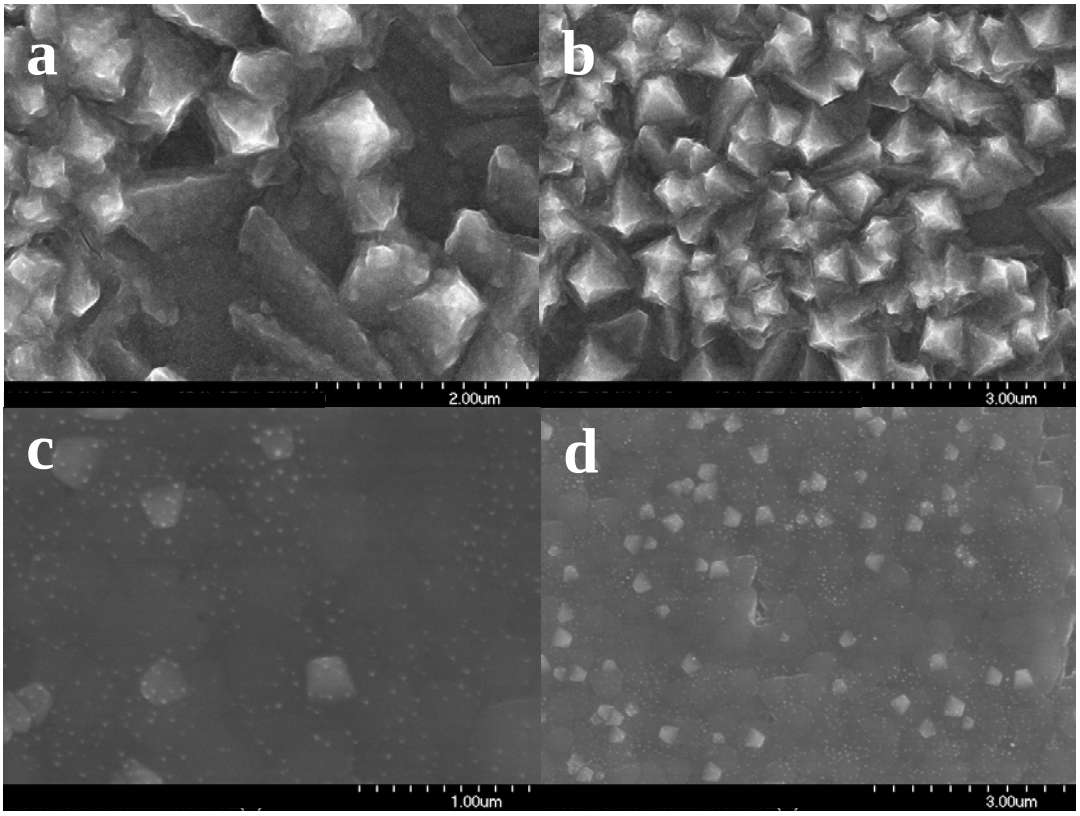

Figure C.8. SEM images with different magnifications of the magnetite films (Fe_3O_4) after calcination in O_2 atmosphere at 400 ^oC for 4 hours. The magnetite film was deposited on single crystalline Au(111) substrate at -1.065 V versus Ag/AgCl until 0.1 C/cm^2 (A, B) and 1 C/cm^2 (C, D) was passed.

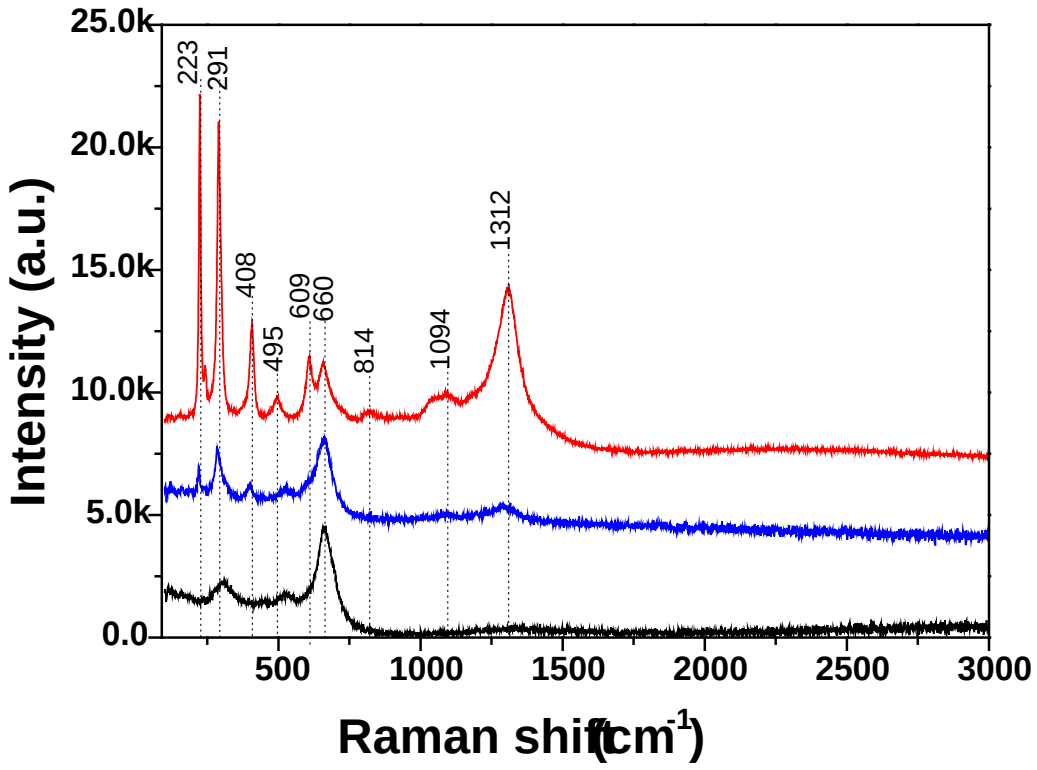

Figure C.9. Raman spectra of the magnetite films (Fe_3O_4) as-deposited on single crystalline Au(111) substrate at -1.065 V versus Ag/AgCl until 0.1 C/cm^2 (black line, bottom) and the same film after calcination in O_2 atmosphere at 400 ^oC for 4 hours (blue line, middle), and the 1 C/cm^2 film after calcination (red line, top).

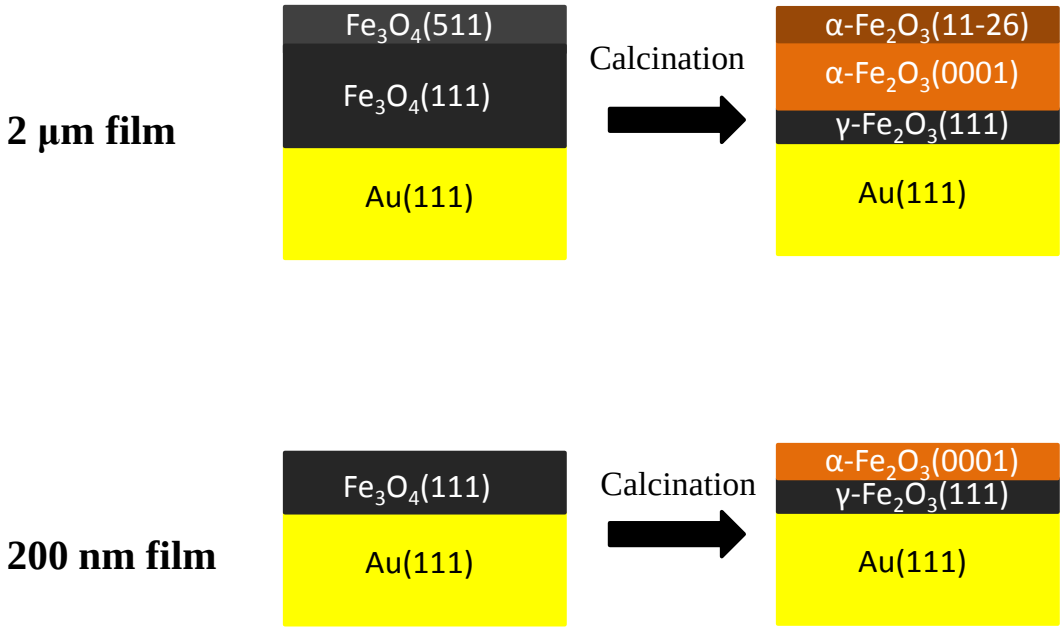

Figure C.10. Illustrations of the thermal transformation of the magnetite films (Fe_3O_4) as deposited on single crystalline Au(111) substrate at -1.065 V versus Ag/AgCl until 0.1 C/cm^2 (200 nm) and 0.1 C/cm^2 (2 µm). The film is annealed in O_2 atmosphere at 400 ^oC for 4 hours.

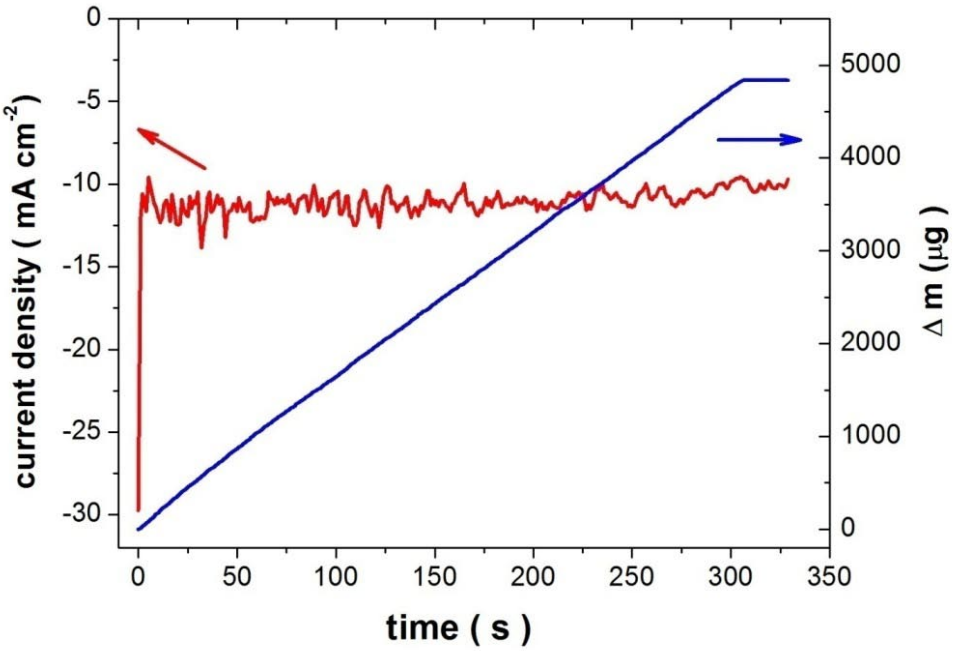

Figure C.11. EQCM study on the electrodeposition of ferrihydrite. Red line is the recoding current, blue line the mass increase on the EQCM electrode. The ferrihydrite is deposited on the Au coated side of the electrodeposited at -1.200 V versus Ag/AgCl from Fe(III)-TEA solution.

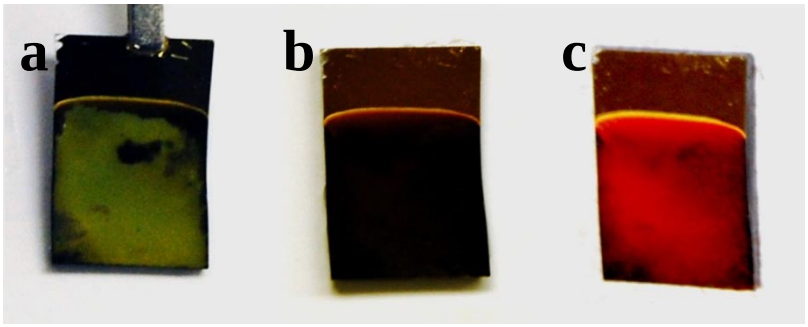

Figure C.12. Photo images of the three samples deposited on Au coated microscope slides. (a) is the film immediately taken out from the deposition solution. (b) is the (a) film exposed to air for 5 minutes , (c) is the same film after being air dried for 2 hours.

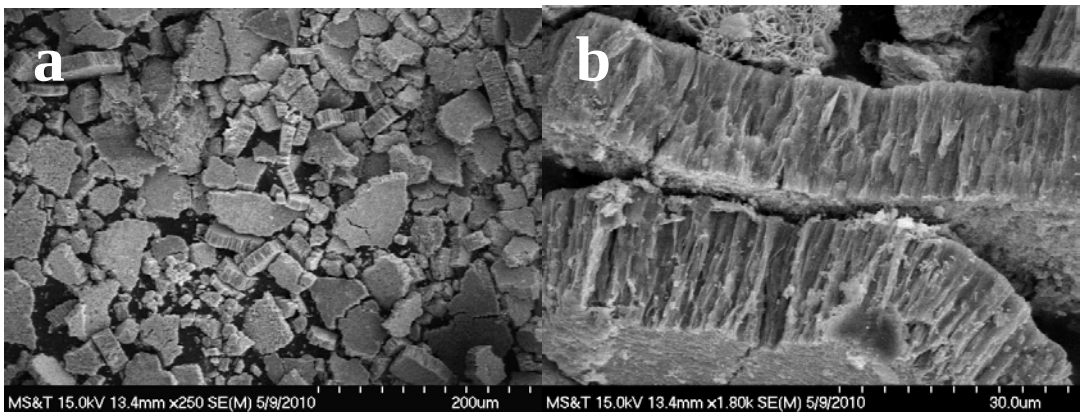

Figure C.13. SEM images of multiple electrodeposited ferrihydrite films (a) that were peeled offfrom the Au-glass substrate, and (b) annealed in O_2 at 400 ^{o}C for 4 hours.

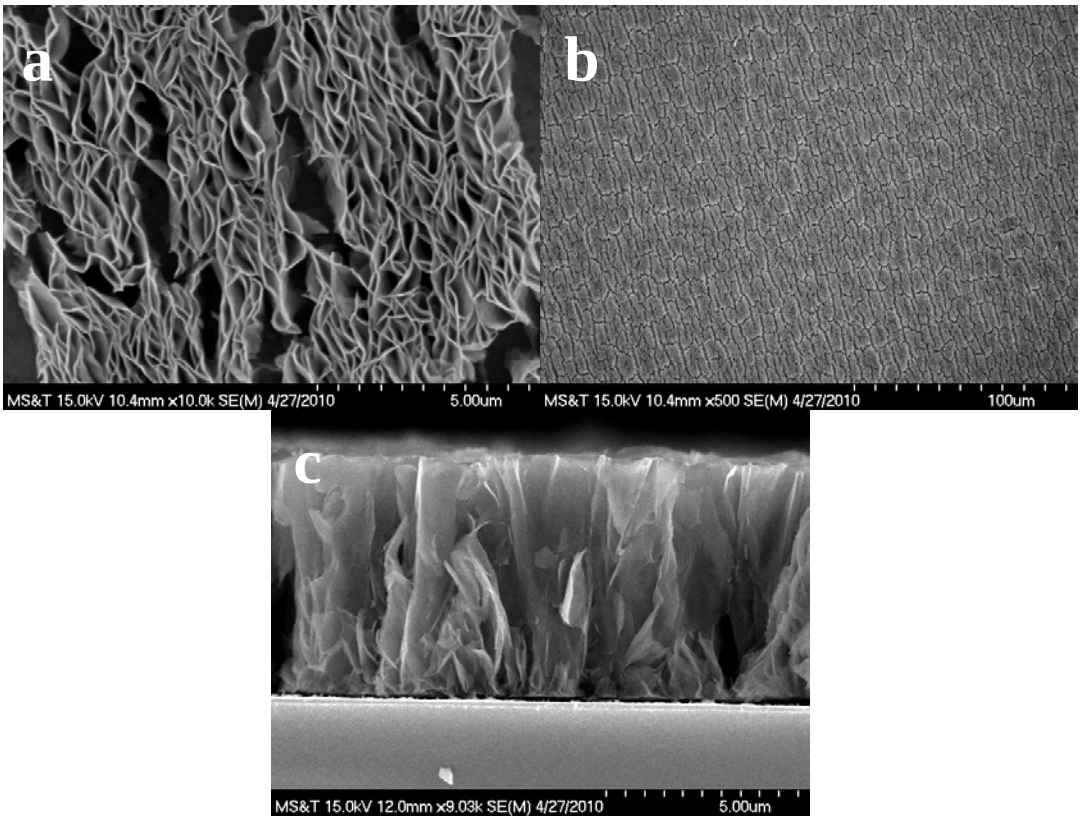

Figure C.14. SEM images of the electrodeposited ferrihydrite films on Au(110) substrate and annealed in O_2 at 400 ^{o}C for 4 hours (a, b). (c) is the cross-section image of film deposited on Au-glass substrate.

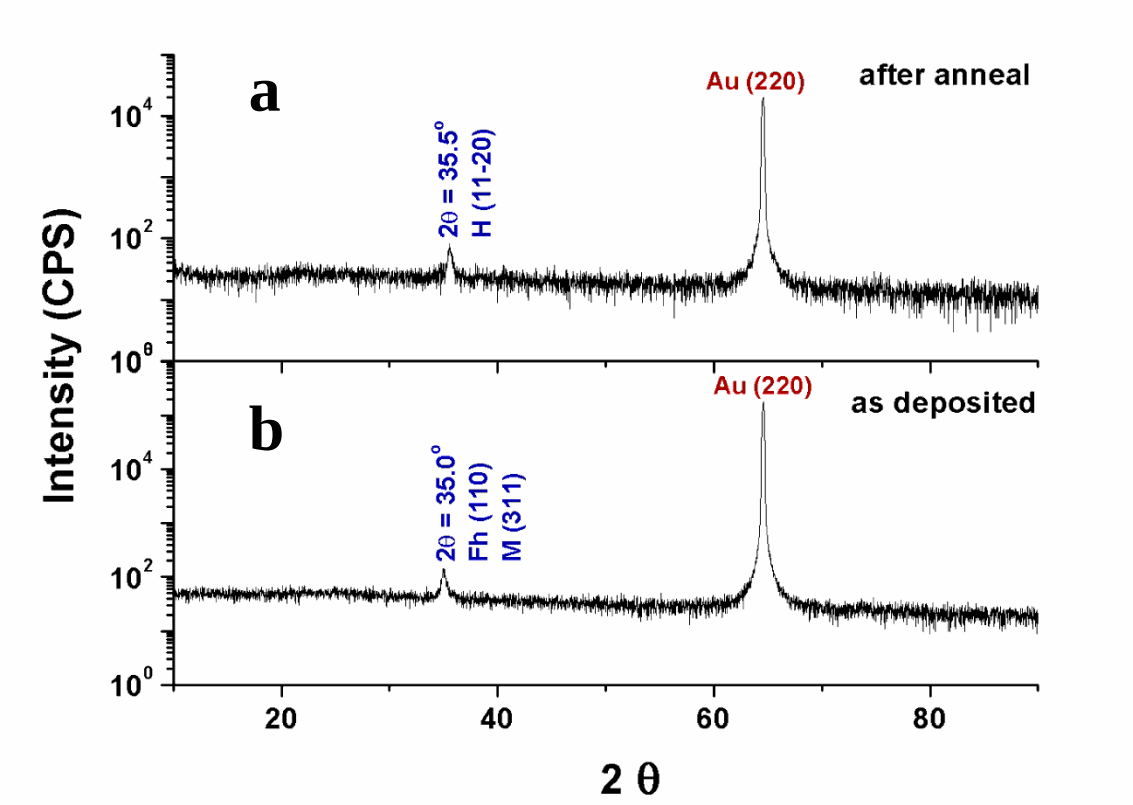

Figure C.15. Symmetric X-ray diffraction patterns of ferrihydrite films on Au(110) substrate before (a) and after (b) annealing in O_2 at 400 ^{o}C for 4 hours. In the figure, H represents hematite, Fh represents ferrihydrite, and M represents magnetite.

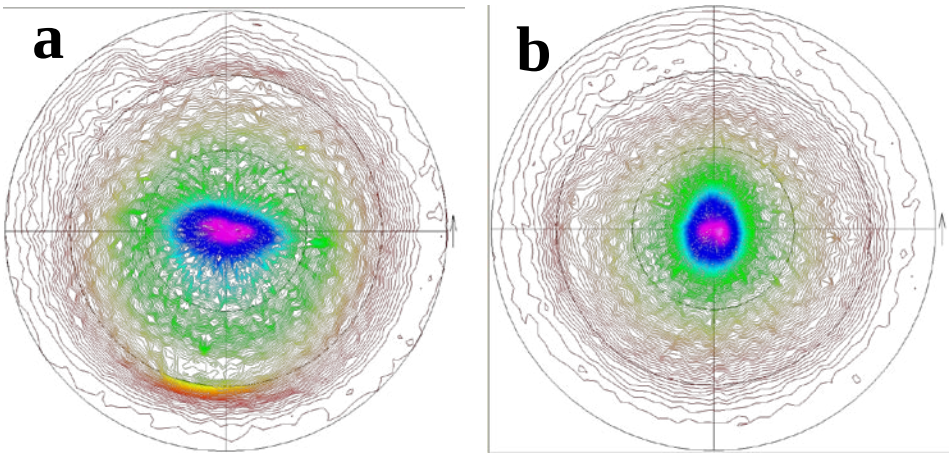

Figure C.16. X-ray pole figures of the ferrihydrite films on Au(110) substrate before (a) and after (b) annealing in O_2 at 400 ^{o}C for 4 hours. (a) is a ferrihydirte (110) pole figure. (b) is a hematite $(1\bar{1}20)$ pole figure.

PATENT

Bin Zhao, Guo-Jun Mu "Nano Core-Shell Bimetal Powder of Cu and Sn, Preparing Method and Application" CN1,539,577 (Golden Medal of China's International Exhibition of Inventions, 2004)

PUBLICATIONS

1. Guojun Mu, Rakesh V. Gudavarthy, Elizabeth A. Kulp, and Jay A. Switzer. "Tilted Epitaxial ZnO Nanospears on Si(001) by Chemical Bath Deposition." *Chemistry of Materials* **2009**, *21(17)*, 3960–3964.

2. Switzer, Jay A.; Gudavarthy, Rakesh V.; Kulp, Elizabeth A.; Mu, Guojun; He, Zhen; Wessel, Andrew J. "Resistance Switching in Electrodeposited Magnetite Superlattices." *Journal of the American Chemical Society* **2010**, *132(4)*, 1258-1260.

3. Guo-Jun Mu, Bin Zhao. "Preparation and Characterization of Core-shell Cu-Sn Bimetallic Nanoparticles" *Chinese Journal of Inorganic chemistry* **2004**, *20(9)*, 1055

4. Guo-Jun Mu, Bin Zhao. "Component Analysis of Core-shell Cu-Sn Bimetallic Nanoparticles" *Journal of East China University of Science and Technology* **2004**, *30(4)*, 470

5. Guo-Jun Mu, Bin Zhao. "Research Advances of Inorganic Nano Additives in Lubricating Oil" *Lubricating Oil* **2004**, *19(1)*, 59.

VITA

Guojun Mu was born on November 16, 1978 in the City of Yantai, Shandong Province, P. R. China, to father Guangliang Mu and mother Jianhua Liu. She received her Bachelor of Science (B.S.) degree in Chemistry in 2001 from East China University of Science and Technology (Shanghai, China). In 2004, she obtained her Master of Science (M.S.) degree from the same department and same university. During her M.S. program, her academic advisor was Prof. Bin Zhao. Her research project involved the syntheses of Cu-Sn core-shell bimetallic nanoparticles by hydrothermal methods and thereby applications as additives in lubricants. She has published three papers and applied one patent on this project. Her graduation thesis received the 2004 Outstanding Master Thesis Award from East China University of Science and Technology.

In January 2005, she came to Missouri University of Science and Technology (known as University of Missouri-Rolla then) to pursue her Doctor of Philosophy (Ph.D.) degree in Chemistry. Since May 2005, she has researched under the guidance of Dr. Jay A. Switzer who offered her a research assistantship. Her research has involved the electrodeposition and chemical bath deposition of semiconductor materials that have potential applications in photovoltaic devices. This project was funded by National Science Foundation (NSF) and Department of Energy (DOE) of the United States. She has published one paper and submitted another two to Journal of Chemistry Materials. She will graduate and receive her Ph.D. degree in chemistry in December 2010.